1 The unique spectral and geomorphological characteristics of pitted impact deposits associated with

2 Marcia crater on Vesta

3 T. Michalik[a], K.-D. Matz[a], S. E. Schröder[a], R. Jaumann[b], K. Stephan[a], K. Krohn[a],

4 F. Preusker[a], C. A. Raymond[c], C. T. Russell[d], K. A. Otto[a]

5

6 [a] German Aerospace Center (DLR e.V.), Rutherfordstr. 2, 12489 Berlin, Germany (tanja.michalik@dlr.de)

7 [b] Institute of Geological Sciences, Freie Universität Berlin, Malteserstr. 74-100, 12249 Berlin, Germany

8 [c] Jet Propulsion Laboratory, California Institute of Technology, Pasadena, California, USA

9 [d] Department of Earth, Planetary, and Space Sciences, University of California Los Angeles, Los Angeles, California, USA

10

11 Abstract

12 The occurrence of pitted impact deposits (**PIDs**) and widespread OH-bearing minerals on the

13 differentiated asteroid Vesta shows that volatiles delivered by exogenic sources play an important role

14 for surface appearance and processes on airless bodies. The young, large crater Marcia features widely

15 spread PIDs in its crater-fill and ejecta deposits. In order to derive more details on their formation, we

16 studied the spectral and geomorphological properties of PIDs associated with Marcia. Our observations

17 imply that the formation of PIDs is linked to topography-controlled accumulation of ejecta and the

18 accompanying increase of deposit thickness as well as internal heat. This is best illustrated where PIDs

19 are located within pre-existing craters (i.e., pre-Marcia), enabling the estimation of pre-impact

20 topography and deposit thickness.

21 Previous studies reported a lower than average reflectance at visible wavelengths for the crater-fill PIDs,

22 which we confirm. However, several PIDs outside the crater exhibit higher reflectance and pyroxene

23 band strength than the average Vesta and the majority of PIDs exhibit higher reflectance and pyroxene

24 band strength with respect to their immediate surroundings (which belong to the same impact deposit).

25 Furthermore, at least six PIDs (many are ambiguous) show resolvable, diminished absorption bands at

26 2.8 µm, corresponding to a depletion in OH. These spectral observations are most consistent with less

27 contamination by exogenic carbonaceous chondrite materials, i.e., a loss of hydroxyl groups as well as

28 dark components. Our observations are inconsistent with differences in grain size, pyroxene

29 composition, glass content or age-related differences. Regarding reflectance at 750 nm and pyroxene

30 band depth (750/917 [nm]), we present a unique spectral trend for PIDs with respect to 'typical Vestan'

31 materials, suggesting a likewise unique formation process occurring on this asteroid. The crater-fill PIDs

32 display ambiguous spectral characteristics that we attribute to post-impact inflow of dark material from

33 the crater rim. PIDs are ubiquitous in the Marcia region (> 100 individual clusters). Yet volatiles lost at

34 these sites might only represent a minor fraction (< 2 %) of volatiles still present in the host ejecta. An

35   average PID only lost ~ 1 wt% of volatiles upon devolatilization, implying that exceptionally high

36   volatile contents are not critical for PID formation on Vesta.

37

38   Keywords: Asteroid Vesta; Asteroids, surfaces; Spectroscopy; Geological processes

39

40   1 Introduction

41   1.1 Crater-related pitted material

42   Crater-related pitted materials/terrains are relatively newly recognized geomorphologic features

43   associated with the best-preserved craters on Mars as well as on Vesta and Ceres and are linked to the

44   loss of volatiles (Tornabene et al., 2007 and 2012; Boyce et al., 2012; Denevi et al., 2012; Sizemore et

45   al., 2017). These pitted materials/terrains consist of polygonal to circular depressions and generally

46   occur in dense clusters within crater-fill, terrace and exterior impact deposits as well as channelized

47   flows. Individual pits lack evidence of ejecta deposits and only show subtle raised rims or a complete

48   lack thereof. The size of individual pits ranges from tens of meters to a few kilometers (Tornabene et

49   al., 2012; Denevi et al., 2012; Sizemore et al., 2017) and parent crater diameters vary between ~ 1 and

50   150 km (Tornabene et al., 2012; Denevi et al., 2012; Sizemore et al., 2017). The term 'parent crater' is

51   used here to distinguish between (genetically unrelated, pre-existing) craters that merely host a pitted

52   terrain vs. the crater whose formation led to the creation of these geomorphological features.

53   Pitted materials on Mars have been recognized as primary impact deposits earlier by Tornabene et al.

54   (2007). Yet it was the extensive survey of more than 200 craters on Mars by Tornabene et al. (2012)

55   that confirmed the primary impact-related nature of these geomorphologic features with the pits

56   representing volatiles escaping from a non-ambient and possibly melt-rich deposit. This and the study

57   by Boyce et al. (2012) revealed more insights in the formation mechanism, the relationship to the host

58   deposit and parent crater, age, as well as global distribution and abundance. They found that pitted

59   materials occur preferentially in mid-latitudes suggesting a dependence on the water/ice-silicate ratio as

60   volatile content increases with latitude on Mars. Furthermore, pit size as well as cluster extent positively

61   correlate with parent crater size as do preservation states of pitted materials and their parent craters.

62   Additionally, similarities to the impact melt-bearing breccia suevite at the Ries impact structure in

63   Germany were concluded as both target materials are/were volatile-rich (e.g., Newsom et al., 1986;

64   Tornabene et al., 2007 and 2012; Boyce et al., 2012). Tornabene et al. (2012) inferred that the pitted

65   materials on Mars and their host deposits most likely resemble impact melt-bearing breccias. Within the

66   suevite outside of the Ries crater, 'chimney-like degassing pipes' were identified (e.g., Engelhardt, 1972

67   ; Newsom et al., 1986) which suggests devolatilization after suevite deposition. The pitted materials on

68   Mars could thus result from the formation of similar vents through the host deposit.

Evidence for pitted terrains on asteroid Vesta was firstly presented by Denevi et al. (2012) shortly after NASA's Dawn mission arrived at this second largest object in the inner asteroid belt. They found striking similarities to the pitted materials observed on Mars and concluded a similar explosive devolatilization process for these Vestan features. Dawn went on to its next target, Ceres, and Sizemore et al. (2017) likewise presented a detailed survey of pitted terrains on the dwarf planet's surface. They found that Cerean pitted terrains strongly resemble those on Vesta and Mars and accordingly inferred a rapid post-impact formation model. The pitted terrains' formation models for Vesta and Ceres are based on the extensive analysis from Tornabene et al. (2012) and Boyce et al. (2012) for Mars. However, for the intriguing crater Occator on Ceres (largest well-preserved crater showing 'bright' spots), Schenk et al. (2020) found that volatile-related pits are in general less common and distinct from the densely clustered pits observed on Mars. Similar to the lack of pitted materials in high latitudes on Mars (Tornabene et al., 2012), this might result from (too) high volatile contents in the crust (up to ~ 60 % ice and clathrates, Ermakov et al., 2017; Fu et al., 2017). Sizemore et al. (2017) linked Cerean pit formation to available volatiles in the regolith whose source could either be minerals and ice (see also e.g., De Sanctis et al., 2015a; Combe et al., 2016). This is still under debate for Vesta (Denevi et al., 2012; Scully et al., 2015) and will be addressed later on.

The detailed studies of the pitted materials on all three bodies revealed that they clearly represent primary impact-related geomorphologic features and that they are best-preserved where their host craters are also well-preserved. This is why from now on we will refer to the pitted materials/terrains as 'pitted impact deposits' (**PIDs**), which was already mentioned by Tornabene et al. (2012).

1.2 Vesta, its surface regolith and pitted impact deposits

Vesta is thought to have fully differentiated (e.g., McCord et al., 1970; Larson & Fink, 1975; Consolmagno & Drake, 1977; Ruzicka et al., 1997; Keil, 2002; Mittlefehldt, 2015; and references therein), losing volatile species in the process. The evidence for the differentiation of Vesta arises from its strong connection to the HED meteorites (howardite, eucrite, diogenite). This suite of meteorites comprises achondritic igneous rocks that display the upper range of a differentiated body: ultramafic rocks composed of Magnesium-rich orthopyroxenes (diogenites), crustal cumulates and basalts (eucrites) as well as surface regolith (howardites; e.g., Mittlefehldt, 2015 and references therein). The HED-Vesta connection is based on the distinct pyroxene-dominated reflectance spectrum of these objects (McCord et al., 1970) and was confirmed by numerous studies that employed data from NASA's Dawn mission (e.g., Reddy et al., 2012b; De Sanctis et al., 2012a and 2013; Ammannito et al., 2013a; Prettyman et al., 2012; Thangjam et al., 2013). The discovery of 'pitted terrains' (Denevi et al., 2012), transient water flow (Scully et al., 2015), widespread hydrated materials (De Sanctis et al., 2012b) as well as exogenic hydrogen (Prettyman et al., 2012) was therefore surprising.

104   The Dawn mission moreover revealed that a 'dark' surface component mixed within the regolith

105   obscures the Vestan reflectance spectrum at numerous locations (e.g., Jaumann et al., 2014; Stephan et

106   al., 2014) and over a large area extending from an equatorial region to the north pole (roughly

107   200,000 km^2, between 70 °E to 220 °E and 30 °N to 30 °S; e.g., De Sanctis et al., 2012b; Combe et al.,

108   2015). The reflectance spectra at these sites show decrease of reflectance at visible wavelengths and

109   diminishment of absorption features in contrast to 'bright' areas on Vesta (e.g., Zambon et al., 2014).

110   Several studies (e.g., McCord et al., 2012; Reddy et al., 2012a; Cloutis et al., 2013a; Nathues et al.,

111   2014) suggest that this darkening agent most likely originates from the infall of carbonaceous chondrites

112   (possibly CM-type) over geological time scales. This exogenic contamination is important when

113   considering the delivery of water through the solar system. As we have learned from Dawn, even

114   differentiated objects can hold considerable amounts of 'water' within their regolith which influences

115   the asteroids' surface geology.

116   On Vesta, currently only four parent craters show PIDs (Marcia, Cornelia, Numisia, Licinia; Denevi et

117   al., 2012), of which only two are undoubted occurrences (Marcia and Cornelia). Marcia is the only crater

118   featuring PIDs beyond its crater rim (Denevi et al., 2012), though this might be an observational bias

119   due to limited image resolution. The (observable) occurrences associated with Marcia crater account for

120   ~ 96 % of all PIDs on the asteroid (this study). Calpurnia crater adjacent to Marcia could also be the

121   parent crater for some of the PIDs (i.e., PIDs originating from Calpurnia impact deposits), which would

122   add another parent crater to the suite on Vesta. Yet in this study we consider the PIDs in this area as one

123   occurrence, which will be addressed in more detail later on. Calpurnia and Cornelia are well-preserved

124   craters nearby which might have influenced the larger Marcia region studied here (for spatial context

125   see Figs. 2 & 3).

126   The crater Marcia is situated within the above mentioned spectrally darker extended area (De Sanctis et

127   al., 2012b, 2013 and 2015c, Combe et al., 2015) at around 190° E and 10° N (Claudia Coordinate system)

128   and is the best-preserved large crater on Vesta. While the Rheasilvia Basin covering the South Pole is

129   thought to be around 1 or 3.5 Ga old (modelling ages by Marchi et al., 2012 and Schmedemann et al.,

130   2014, respectively), Marcia is the next largest well-preserved crater and considerably younger with a

131   modeled age of ~ 40 or 390 Ma (Williams et al., 2014b). Marcia has been of high interest to many

132   studies (e.g., Williams et al., 2014a and 2014c; De Sanctis et al., 2015b and 2015c; Denevi et al., 2012;

133   Scully et al., 2015; Keihm et al., 2015) due to its unusual and asymmetric shape, reflectance spectra,

134   thermal properties and geomorphologic features including PIDs as well as gully-like features. Marcia is

135   also the focus of this study due to the remarkable preponderance of PIDs situated in and around this

136   crater.

137   Marcia is ~ 58 km wide and 68 km long and possesses a relatively large wall-slump or terrace off the

138   southern rim that also possesses PIDs. Calpurnia and Minucia are two adjacent craters to the NE (Fig.

139   2a). Marcia and its surroundings exhibit numerous PIDs (we count > 100 discrete occurrences). PIDs

on Vesta are generally defined as clusters of irregularly shaped, rimless depressions, at times also overlapping with other pits (Denevi et al., 2012) which occur on otherwise smooth deposits on crater floors, and for Marcia on its southern terrace as well as within its continuous ejecta blanket. Denevi et al. (2012) concluded that the PIDs formed, similarly as on Mars, through explosive volatile outgassing. They suggest that volatile-bearing deposits like those from carbonaceous chondrites have been emplaced in the upper surface of the Vestan crust by pre-Marcia exogenic impactors which subsequently led to the formation of PIDs upon impact of the Marcia impactor. Scully et al. (2015) suggest that icy subsurface deposits could also be responsible for the formation of PIDs, thus the volatile sources for PIDs require further investigation.

The spectral characteristics of PIDs have not been studied in detail yet, except for the PIDs on Marcia's floor. Denevi et al. (2012) and De Sanctis et al. (2015c) both reported that the PIDs on Marcia's floor are darker than the average Vesta and correlated the PIDs with the OH-bearing material prevailing the previously mentioned area that De Sanctis et al. (2012b) described as "OHRT1" (OH-rich terrain). However, not all the PIDs exhibit a generally darker spectrum. Numerous PIDs in Marcia's vicinity exhibit higher reflectance and stronger pyroxene absorptions (i.e. 'purer', with less exogenic contamination) with respect to average Vestan values. Additionally, the 2.8 μm absorption band is weaker at some of the PIDs' sites (consistent with a depletion in OH) with respect to their immediate surroundings.

Our overall objective is to build and expand upon the geomorphological and spectral observations of PIDs on Vesta to: 1) test and place further constraints on the existing hypotheses explaining the origin and emplacement of PIDs, and (2) gain insight into the physical and/or petrological changes that material underwent while rapidly losing volatiles.

We present an extended map of PIDs and analyze the local geomorphological setting of the PIDs in more detail to see if they are consistent with previous observations that support an impact origin for these materials. While Denevi et al. (2012) report that PIDs often occur in topographic lows, a detailed analysis has not yet been undertaken. We also present detailed spectral characteristics of PIDs and their surroundings which have not been reported yet. In this study we use Dawn Framing Camera (FC, Sierks et al., 2011) images, spectral data from the visible and infrared spectrometer (VIR, De Sanctis et al., 2011; Combe et al., 2015) as well as comparisons with meteoritic spectral data.

2 Data sets and methods

2.1   Dawn's Framing Camera at Vesta

This study's main observations are derived from data collected by the Dawn Framing Camera (FC). The FC has one panchromatic clear filter and seven narrowband color filters in the visible and near infrared (~ 0.43-0.97 μm, Sierks et al., 2011). The filters of the FC focus on the visible and near infrared

wavelength region as Vesta's surface mineralogy is dominated by pyroxenes, showing a distinct iron absorption band at ~ 0.9 μm (McCord et al., 1970). All maps shown here are based on the Claudia coordinate system (Russell et al., 2012; Supplementary Text) and presented in equidistant projection oriented with north toward the top. The FC mosaics are photometrically corrected to I/F at i=30°, e=0°, and p=30° (incidence, emission and phase angle, respectively), using the Akimov function as described in Schröder et al. (2014). We will use the term 'reflectance' for the photometrically corrected I/F throughout this study. Clear filter images for geomorphological observations are depicted at LAMO resolution (Low Altitude Mapping Orbit up to 16 m/px, Roatsch et al., 2013), while the shown RGB composite depicting multispectral information were produced with HAMO resolution (High Altitude Mapping Orbit ~ 60 m/px, Roatsch et al., 2012), which is the highest resolution with complete filter coverage.

In the past, studies using Dawn FC data commonly employed the Clementine-type RGB composite introduced by Pieters et al. (1994) for the lunar data set obtained during the Clementine mission. The Clementine-type RGB composite include the following ratios for the respective channels: R=750/415 [nm], G=750/950 [nm], B=415/750 [nm], and were used for Vesta in e.g. Reddy et al. (2012b), Denevi et al. (2012), Le Corre et al. (2013) and Williams et al. (2014a). This composite can give valuable information about the surface composition and/or degree of space weathering (especially on the Moon). The red and blue band ratio in the Clementine-type RGB composite is sensitive to soil maturity (spectral 'reddening' positively correlates with maturity) as well as composition, whereas the green band is sensitive to strength and character of the common mafic absorption near 1 μm caused by the presence of Fe^{2+}.

In this study, we use another RGB composite to illustrate compositional and/or physical differences. It is tightly connected to our observations of the PIDs and Vesta in general. As low-Ca orthopyroxenes predominate the Vestan spectra, pyroxene absorption band positions of the Vestan surface vary between ~ 920 and 935 nm (Ammannito et al., 2013a; De Sanctis et al., 2013), mostly depending on their Fe/Mg contents. Diogenites generally have pyroxene absorption band positions at shorter wavelengths than eucrites due to higher Mg contents of their orthopyroxenes (see Fig. 1 left panel and e.g., Gaffey, 1976; Mittlefehldt, 2015). Therefore, their spectra exhibit higher 965/917 [nm] values than eucrites, while howardites are in between. We therefore use the 965/917 [nm] ratio for the red channel as it is the most significant parameter in order to distinguish between the main Vestan rock types diogenites and eucrites, which was previously described in Le Corre et al. (2011); Reddy et al. (2012b) and Thangjam et al. (2013).

The reflectance of HEDs and Vestan spectra is generally at its highest around 750 nm, before it drops due to the absorption of electromagnetic energy by the iron-bearing pyroxene (see Fig. 1, left panel). As pyroxene absorption band positions on Vesta are closest to the 917 nm filter of the FC, the ratio 750/917 [nm] is best suited to characterize the material's pyroxene absorption strength. The PIDs differ

from their immediate surrounding foremost in reflectance at 750 nm and pyroxene absorption band strength. Consequently, we chose the green and blue band of our RGB composite accordingly (750 nm and 750/917 [nm], respectively).

In summary, greenish and cyan colors in the applied RGB composite denote higher reflectance and pyroxene absorption band strength. We emphasize that all images of this RGB composite use the same stretch while the standard deviation stretch type with n=1.3 showed the best results with respect to the perception of the viewer. We also note that artefacts occur in the HAMO RGB composite as a result of the mosaicking process (along single image boundaries) and due to missing or incomplete data, e.g. in shadowed areas.

The Digital Terrain Model (DTM) by Preusker et al. (2014 and 2016)was modified by including LAMO images and implementing a triaxial ellipsoid (286 x 279 x 223 [km]) in order to reach the most realistic approximation to the actual geophysical altitudes and their relations. With a lateral resolution of ~ 70 m/px and a vertical accuracy of ~ 6 m, the DTM helps to examine the topographic context of the PIDs. No vertical exaggeration was applied. In addition to FC data, we use the VIR-derived 2.8 µm absorption band depth distribution map generated by Combe et al. (2015) in order to evaluate the OH content of relevant locations. In contrast to the RGB composite, we use a dynamic range adjustment in displaying this data which is especially important regarding Figure 11. This map has an approximate resolution of ~ 200 m/px.

2.2   RELAB spectral data

We used HED as well as carbonaceous chondrite and olivine spectral data for comparative observations. These data were obtained from the RELAB database at the Brown University, which is publicly available under:

 http://www.planetary.brown.edu/relabdocs/relab_disclaimer.htm.

In order to compare the meteorite spectra with space craft camera data, the meteorite spectra were resampled to fit the format of the responsivity functions of the respective filter (Sierks et al., 2011). The resampling of the RELAB meteorite spectra occurred as follows:

$$R_{mfc}(\lambda) = \int R_m r_i(\lambda) d\lambda \ / \int r_i(\lambda) d\lambda \qquad (1),$$

where R_{mfc} is the reflectance value of the resampled meteorite spectrum for the respective filter, R_m is the original reflectance of the meteorite spectrum obtained in the laboratory, r_i is the responsivity function for each filter and λ is the respective FC filter wavelength.

In total, data from 239 RELAB spectra are used in this study, with 142 being from HED meteorites and 82, 33 and 27 spectra from eucrites, diogenites and howardites, respectively. Many meteorites were measured multiple times, e.g. because different grain sizes were measured or powders vs. slabs. We

245 incorporate everything in order to display a great diversity. In total, the following quantities of actual
246 meteorites were measured: 44 eucrites, 16 howardites and 14 diogenites. Only seven samples of our
247 database are official Antarctic pairings of which one is a eucrite, four are howardites and two belong to
248 the impact melt samples. We display all of those as we want to display a great variety of possible
249 lithologies. Yet we acknowledge that unidentified pairing might further decrease the number of actually
250 measured meteorites.

251 Other spectra used here include the mineral olivine (19, various compositions, see Table S1) as well as
252 carbonaceous chondrites (69 spectra from 44 individual carbonaceous chondrites). Zolensky et al.
253 (1996) analyzed clast contents of HEDs and found a remarkable predominance of CM2 carbonaceous
254 chondrites (~ 81%). Therefore, we mainly used spectra derived from CM-type chondrites, which are
255 distinguished within the carbonaceous chondrite data points in Figure 1. We also included spectral data
256 of impact melts (9) originating from howardites, eucrites, ordinary chondrites and an unclassified object.
257 Spectra IDs and corresponding meteorite names are given in the supplementary material (Table S1).

258 Figure 1 displays the resampled meteorite data for the two most significant parameters (750/917 [nm]
259 vs. 965/917 [nm], right panel) to distinguish different lithologies on Vesta (i.e., howardites, eucrites,
260 diogenites and olivine-rich regions as well as areas contaminated by 'dark material'). These ratios are
261 especially sensitive to the pyroxene absorption band position and the band strength, which are the main
262 FC-covered spectral variations observed on Vesta (Fig. 1 and e.g., Le Corre et al., 2011; Reddy et al.,
263 2012b; Thangjam et al., 2013). The left panel of Figure 1 illustrates four representative spectra of a
264 diogenite (red), eucrite (yellow), olivine (green) and carbonaceous chondrite (dark blue) and the relevant
265 filter positions (grey dashes). This Figure best illustrates the differences of eucrites and diogenites in
266 terms of pyroxene band position and its effect on the ratio 965/917 [nm] as previously described. In
267 section 3.4, the right panel of Figure 1 will serve for comparisons with Vestan FC data, which are
268 extracted for different locations from global HAMO mosaics. As there is no uncertainty available for
269 the RELAB measurements, we do not apply any error bars to the data points and as the data are displayed
270 as ratios, possible systematic uncertainties regarding the measurements or the responsivity functions are
271 cancelled out. The instrument error of the RELAB spectrometer is given as 0.25 % which is smaller than
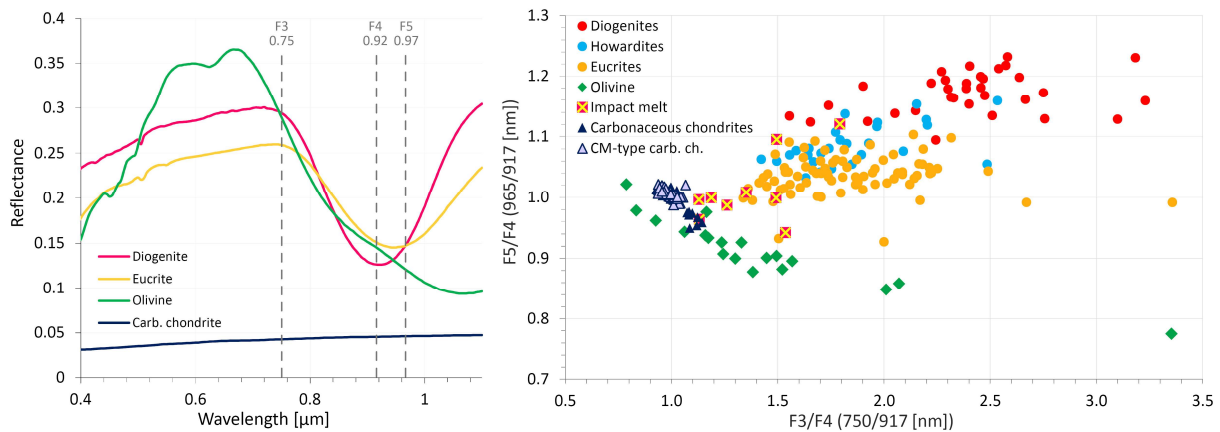272 the data points' symbols in Figure 1.

Fig. 1: Left panel: Wavelengths vs. Reflectance of four different rock types. Dashed vertical lines indicate filter positions of the FC filters used in this study. Diogenite = Ellemeet (ID bkr1mp113), eucrite = ALHA81011 (ID bkr1mp122), olivine from Chassigny (ID bkr1dd001) and Carbonaceous chondrite = Mighei (ID bkr1ma062). Right panel: 750/917 [nm] vs. 965/917 [nm] for resampled RELAB meteorite and olivine data.

We did not use all suitable spectra from the RELAB database. Eucrites with a known oxygen isotopic anomaly (PCA91007, A-881394, Pasamonte, GRA 98098, EET 87542, PCA 82502, NWA 011; Scott et al., 2009; Mittlefehldt et al., 2016) were excluded from the original dataset as they possibly originate from another object (Scott et al., 2009; Mittlefehldt et al., 2016). Furthermore, we excluded samples where distinct "bright" or "dark" spots of the meteorite were measured (mentioned in the comment column of the RELAB sample catalog).

Terrestrial weathering can alter a meteorite significantly, depending on its original mineralogy and the time and place spent on Earth. In particular, the most common changes due to weathering appear as the formation of iron (oxy-) hydroxides and water-bearing phases. The reflectance spectrum of a meteorite can therefore also be affected, which especially applies for meteorites that were found on Earth in contrast to observed falls that have not experienced prolonged terrestrial weathering. Iron oxyhydroxides strongly absorb in the ultraviolet region and water-bearing phases add, amongst others, an absorption near 3 μm (Salisbury & Hunt, 1974). Thus, they do not affect the wavelength area of the pyroxene absorption, which is studied here.

We still investigated a possible influence of weathering and identified falls and finds amongst our meteorite samples as well as the weathering grade of finds (where available, source: Meteoritical Bulletin, publicly available under https://www.lpi.usra.edu/meteor/). We plotted the different meteorite types according to these data and found no influence of weathering on the used FC-based filter ratios (750/917 [nm] and 965/917 [nm]). Furthermore, we confirmed this observation by using the Salisbury and Hunt (1974) approach. They showed for various meteorites that the 500/600 [nm] slope positively correlates with the formation of a water band at 3 μm, which develops under the oxidizing conditions on Earth. We therefore used the 500/600 [nm] ratio to confirm that the meteorites we used are not

301 significantly affected by terrestrial weathering. The respective plots for each meteorite type separated
302 into falls and finds can be found in the supplementary material (S2).

303 Thirteen more meteorite spectra were used to investigate the influence of particle size on the spectral
304 parameters displayed here, which will be discussed in section 4. These meteorite data were provided by
305 Dr. Edward Cloutis and measured at the University of Winnipeg's Planetary Spectrophotometer Facility
306 (e.g., Cloutis et al., 2013a and 2013b). We resampled the spectra according to equation (1).

307

308 3   The PIDs associated with Marcia crater

309 3.1   Regional overview

310 In order to examine the PIDs and identify the process driving the formation of these features, it is
311 necessary to take their surrounding into consideration, especially the spectral and geomorphologic
312 features of Marcia and Calpurnia craters and their ejecta. Figure 2 displays the broad Marcia region as
313 seen through clear filter LAMO images (a), our HAMO RGB composite (b), DTM data (c) and the 2.8
314 µm absorption depth (Combe et al., 2015) (d). In Figure 2b, green and cyan colors indicate material with
315 higher reflectance and pyroxene band strength, while red colors indicate regions with lower reflectance
316 and pyroxene band strength values (R= 965/917 [nm], G=750 nm and B=750/917 [nm]). In Figure 2d,
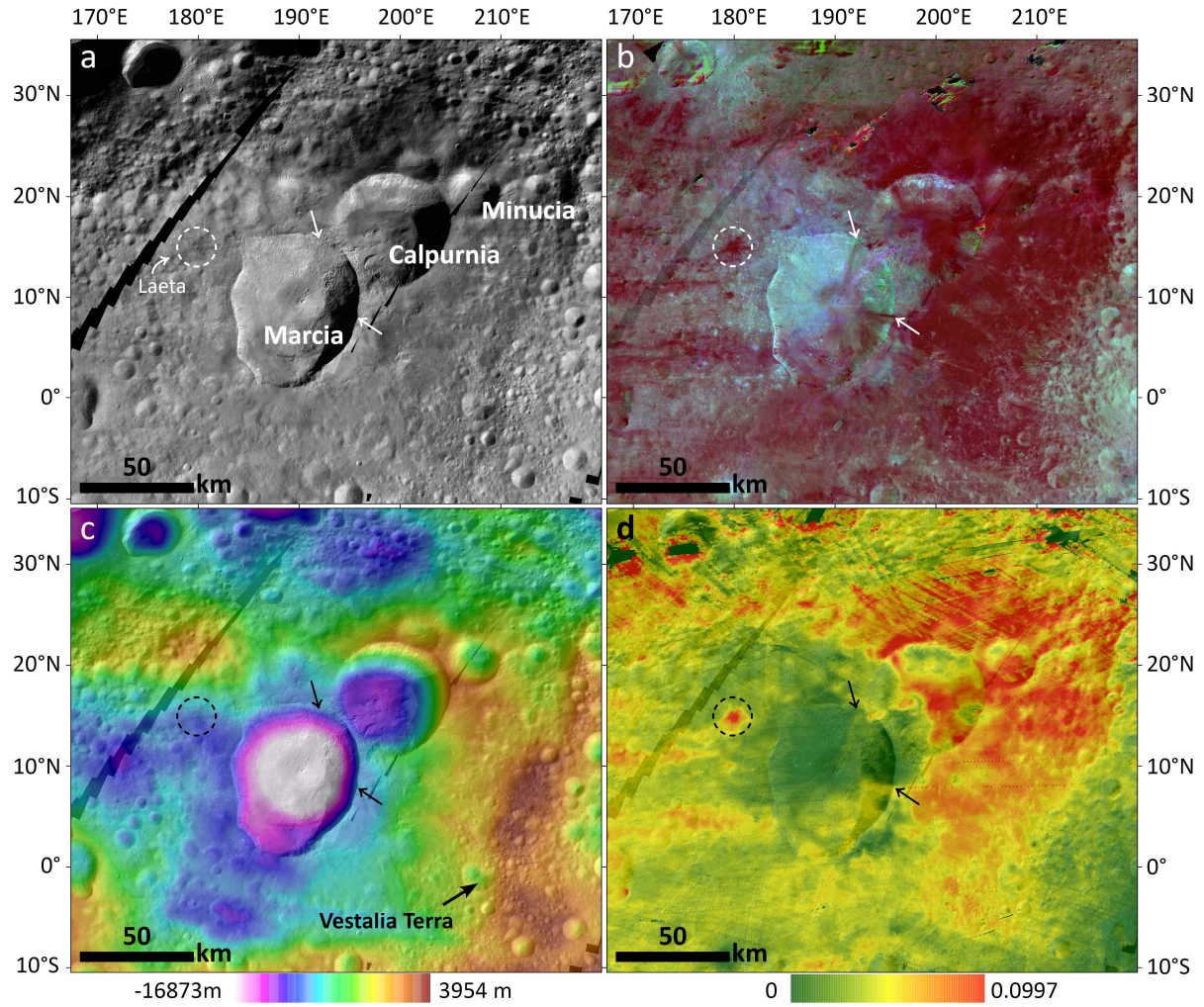317 dark green colors indicate lower OH content whereas red colors indicate higher OH content.

Fig. 2: Spatial and spectral context of Marcia crater and its broad surrounding. a) LAMO clear filter data. This is also the base layer for the other panels, b) HAMO RGB composite (R= 965/917 [nm], G=750 nm and B=750/917 [nm], 20% transparency), c) DTM (50% transparency), d) VIR 2.8 µm band depth map from Combe et al. (2015) (30% transparency). The arrows just east and northeast of Marcia indicate input of material from the rim into the crater which will be explained later on. Dashed circle NW of Marcia indicates Laeta crater.

Figure 2 illustrates distinct regional differences in spectral and geomorphological properties. In general, regions with higher OH absorptions correlate well with regions of lower reflectance and pyroxene band strength. The NW and center of Marcia crater are strongly depleted in OH with respect to other regions nearby. A few km off the rim in the E and NE, a well-defined boundary between brighter/OH-depleted material and darker/OH-enriched material is visible (Fig. 2b and d). We use this boundary to define two different units of Marcia (and/or Calpurnia) ejecta (Fig. 3): Ejecta unit 1 (E1) is generally higher in reflectance, higher in pyroxene band strength (green/cyan in Fig. 2b) and lower in OH abundance (green in Fig. 2d), while ejecta unit 2 (E2) is lower in reflectance, lower in band strength (reddish in Fig. 2b) and higher in OH abundance (orange/red in Fig. 2d). In E2, pre-existing craters and topography are largely overprinted by Marcia ejecta and hardly recognizable whereas numerous pre-existing craters can be observed in E1, indicating that E1 is thinner than E2.
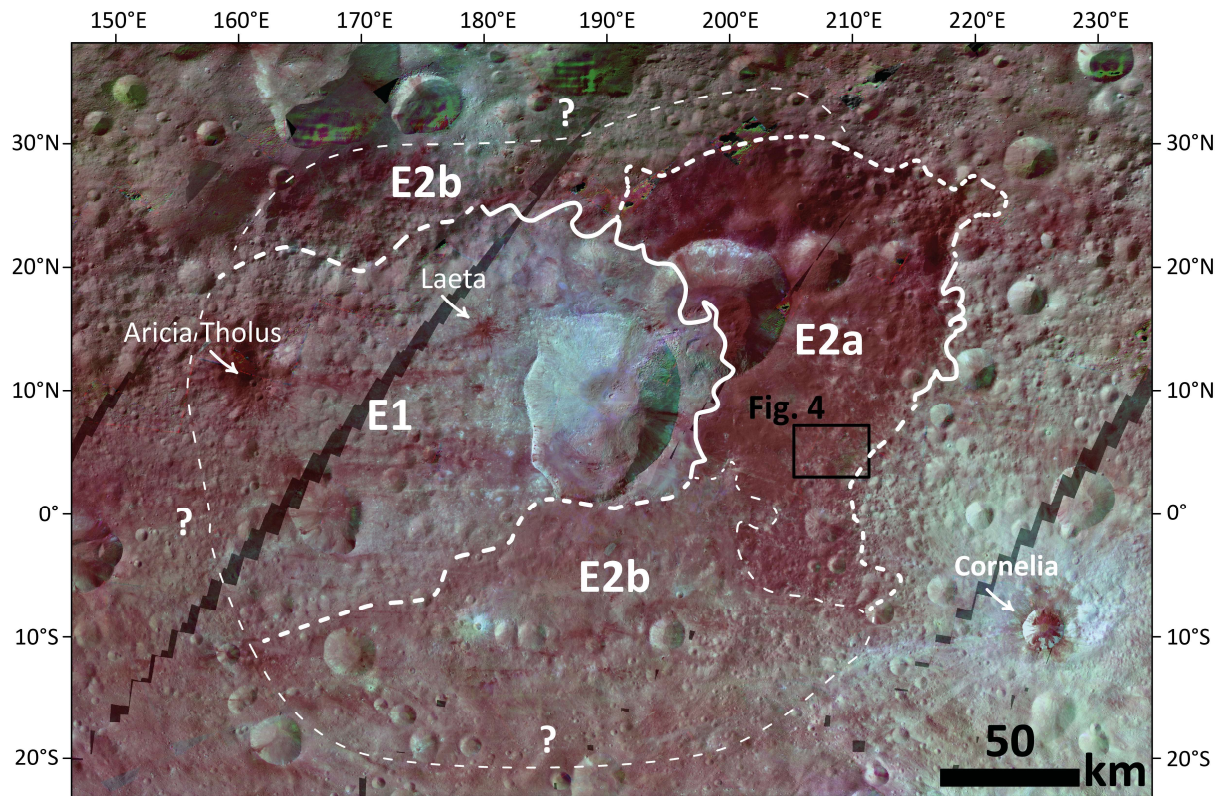
336

Fig. 3: Map of the ejecta units E1, E2a and E2b. Clear filter LAMO data overlain by our RGB composite (R=965/917 [nm], G=750 nm and B=750/917 [nm], 50% transparency). Solid line indicates clear boundary, dashed lines indicate approximate boundaries and faint dashed lines indicate uncertain boundaries. Cornelia crater is displayed in this map on the lower right.

341

We further subdivided E2 into E2a and E2b, where E2a is strongly influenced by the presence of Vestalia Terra, a mountain range to the east of Marcia (Fig. 2c), and characterized by lobate slope deposits, lobate uphill features as well as lower reflectance/pyroxene band strength and slightly higher OH absorption values than E2b. Figure 4 illustrates lobate uphill features as well as lobate slope deposits in E2a. E2b does not feature these specifics but is still lower in reflectance and pyroxene band strength than E1 and also shows larger 2.8 μm absorptions band depths than E1. Moreover, the OH-rich spectral signature of E2a ends quite abruptly near the top of Vestalia Terra and overlaps well with lobate uphill features (Fig. 4d). The high OH abundance is therefore strongly tied to ejecta.

As material of E2a is correlated with thick ejecta, subsequent space weathering processes (Pieters et al., 2012) probably foremost reworked the ejecta and not pre-existing regolith. Therefore, spectral characteristics of this ejecta unit might still be very similar to the characteristics of the original ejecta. Table 1 summarizes the spectral properties of the presented three ejecta units and displays that, in comparison with the whole Vesta, Marcia (and Calpurnia) ejecta are generally darker and richer in OH than the average of Vesta (as observed before by De Sanctis et al., 2012b and Combe et al., 2015). Data

356   for E1 in Table 1 do not include areas obviously contaminated by dark material (e.g. Laeta crater within

357   E1, dashed circle in Fig. 2; Jaumann et al., 2014).

	Mean 750 nm reflectance	Mean 750/917 [nm]	Mean 2.8 μm band depth	n (pixel number)
E1	0.185 ± 0.010	1.443 ± 0.042	0.031 ± 0.003	755,550
E2a	0.142 ± 0.012	1.291 ± 0.114	0.048 ± 0.006	1,675,878
E2b	0.161 ± 0.014	1.346 ± 0.041	0.038 ± 0.006	1,918,785
whole Vesta	0.194 ± 0.034	1.455 ± 0.133	0.030 ± 0.009	$3.56 * 10^8$

362

363   Figure 3 displays E1, E2a and E2b mapped over clear filter LAMO images and faint overlain HAMO

364   RGB composite. Laeta crater NW of Marcia excavated dark material with the same spectral

365   characteristics as E2a, suggesting that E1 superposes E2a. The spectral signatures of E1 and E2b

366   gradually attenuate to the west, south and north. The boundary we mapped in these regions is

367   approximate and based on lobate features that we observed and interpret as ejecta flow fronts (similar

368   to the example in Fig. 4a, white arrows). The extent of Marcia and Calpurnia ejecta is larger than what

369   was mapped by Williams et al. (2014a) on the basis of geomorphologic observations at a resolution of

370   260 m/px (Survey orbit).

371   It is still under debate whether the OH-rich ejecta unit (E2a) results from the Calpurnia or Marcia impact.

372   The spectrally very different ejecta units E1 and E2a clearly suggest different origins. However, the

373   relationships of E1 and E2a are not easily unraveled. For example, E1 clearly appears to superpose E2a

374   (e.g., as seen at Laeta crater and within Calpurnia), yet just east of Marcia, material from E2a seems to

375   merge into E1 and overprint it. The extent of E2a favors an origin in the older crater Calpurnia, yet the

376   shape of the Vestalia Terra highlands coincide with the shape of the OH-rich and dark margin of E2a,

377   possibly leading to the current shape by coincidence und thus questioning Calpurnia as the origin of

378   E2a. Moreover, there are no PIDs occurring north of Calpurnia. Furthermore, E2b spectrally appears as

379   a mixture between E1 and E2a und its extent is not readily explained by two craters forming at different

380   times. In summary, we are fairly confident that the majority of E1 materials originate from the Marcia-

381   forming impact event, yet we are less confident that all of E2 can be assigned to Marcia and may actually

382   originate from Calpurnia. This would also suggest a possible oblique impact angle for the Marcia

383   projectile, as E1 is distributed asymmetrically around the crater.

384   While it is likely that at least E2a originates from Calpurnia, we will refer to all PIDs in this area as one

385   large occurrence. As all of the ejecta units appear well-preserved, a large age difference between

386   different PIDs and therefore different preservation states can be excluded. Modeled ages from crater-

387   counting methods could not show definite age differences between these different ejecta units (Williams

388   et al., 2014b, Appendix A), though model age determination shows an increased uncertainty for 'young'

389   ejecta blankets (e.g., Williams et al., 2018). It might also be plausible that the Calpurnia and Marcia

390   impactors once built a binary object with different compositions, impacting on Vesta nearly

391 simultaneously with the Calpurnia impactor hitting just before the Marcia impactor. This could also
392 explain the mobility of E2a, slumping into Marcia crater after its final formation as well as the
393 'intermediate' ejecta unit E2b. While the distinction of ejecta units is important for our observations, the
394 determination of the parent crater of PIDs in the broad Marcia region is not a key element in this study
395 and independent from our findings. This is why we will only address this marginally.

396 Figure 5 displays our mapped PIDs and indicates craters that existed prior to Marcia and now host PIDs
397 in blue circles. We mapped in total 118 individual PIDs. Some PIDs might be part of a bigger cluster or
398 could be subdivided into smaller units as identification of boundaries is limited due to the given image
399 resolution. 41 of the 118 PIDs mapped are located in E1, 21 in E2a and 39 in E2b. The remaining PIDs
400 are situated within the crater. Additionally, we identified 13 pre-existing craters that host one or more
401 PIDs (excluding the large craters Calpurnia and Minucia). Nine of those craters are situated in E1 and
402 four of these craters in E2b. More details will be discussed and shown in section 3.2. Figure 5b, c and d
403 display high-resolution examples of PIDs whereas 5b is situated in E1, 5c in E2b and 5d is part of the
404 crater-fill PIDs. In this study, we refer the term 'crater-fill' only to the PIDs around Marcia's central
405 peak and not to PIDs on the mentioned southern terrace of Marcia (see Fig. 5 for spatial context) as this
406 material most likely represents material thrown out of the transient cavity during crater formation before
407 the crater wall collapsed. Figure 6 serves as spatial orientation for close-up images presented in the
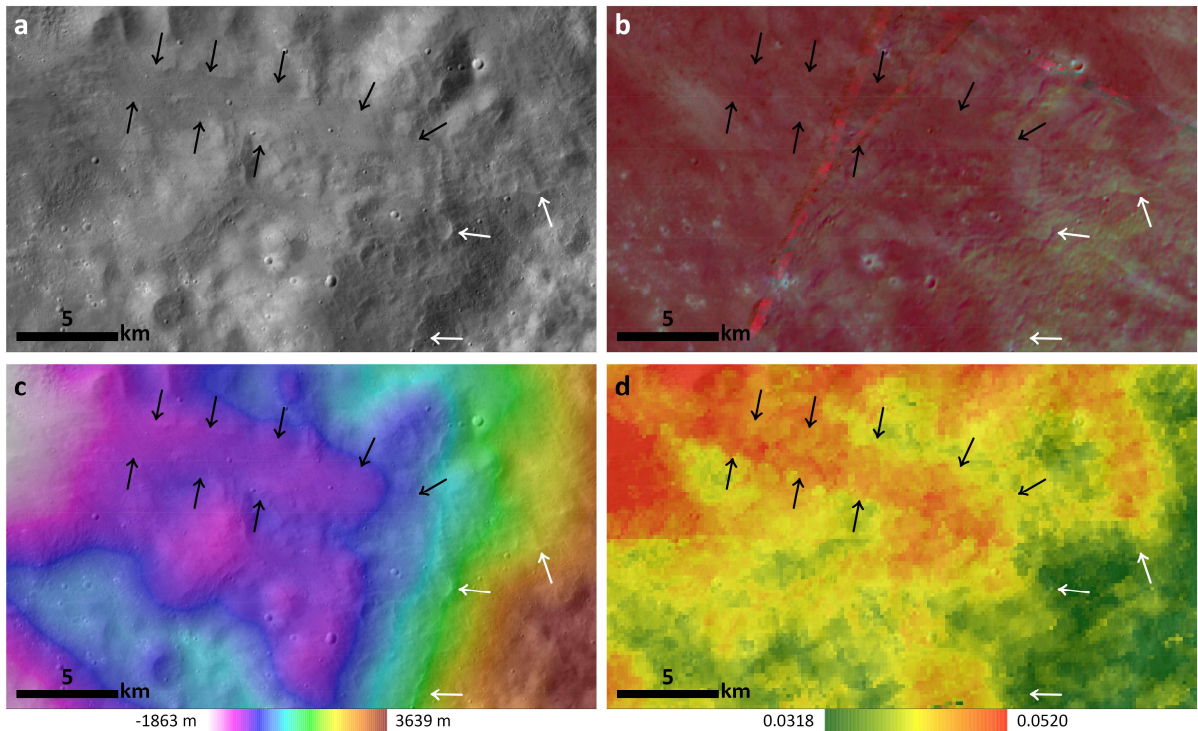408 following sections.

409

410
411 Fig. 4: Lobate uphill features (white arrows) and lobate slope deposit (black arrows) in E2a, for spatial context see Figure 3. a)
412 LAMO clear filter data, b) HAMO RGB composite (R= 965/917 [nm], G=750 nm and B=750/917 [nm]), c) DTM (50%

413 transparency) over LAMO clear filter data, d) VIR 2.8 μm band depth map from Combe et al. (2015). Straight red lines in b)

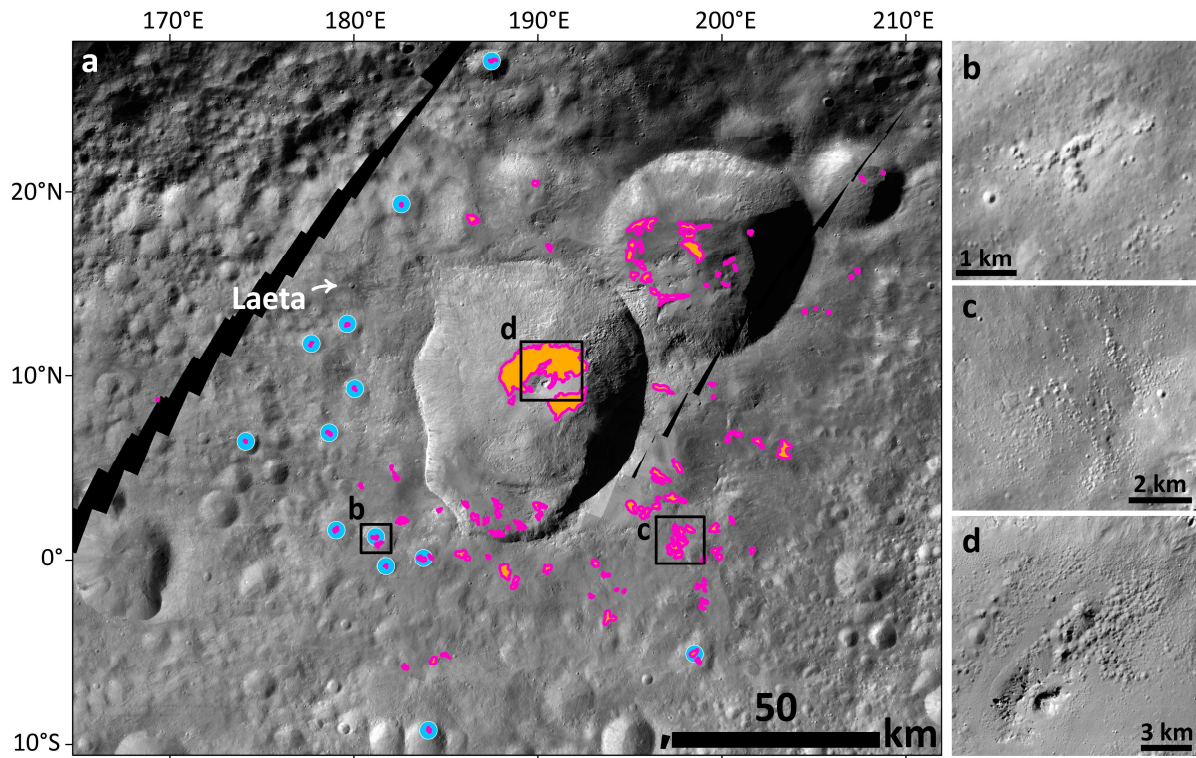414 indicate artefacts from the mosaicking process.

415

416 Fig. 5: a) Distribution map of PIDs (in total 118 individual terrains) associated with Marcia ejecta (LAMO clear filter). Blue

417 dots denote small craters housing PIDs which will be described in section 3.2. b), c) and d) examples of PIDs. b) is situated

418 within E1, c) is situated within E2b and d) is part of the crater-fill PIDs.
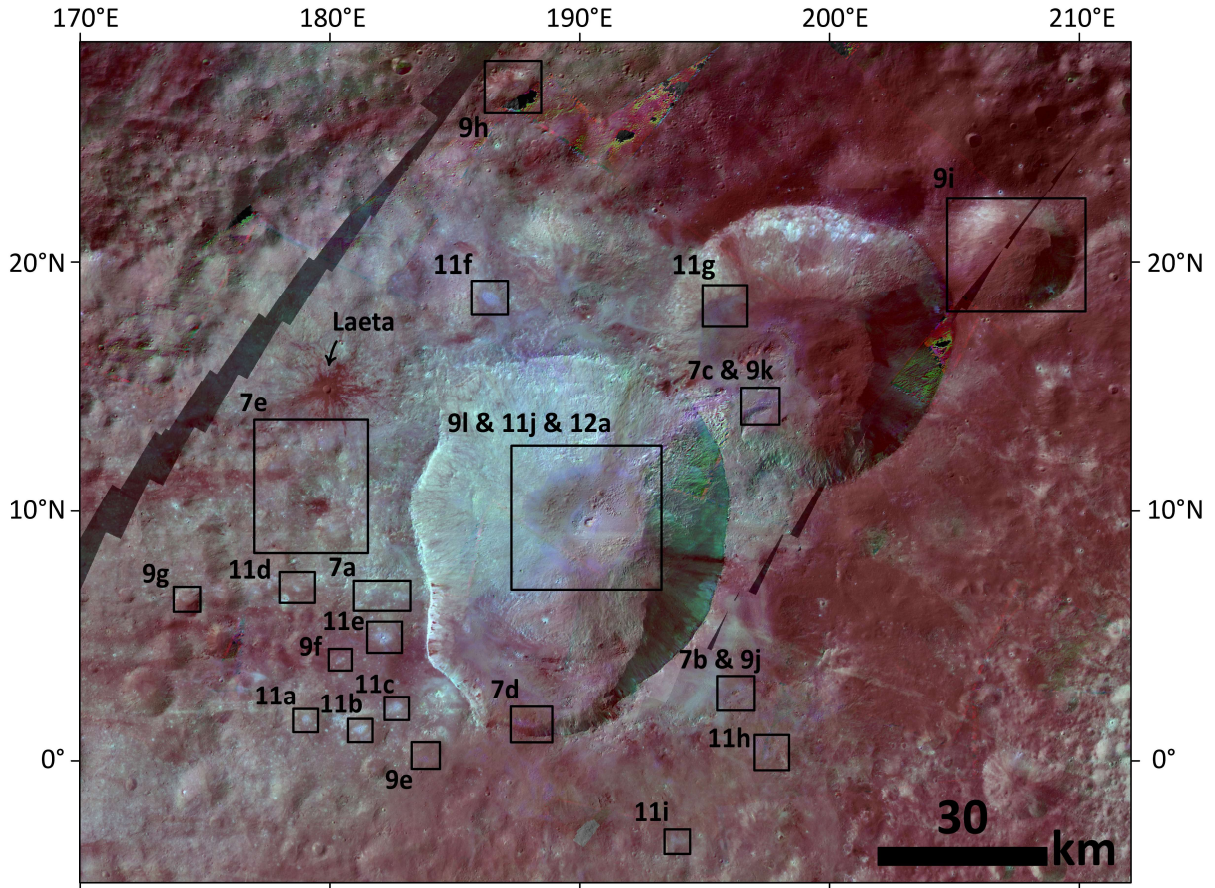
419

420

Fig. 6: Spatial context of locations presented throughout this study. Clear filter LAMO data overlain by our HAMO RGB composite (R= 965/917 [nm], G=750 nm and B=750/917 [nm], 50% transparency).

3.2   Geomorphological characterization of the PIDs

Identifying a PID on the basis of its visual appearance is not trivial as a range of possible morphologies indicating volatile loss can be observed within the ejecta blanket of Marcia. PIDs have been defined as clusters of individual, irregular shaped, rimless pits (Tornabene et al., 2012; Denevi et al., 2012). However, already the identification of a cluster of pits is challenging on Vesta. Figure 7a displays an example of 'possible' PIDs. The pits are not densely clustered but rather individually located in each other's vicinity and could therefore also represent secondary cratering or later impacts. Limited image resolution prevents an analysis of single pit and potential ejecta morphology. A secondary impact origin (i.e., post-Marcia) can therefore not be excluded for these pits although they appear to only occur in smooth deposits as do the PIDs. Moreover, their spectral characteristics are also consistent with PIDs (i.e., cyan colors in our RGB composite, Fig. 7a, lower panel; more details on the spectral characteristics in section 3.3). Those 'possible' PIDs can be observed especially within E1 and their presence indicates a more widespread and pervasive devolatilization process than previously suspected. We did not include the particular feature from Figure 7a into our counts but several others not mapped in Denevi et al.

439 (2012). The identification of a cluster of pits is biased and strongly depends on the individual mapping
440 the feature. Several 'possible' PIDs were not included due to identification uncertainty.
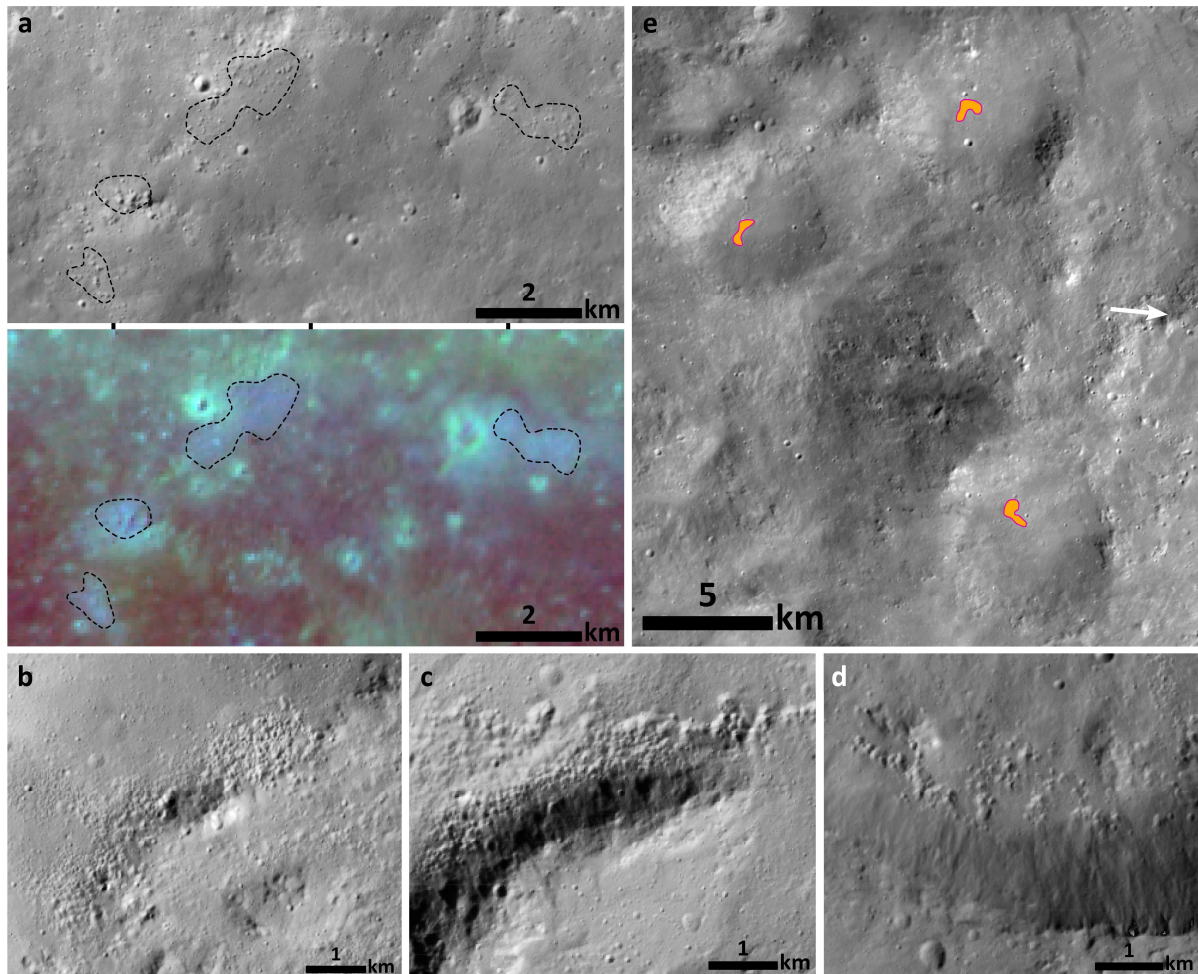

441

442 Fig. 7: a) 'Possible' PIDs (dashed lines) with a lack of obvious clustering and distinct pit morphology but showing the
443 characteristic spectral properties of PIDs (upper panel: clear filter LAMO image, lower panel: HAMO RGB composite). b), c)
444 & d): Examples of PIDs that exist adjacent to a topographic high. e) Example of three PIDs west of Marcia which are situated
445 in craters (yet do not exhibit a detectable positive topography); colored polygons indicate PID (as in Fig. 5). For spatial context
446 of a)-e) see Fig. 6.

447

448 Excluding the crater-fill PIDs around Marcia's central peak, PIDs have an average areal extent of a few
449 square km (1.9 km^2) and roughly range from less than 10 to more than 80 individual pits per cluster. As
450 individual pits often reach the resolution limit, we point out that counting of individual pits and
451 measuring pit diameters occurred for representative clusters only. The diameter of individual pits ranges
452 from less than 50 m (resolution limit) to more than 500 m with the largest ones occurring within
453 Marcia's crater-fill deposits. The average pit size within ejecta PIDs is 120 m while it is 290 m for PIDs
454 within the crater-fill deposit. This is consistent with what has been observed for Martian PIDs (i.e., pits
455 are largest in crater-fill deposits; Tornabene et al., 2012). An increase in pit size of PIDs on Marcia's
456 southern terrace with respect to those within the ejecta was not observed. Numerous PIDs show many

17

457   'possible' smaller pits (i.e., dark individual pixels as possible pit wall shadows), which cannot be
458   identified with confidence due to the limited image resolution. A dependence of PID size vs. parent
459   crater diameter seen on Mars (Tornabene et al., 2012) is hardly derivable for Vesta as the number of
460   parent craters is very low, yet we report crater diameter vs. the largest pit within the crater-fill deposit
461   for the four parent craters reported in Denevi et al. (2012): Marcia, 63 km vs. ~1300 m; Cornelia, 15 km
462   vs. ~280 m; Licinia, 22 km vs. ~400 m (if devolatilization pit exists), Numisia, 30 km vs. ~590 m (if
463   devolatilization pit exists).

464   The depth of the individual pits can also not be resolved by the existing data, yet an assumption of depth
465   by considering shadows and incidence angles gives a rough average depth of 25-50% of the pit diameter,
466   though smaller and higher values are observable as well (e.g., Fig. 8h shows relatively shallow pits).
467   PIDs appear to be flatter in E2a and E2b. These values are higher than what Tornabene et al. (2012)
468   found for Martian PIDs (pit depth ~ 0.1 pit diameters). Boyce et al. (2012) present a rapid formation
469   model for the PIDs where steam release is expended in days to weeks after deposition, strongly
470   depending on the volatile content and energetics of the degassing process. Lower volatile contents within
471   the hot ejecta deposits of the Marcia impact would be exhausted earlier. This could produce steeper pits
472   as the vents on the top progressively widen with time (Boyce et al., 2012). A lower gravitational
473   acceleration can also increase the steam escape rates (Boyce et al., 2012) which could favor the
474   formation of steeper pits. However, Sizemore et al. (2017) applied the Boyce et al. (2012) model for
475   Cerean pits and found that they are broadly comparable on Ceres and Mars.

476   The shape of individual pits within a PID appears more cone-like and less bowl-shaped as for nearby
477   small craters which is helping the identification (as can be observed in e.g., Fig. 5a & b, Fig. 12).
478   Assuming a conical shape for the pits and a depth of the respective pit radius (upper limit), we calculated
479   volumes (Table 2) of the now lost volatiles of the PIDs shown in Figure 11, divided into the crater-fill
480   PIDs around the central peak and all other PIDs (incl. PIDs on the southern terrace of Marcia). The
481   calculations assume that the voids within the pits equal the volume of volatiles released which is a rough
482   simplification. The given volumes are therefore upper limits as other materials might also have been
483   extracted during this process (Boyce et al., 2012) and are part of the volume now lost. We measured
484   only the largest pits within a cluster as smaller pits are close to the resolution limit and do not contribute
485   significant amounts to the total volume. We interpolated the values of the representative PIDs shown in
486   Figure 11a-i to infer the total amount of volatiles lost for all PIDs (except the crater-fill PIDs).

487   Table 2 summarizes the calculated volumes and shows that a higher volume of volatiles has been
488   released from the crater-fill material than from the ejecta material. The volume per km^2-value for the
489   crater-fill PIDs is more than twice the value of the other PIDs which likely results from the difference
490   in pit size and volume of the initial crater-fill impact deposit. If Calpurnia is the source of E2a PIDs, the
491   difference between the volatile volumes of Marcia crater-fill PIDs and external PIDs is even larger. The
492   individual pits measured within the crater-fill material are on average significantly larger than elsewhere

493 (290 m vs. 120 m) and moreover the largest connected crater-fill PID is 145 km^2 while the largest PID

494 elsewhere is around 13 km^2. This illustrates a significant difference between crater-fill PIDs and

495 elsewhere around (or on the southern terrace of) Marcia crater. In summary, the total volumes of lost

496 volatiles are similar for the PIDs around the central peak and all other PIDs altogether, yet the number

497 of volatiles per km^2 and the connected area of pitted terrain is larger for the crater-fill PIDs.

498 **Table 2**
499 Estimates of lost volatile volumes due to explosive devolatilization.

	Area [km^2]	Volume [m^3]	Volume/km^2
PIDs Fig. 11a-i	~ 29	$\sim 7*10^7$	$\sim 2.3*10^6$
All PIDs (excl. crater-fill)	~ 212	$\sim 5*10^8$	$\sim 2.3*10^6$
Crater-fill PIDs	~ 180	$\sim 9*10^8$	$\sim 5.0*10^6$

500

501 The PIDs are not distributed uniformly around the crater. Most clusters are found from the SW to the

502 SE and inside Calpurnia (see Fig. 5), but a few also occur in other areas. All of the external PIDs are in

503 proximal distance to the crater rim (i.e., about one crater diameter). Figure 8 illustrates the dependency

504 of distance vs. number of PIDs as well as distance vs. area of the PIDs for all PIDs external to Marcia.

505 The farthest PID is located 69 km off the crater rim (within Minucia crater) while about 50% of the PIDs

506 are located within 20 km off the crater rim and 73% are located within 30 km (i.e., one crater radius).

507 On average, PIDs within E1 (blue circles in Fig. 8b) are slightly larger than PIDs elsewhere (2.2 km^2 vs.

508 1.8 km^2) and are located closer to Marcia than PIDs within E2a (red diamonds) and E2b (orange

509 squares). This might reflect the thinning of the ejecta with distance from Marcia and therefore the

510 decrease in pit size and abundance. This relationship has been observed for Mars as well (Tornabene et

511 al., 2012).

512 PIDs are less abundant within 10 km off the rim than at 10-20 km (Fig. 8a). This could have several

513 reasons. The most likely explanation is that post-impact modification processes (slumping, collapsing)

514 prevail in the closest regions to the rim (e.g., Melosh, 1989) and might have overprinted existing PIDs.

515 Furthermore, the considered area increases with distance, i.e. so that the number of PIDs/km^2 is nearly

516 identical for the first two columns (assuming an elliptical shape for Marcia with a = 27 km, b = 34 km)

517 before this value drops significantly for distances > 20 km. Lastly, E2a PIDs possibly originate from

518 Calpurnia and therefore do not naturally occur near the rim of Marcia, possibly adding to this slight
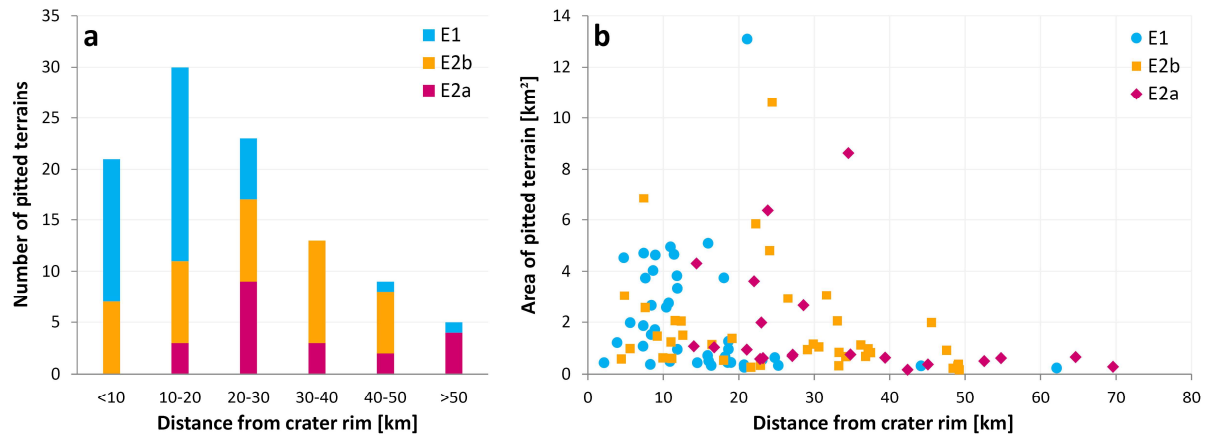
519 variation in PID distribution.

Fig. 8: a) Distance of PIDs from Marcia crater rim (closest distance) vs. the number of PIDs occurring within the given ranges. b) Distance of PIDs from Marcia crater rim (closest distance) vs. the area spanned by the individual clusters separated into the three different ejecta classes within which they occur (see section 3.1).

Higher numbers of individual pits within a cluster imply a higher local volatile content, assuming that PIDs are related to volatile outgassing (Tornabene et al., 2012; Boyce et al., 2012; Denevi et al., 2012). Individual pits in the clusters do not always overlap and the arrangements of individual pits within the clusters often do not seem to follow any systematics. The clusters exhibit diverse shapes (circular, circular with a lack of pits in the center, oval, polygonal or as directional 'pit chains', see Fig. 11), which illustrates a heterogeneous distribution of the degassing conduits within the host material. The 'soap froth' pattern of PIDs described in Tornabene et al. (2012) and Boyce et al. (2012) is present at multiple PID locations (best-developed within the crater fill-deposits), yet many PIDs do not feature shared rims and this extensive close packing which can be seen in Figure 5 and 11. This is likely due to the lower availability of volatiles on Vesta with respect to Mars and the concomitant decreased duration of volatile loss. Intervening smooth regions between pits also occur frequently (best illustrated in Fig. 11 in section 3.3) which has also been reported for Martian PIDs (Tornabene et al., 2012).

PIDs always occur within 'smooth material' (Denevi et al., 2012; Williams et al., 2014a), which could be impact melt or an impact melt-bearing breccia linked to Marcia ejecta. A connection of pitted material with fluid flow features and smooth melt-bearing impact deposits was also observed for Mars and Ceres (Tornabene et al., 2012; Sizemore et al., 2017). This smooth material is characterized by very few and small impact craters and an even surface appearance within the resolution limits. PIDs are mostly located on slight slopes (~ 2°-15° with respect to the triaxial ellipsoid, see section 2.1) and with minor exceptions (e.g. in Calpurnia & Minucia craters), these slopes are facing the direction from where Marcia ejecta were excavated (e.g., Figure 7e, white arrow indicates the direction towards the Marcia center). These slopes are consistent with the slope range in which Martian PIDs are present (< 15°, Tornabene et al., 2012), indicating that the critical slope below which pits can form is independent of the body's gravitation. Within Calpurnia and Minucia, PIDs occur near the margins of the crater-fill deposits, at the lowest elevations and at topographic highs (i.e. crater wall, large blocks).

549   Furthermore, we found 17 PIDs located within 13 relatively small craters (2-9 km, see Fig. 5) that

550   existed prior to the Marcia impact (as seen by smooth rims and ejecta-filled crater interiors, e.g. Figs.

551   7e and 11d). In this consideration, we exclude the large craters Calpurnia and Minucia due to possibly

552   misleading statistics and interpretations. These small pre-existing craters occur foremost in E1 (compare

553   Figs. 3 and 5) and there are no small pre-existing craters hosting PIDs within E2a. Some ambiguous

554   'craters' hosting a PID were found but not included here. Moreover, we identified several locations

555   where the DTM shows a positive local topography (bulge) linked to the PIDs.

556   Another important observation is that some PIDs occur near or directly at topographic highs, i.e., the

557   pits are aligned and densest where the deposit is in contact with crater walls and ridges/large blocks.

558   This can be observed, for example, a few kilometers SE of Marcia (Fig. 7b), within Calpurnia (Fig. 7c)

559   and at the Marcia southern crater wall (Fig. 7d). PIDs are clearly aligned along these features, indicating

560   a structural control on the formation of PIDs.

561   Figure 9 illustrates twelve profiles of PIDs where a PID is connected to positive local topography, is

562   identified within a pre-existing small crater or is aligned along a topographic high (9k). The red part of

563   the current topography indicates a pitted surface and the dashed grey line indicates an approximate

564   putative surface profile without overlying ejecta assuming the steepest parts of the slopes/crater walls

565   still display the pre-Marcia-impact topography (simple bowl shape for craters). The 'halo' (yellow part

566   of the current topography) within Marcia is a spectrally distinct part of the crater-fill PIDs and will be

567   described in detail in section 3.3. The halo for all other PIDs represents smooth material exhibiting the

568   distinct spectral characteristics of the adjacent PID, which will also be shown in detail in section 3.3. A

569   PID host deposit thus differs greatly in both spectral (i.e., 'dark' and 'bright') and geomorphological

570   (pitted and smooth) characteristics. View Figure 6 for the spatial context of the profiles and the

571   supplementary material (S3) for the exact location and course of the profiles. S3 also includes an

572   indication of the excavation direction from Marcia; e.g., for profiles a, b, c, e and i Marcia ejecta arrived

573   from the right of the profile and for profiles e, h and j, from the left of the profile.

574   The occurrence of a PID therefore appears to be linked to accumulation of volatile-bearing ejecta

575   controlled by pre-impact topography. According to our estimated pre-Marcia topography (dashed line),

576   PIDs mainly reside where the host deposit is thickest, yet they can also occur near the margins of the

577   host deposit (e.g., within Minucia, 9i and along topographic highs). We did not observe a correlation of

578   the 13 presented host crater diameters and area or thickness of the PID deposit. Thus, PID size does not

579   appear to be related to the deposit thickness, possibly as a result of heterogeneous compositions within

580   the ejecta.

581   For the examples in Figure 9, the thickness of the PIDs' material ranges from 20 m to roughly 300 m.

582   In the larger craters Marcia (9l) and Minucia (9i), the thickness of the host deposits might be in the order

583   of ~ 500 m and are therefore significantly larger than the deposits elsewhere. Furthermore, the profiles

584   clearly illustrate that the PIDs are part of larger impact deposits, whose surfaces are otherwise smooth.

585 This is best illustrated where host deposits of PIDs reside in pre-Marcia-existing craters (9a, b, d, e, g,
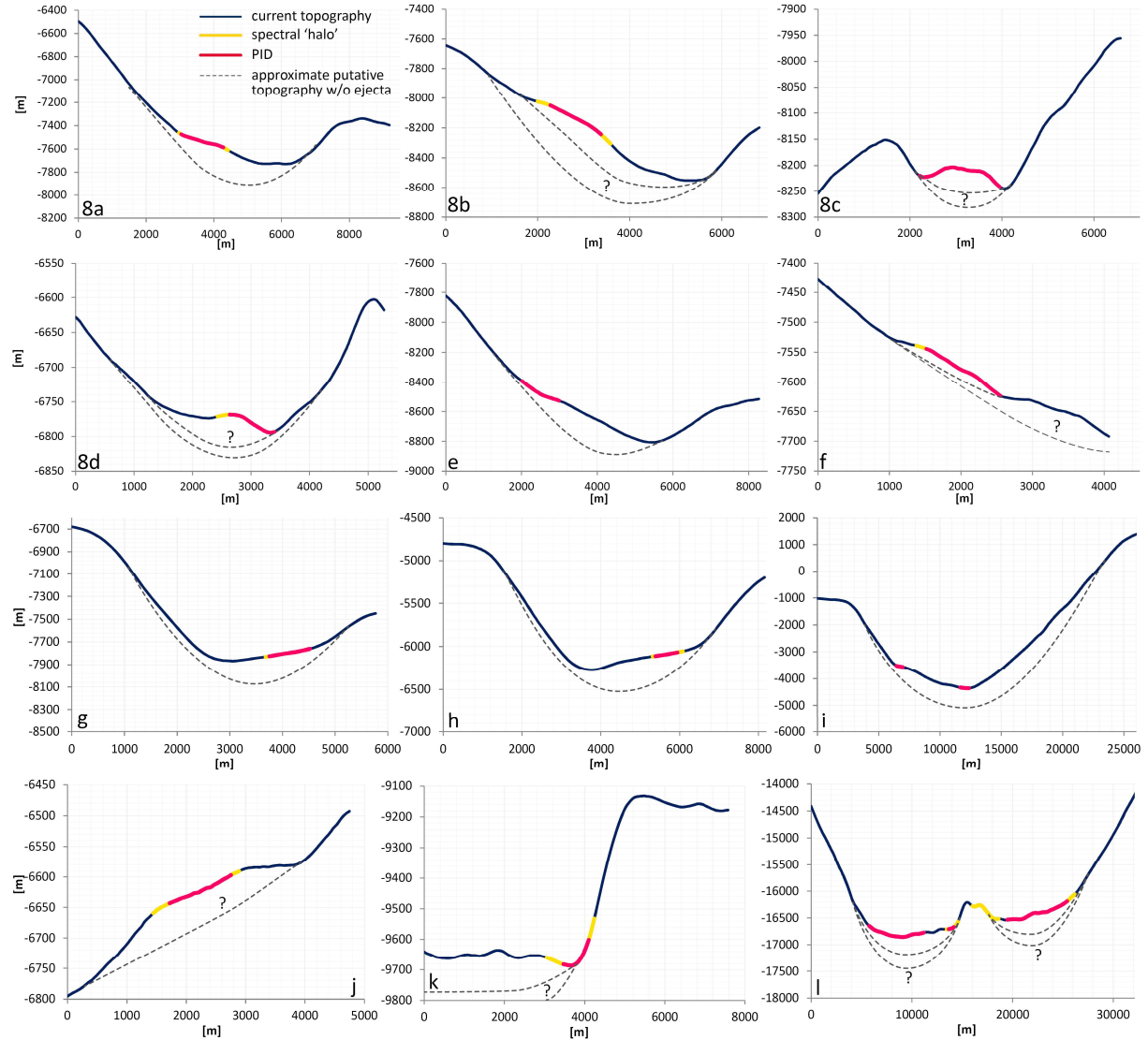586 h, i).

587

589 Fig. 9: DTM-derived profiles: Dark blue line displays the current topography. Dashed line represents the putative topography
590 prior to the emplacement of Marcia ejecta. Red colored part denotes a PID, yellow color denotes the halo around the respective
591 PID and for the Marcia profile (l), also the halo near the central peak not associated with a pitted surface. Spatial context is
592 given in Fig. 6 while exact profile locations are displayed in the supplements (S3). No vertical exaggeration applied.

593

594 3.3   Spectral characterization of the PIDs

595 Williams et al. (2014a) report a "distinctive color signature" of pitted terrain in FC false color ratio
596 images, which they describe as "gray-brown" in the Clementine-type ratios (Pieters et al., 1994; R=
597 750/438 [nm], G= 750/917 nm, B= 438/750 [nm]). This statement applies to the large PIDs on Marcia's
598 floor, which were described by Denevi et al. (2012) and De Sanctis et al. (2015c) to exhibit a spectrum
599 darker than the average of Vesta. However, some PIDs outside of Marcia exhibit a significantly higher

22

reflectance and pyroxene band strength than the average of Vesta or Marcia's crater-fill PIDs. Figure 10 displays FC spectra of nine sample locations and Vesta's average spectrum. Included is also the spectrum of the crater-fill PID within Cornelia crater, which is slightly darker with a higher visible slope than the crater-fill PIDs of Marcia. Cornelia is a very well-preserved, bright crater SE of Marcia (Fig. 3) located on top of the Vestalia Terra highlands that also contains very dark material in its walls and a single PID on its floor (Fig. 7, upper right panel). The contrast between the PID on the floor and bright material within Cornelia crater is higher than the contrast between Marcia's crater-fill PIDs and bright material from its rim, possibly due to age differences between the craters. Figure 10 illustrates that PIDs exhibit stronger absorptions with respect to locations with similar reflectance levels in the visible region. Most notably is the spectrum of the crater (light orange) right next to the PID SW of Marcia (orange) in comparison with the PID itself and also to the halo of the crater-fill deposit. The spectrum of this crater shows a discernably smaller absorption band than the halo and the nearby PID while showing very similar patterns from 400 to 750 nm. We do not show normalized spectra in order to emphasize the different absolute reflectance values of the sample locations.

All PIDs mapped during this study exhibit higher reflectance and pyroxene band strengths (i.e., cyan in our RGB composite) than their immediate surrounding except the crater-fill PIDs, which generally exhibit lower reflectance and weaker pyroxene absorptions with respect to their immediate surrounding. The surroundings of PIDs comprise smooth materials from the same ejecta host deposit (e.g., Fig. 5b, c & d, Fig. 9) which do not exhibit the same spectral characteristics (Fig. 11). The majority of PIDs only exhibit minor differences with respect to their surroundings, but they are still distinguishable (e.g., Fig. 11g-i). In general, the PIDs exhibit an increase in reflectance of up to ~ 7 % at 750 nm (Figure 10). The Marcia crater-fill PIDs are the only ones showing a decrease of reflectance and pyroxene band strength with respect to their immediate surrounding, which will be discussed later on.
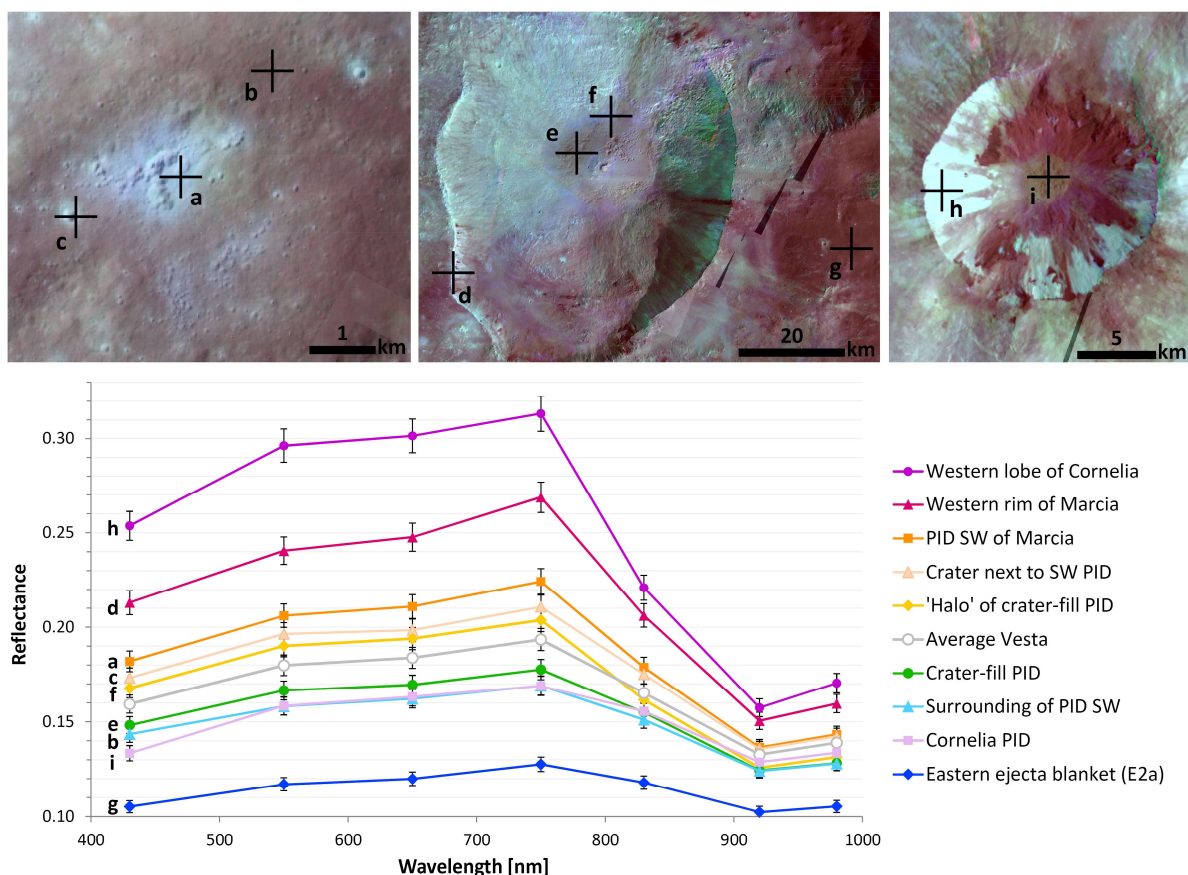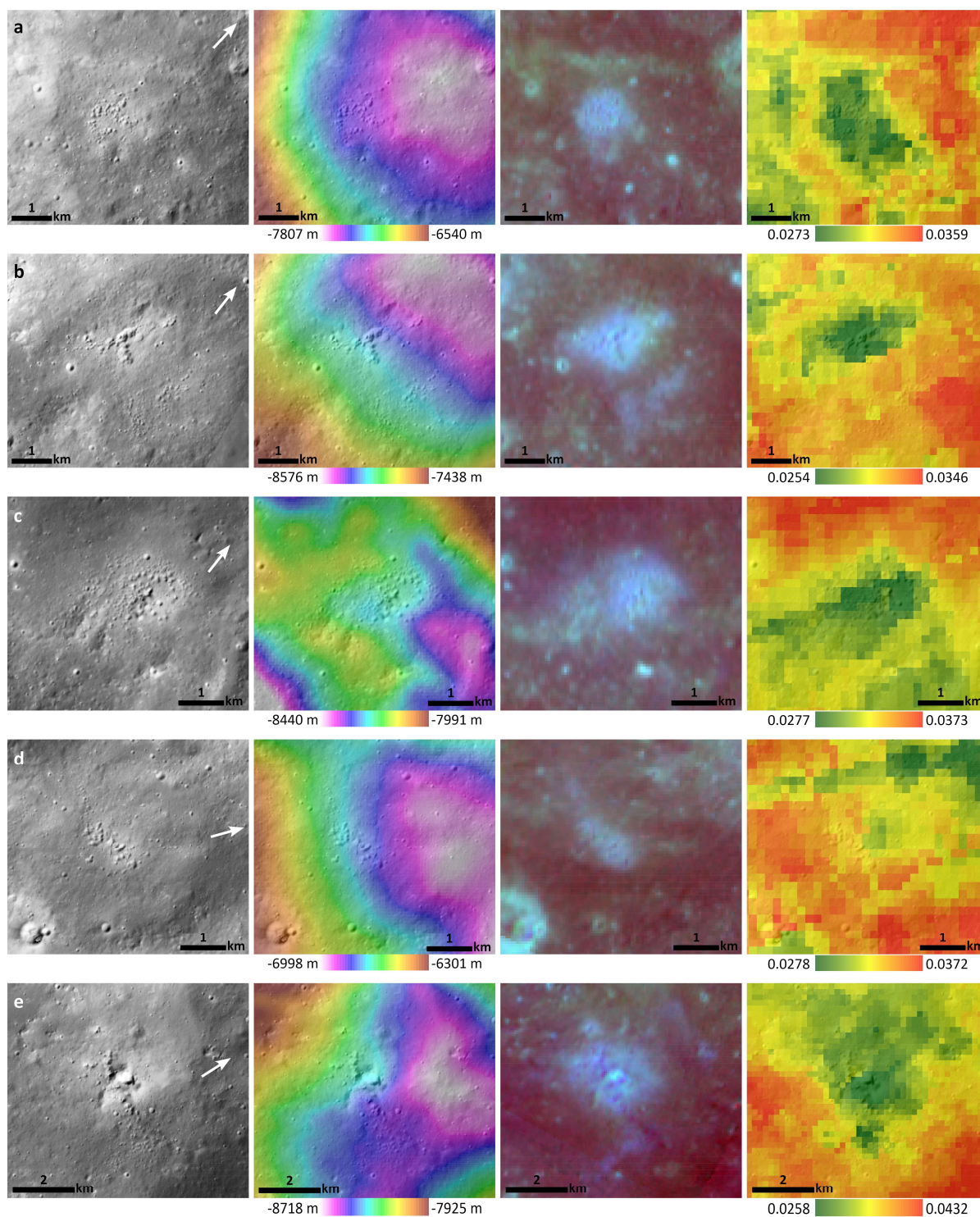
Fig. 10: Upper panel: Spatial context for spectra displayed in lower panel. Lower panel: FC spectra of different regions of interest on Vesta (mostly Marcia-related but for comparison, the Cornelia PID and a bright slope deposit inside Cornelia are shown). Note that reflectance and pyroxene band strength are positively correlated. The vertical error displays 1σ for the Vestan FC data according to the approximate calibration uncertainty after Schröder et al. (2014). Here, an uncertainty of 3% was assumed. The uncertainty is mostly caused by the stray light removal, which varies from image to image and from filter to filter (e.g. Schröder et al., 2014. For spatial context of the upper left two panels, see Fig. 5a & b and for Cornelia crater Fig. 3.

External to the crater, there are numerous examples of spectrally distinct PIDs located in different topographic settings distributed in all directions (see Fig. 5a). Figure 11 displays several examples of the most characteristic PIDs (high 750/917 [nm] and 750 nm values and/or distinct geomorphologic appearance) in clear filter LAMO images (1st panel), topographic setting (2nd panel) and FC false color ratio RGB (3rd panel, R= 965/917 [nm], G=750 nm and B=750/917 [nm]). Reflectance and pyroxene band strength of the PIDs are positively correlated (see also Fig. 10 and Table 3). The 4th panel in each row of Figure 11 displays the absorption band depth at 2.8 μm (i.e., the abundance of OH-bearing minerals) created with VIR data by Combe et al. (2015) who derived the absorption depth from the reflectance between a calculated continuum above the 2.8 μm absorption and the band center. These maps show a definite local depletion of OH-bearing minerals for six of the external PIDs with respect to their immediate surrounding, indicating the loss of hydroxyl groups upon PID formation. We note that many PIDs show ambiguous OH depletions, likely due to the limited resolution of the VIR instrument (~ 200 m/px).

644　The lowest OH abundances of the Marcia area are observed within the Marcia crater and even for the

645　PIDs within the crater-fill material, which generally exhibit a lower average reflectance and pyroxene

646　band strength values as seen in Figs. 2, 10, 11j and Table 3. The lower than average reflectance was

647　previously described in Denevi et al. (2012) and De Sanctis et al. (2015c). This is a contrary observation

648　to all other PIDs, where lower 2.8 μm band depth values are linked to higher reflectance and stronger

649　pyroxene absorptions (i.e., bright = OH-depleted). External PIDs with similar reflectance and pyroxene

650　band strength values as the crater-fill PIDs (e.g., Fig. 11h) show higher 2.8 μm band depth values as

651　well as darker and more featureless immediate surroundings than the PIDs within the crater-fill material.

652　We therefore emphasize here that the crater-fill PIDs are different to all other PIDs.

a

-7807 m ■■■■■■■■■■ -6540 m

0.0273 ■■■■■■■■■■ 0.0359

b

-8576 m ■■■■■■■■■■ -7438 m

0.0254 ■■■■■■■■■■ 0.0346

c

-8440 m ■■■■■■■■■■ -7991 m

0.0277 ■■■■■■■■■■ 0.0373

d

-6998 m ■■■■■■■■■■ -6301 m

0.0278 ■■■■■■■■■■ 0.0372

e

-8718 m ■■■■■■■■■■ -7925 m

0.0258 ■■■■■■■■■■ 0.0432

653

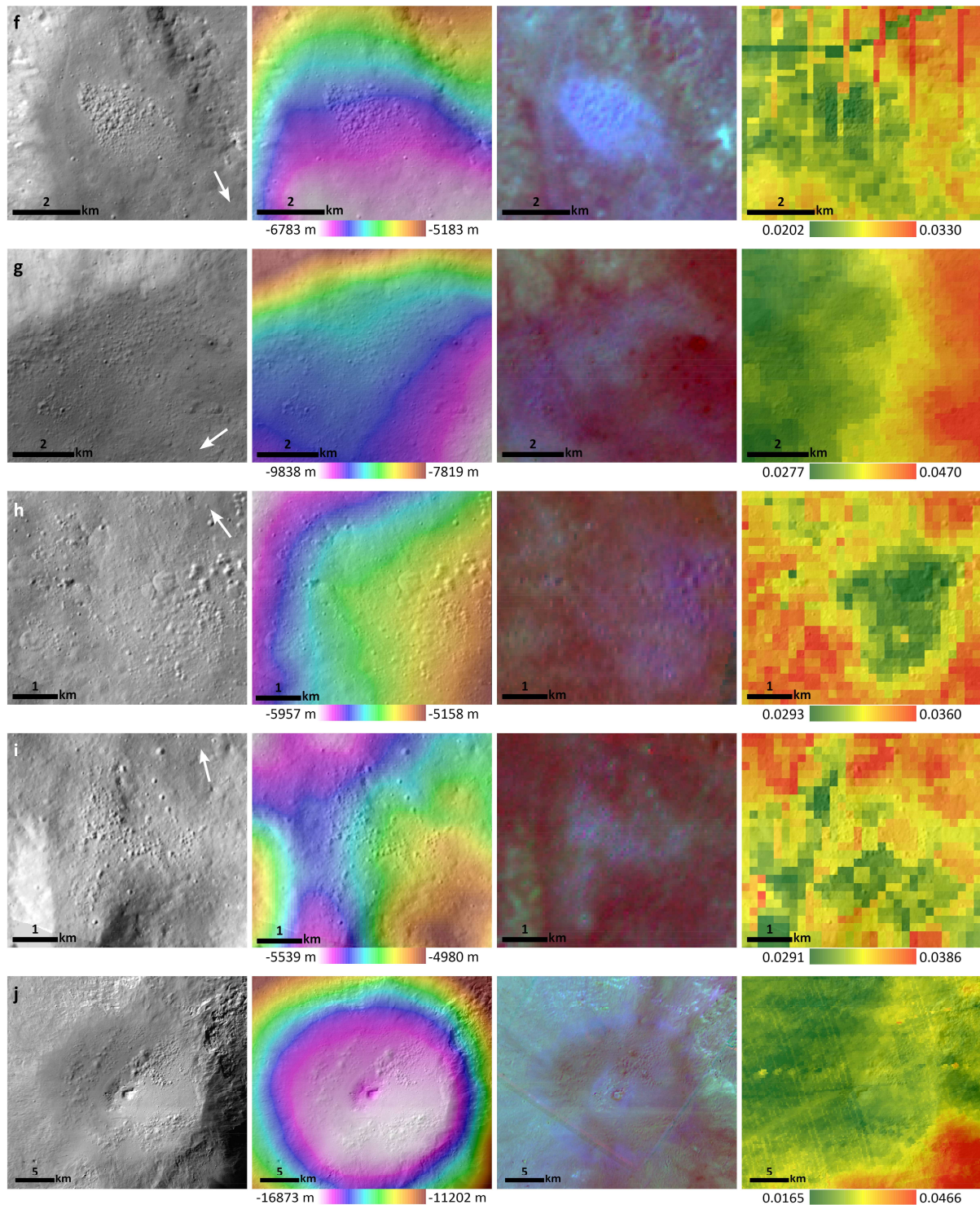654   Fig. 11: see description on the next page

26

Fig. 11 cont.: Ten examples of PIDs in and around Marcia showing eucrite-like spectral features and in six cases definite local depletions of hydroxyl groups (i.e., decrease of absorption at 2.8 μm). The first panel in each row shows clear filter LAMO data and white arrows indicate the direction to the primary cavity of Marcia. 2nd panel: DTM data (50% transparency over LAMO clear filter data). 3rd panel: HAMO RGB composite (R= 965/917 [nm], G=750 nm and B=750/917 [nm], same stretch in every row), greenish/cyan colors represent higher reflectance and pyroxene band strength. 4th panel: 2.8 μm band depth distribution map from Combe et al. (2015). Row j shows the central PIDs of the Marcia crater floor. Spatial context is displayed in Fig. 6.

664 However, the PIDs within the crater-fill material are not exclusively 'darker' and appear to have a

665 spectral 'halo' where they meet and embay the crater wall (Fig. 12a, dashed outline and arrows).

666 Especially at the northern and western margins of the crater-fill material areas with higher reflectance

667 and pyroxene band strength are visible (Fig. 12b and Table 3), consistent with those of external PIDs.

668 These areas comprise significantly smaller pits than the rest of the PID (Fig. 12b), and appear smooth

669 where the halo does not show a pitted surface. The northern halo material generally resides on larger

670 slopes (~ 5° to 15°) than the rest of the crater-fill PIDs towards the central peak (~ 1° to 6°). The

671 southwestern halo (Fig. 12a, arrows) is located at lower elevations and generally smaller slopes than the

672 northern halo (Fig. 12a, dashed line) and appears smooth with minor pitting. Small pits down to the

673 resolution limit can be observed in the close-up image in Figure 12b. The crater-fill PIDs are therefore

674 not homogenous in terms of their spectral characteristics which makes them unique among the 118

675 mapped PIDs in and around Marcia. An important observation is moreover that in some parts the

676 described halo is superposed by material input from the crater wall which is best illustrated on the right

677 side of Figure 12b. This is also valid for the spectral characteristics as the superposing slumps show

678 lower reflectance and pyroxene band strength (compare with Fig. 12a).

679 Moreover, an area with the same spectral characteristics as the 'halo' is found around the central peak

680 (Fig. 12c). The higher reflectance and pyroxene band strength is strongly correlated with a confined area

681 of pitted and smooth terrain showing signs of subsidence along a small topographical scarp (arrows in

682 Fig. 12c). Signs of subsidence were already reported for other regions within the crater-fill deposit

683 (Denevi et al., 2012), but these do not show this distinct spectral signature. In the northwestern part, it

684 cannot be determined if the topographic feature is a scarp or a ridge and the DTM does not resolve this

685 topographical difference. The highest reflectance and pyroxene band strength values in this central peak

686 halo are observed for a smooth appearing area WNW of the central peak and for a pitted area ESE of
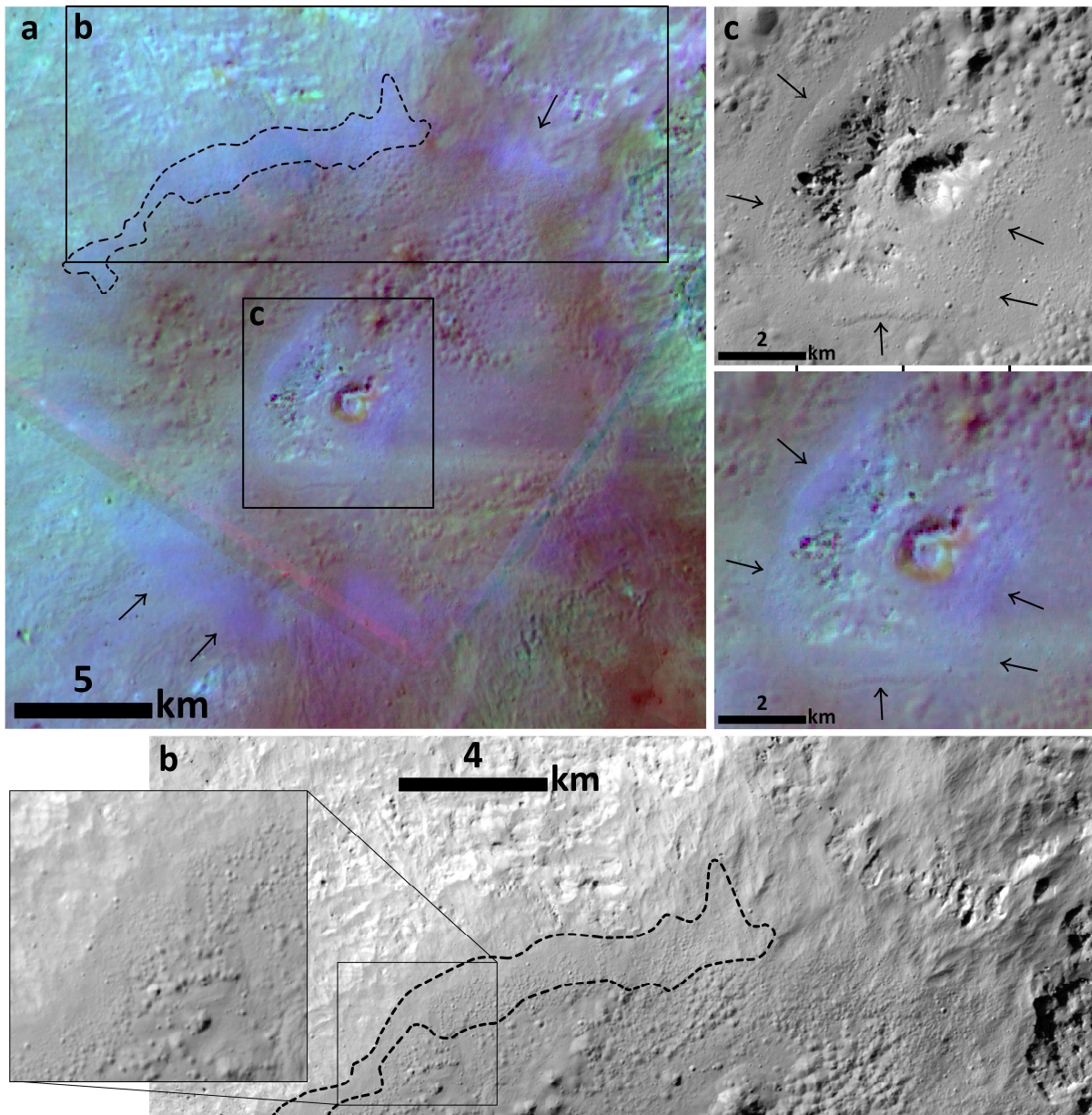
687 the central peak.

Fig. 12: a) HAMO RGB composite of the Marcia crater-fill PIDs. The spectral halo of the crater-fill PIDs at the margin towards the crater wall appears cyan/bluish. One part of the halo is indicated by dashed lines, others are indicated by arrows. b) LAMO clear filter image, area of the spectral halo appears to contain both pitted and smooth material while the pits are close to the resolution limit. c) displays the area around the central peak showing signs of subsidence as well as distinct PIDs comprising very small pits (upper panel) and higher reflectance and pyroxene band strength (cyan/bluish in lower panel). Spatial context is given in Fig. 6.

Table 3 displays the mean reflectance at 750 nm, 750/917 [nm] and 2.8 µm band depth values of Marcia-related regions of interest relevant for this study. Values for 'PIDs' (1st row) include the nine PIDs in Figure 11 a-i and values of their 'surroundings' (2nd row) include only the surroundings of these nine PIDs. The 3rd row denotes the PIDs surrounding the central peak of Marcia crater, excluding the ones on the southern terrace. 'Halo floor' denotes the outlined area in Fig. 12a.

701 Table 3 and Figure 11 demonstrate that the PIDs significantly differ from their immediate surroundings,
702 especially considering the 750/917 [nm] values. In comparison with the PIDs on the crater floor and the
703 whole Vesta, PIDs have a similar mean in reflectance at 750 nm but a higher mean in the 750/917 [nm]
704 values, as does the halo. A more intuitive Figure is displayed in section 3.5. PIDs have similar mean
705 reflectance values like the average Vesta as they comprise both brighter and darker PIDs which will also
706 be shown in section 3.5. Additionally, 2.8 μm band depth values show that the PIDs and their
707 surroundings (i.e., ejecta material) are both enriched in OH with respect to materials within the crater
708 (PIDs, halo and NW crater wall).

709 **Table 3**
710 750 nm reflectance, 750/917 [nm] and 2.8 μm band depth values (from Combe et al., 2015) of locations of interest. Values are
711 given with one standard deviation.

	Mean 750 nm reflectance	Mean (750/917 [nm])	Mean 2.8 μm band depth	n (pixel number)
PIDs (Fig. 7a-i)	0.190 ± 0.017	1.529 ± 0.100	0.031 ± 0.004	3,707
Surroundings	0.167 ± 0.012	1.379 ± 0.048	0.034 ± 0.004	22,982
PIDs (floor, Fig. 7j)	0.183 ± 0.007	1.443 ± 0.029	0.023 ± 0.002	26,089
Halo floor	0.201 ± 0.004	1.579 ± 0.026	0.020 ± 0.002	4,509
NW crater wall	0.217 ± 0.008	1.576 ± 0.031	0.021 ± 0.001	64,213
Whole Vesta	0.192 ± 0.035	1.454 ± 0.145	0.030 ± 0.009	$3.56 * 10^8$

712

713 The distinct spectral characteristics of the PIDs are not exclusively confined to the pits themselves.
714 Instead, the spectral signatures reach several tens of meters outward building another sort of halo around
715 the PIDs (see especially Fig. 11b, e & f). Thus, some parts of the smooth surface of the host deposit
716 show the same spectral characteristics as the pitted parts. However, due to the resolution limit, it cannot
717 be excluded that there are smaller pits inside these halos (< 50 m). We note that for other (potential)
718 PIDs identified on Vesta by Denevi et al. (2012) we did not observe such apparent spectral variations
719 (i.e., in craters Cornelia, Licinia and Numisia).

720

721 3.4   Spectral comparison with HEDs

722 Figure 13 displays FC data ratios of the most prominent PIDs (i.e., 11a, b, c and f which exhibit the
723 highest 750/917 [nm] values, magenta colored data cloud) in comparison with other locations of interest
724 on Vesta and the meteorite spectra from RELAB (Figure 1, now black & grey symbols), showing that
725 the data points of these PIDs overlap with the main data cloud of eucrites (light grey circles). The NW
726 crater wall of Marcia shows very similar values like the PIDs, but with slightly lower 750/917 [nm]
727 values. The surroundings of the PIDs (light turquoise), as well as the PIDs on the Marcia crater floor
728 (purple) have relatively equal values and also overlap with eucrite data points but with lower
729 750/917 [nm] values with respect to the selected PIDs. E2a (light blue) and Aricia Tholus (dark blue)
730 have even lower 750/917 [nm] values. All of these regions of interest together plot on a mixing line
731 between eucrite and carbonaceous chondrite data (indicated by shortly-dashed line). They show a slight
732 difference in 965/917 [nm] values. This observation is consistent with previous studies suggesting
733 carbonaceous chondrites as the source for the observed dark material on Vesta.
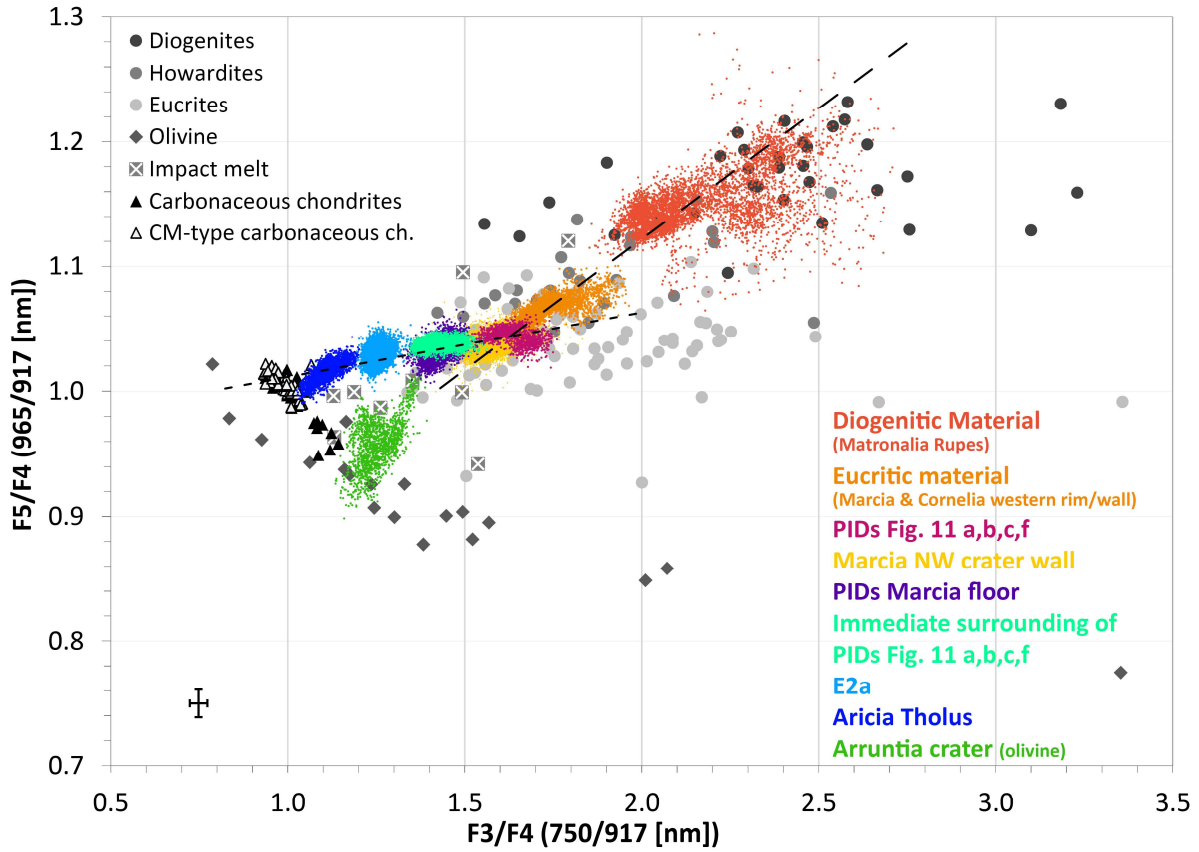
Fig. 13: 750/917 [nm] vs. 965/917 [nm] of various locations of interest (colored data) with RELAB meteorite data from Fig. 1 in black, white, and grey colors. The FC ratio values of selected external PIDs overlap with data points of eucrites as well as partly with data for the most eucritic regions on Vesta (orange data points, taken from Marcia western rim and Cornelia western wall). These PIDs can therefore be spectrally separated from their immediate surroundings (light turquoise) and from the PIDs on the Marcia floor (purple). Dashed lines represent spectral trends of contaminated material (flatter line between carbonaceous chondrites and eucrites) and uncontaminated material (long dashes, purely HED). The error indicator on the lower left displays an approximate calibration uncertainty of 3% after Schröder et al. (2014). Note that the diogenitic material (dark orange) overlaps well with the diogenite data points (black circles), indicating an accurate calibration and the feasibility of this comparison.

On this 'contamination mixing line', PIDs appear to represent the eucrite-rich endmember. Eucritic regions of interest with even 'purer' (i.e., less contaminated) eucritic compositions (orange) likely representing exposed eucritic bedrock, such as at the rim of Marcia crater (Fig. 10, upper middle panel) and the bright slope deposit on Cornelia's western wall (Fig. 10, upper right panel), show even higher 750/917 [nm] and significantly higher 965/917 [nm] values.

Matronalia Rupes – a scarp at the Rheasilvia Basin rim – was previously reported to be composed of diogenitic rock (e.g., McSween et al., 2013a; Ammannito et al., 2013a; Stephan et al., 2015), which is consistent with our comparison in Figure 13 (dark orange). Carbonaceous chondrites have values around 1.0 for 965/917 [nm] and 750/917 [nm], while Vestan data generally have higher values for both ratios (Fig. S4). This suggests that larger values for 965/917 [nm] and 750/917 [nm] indicate less contamination with carbonaceous chondrite material (or other reflectance-lowering components).

Moreover, seemingly "pure" regions (eucritic and diogenitic characteristics) are characterized by another dependency than contaminated areas and plot on a different trend line (dashed lines in Fig. 13).

The cause for these two distinct trend lines is 1) the contamination by dark (carbonaceous chondrite) material and 2) that the Marcia region is characterized by a high eucritic abundances with no diogenitic occurrences (Ammannito et al., 2013a; Prettyman et al., 2013). Therefore, the slope of the "contaminated trend line" in Figure 13 is significantly lower than the HED trendline including diogenites. For the Marcia region, we only observe a very subtle change in the pyroxene band position (indicated by the 965/917 [nm] ratio), which can be attributed to the described contamination.

The mineral olivine, which commonly occurs in planetary materials, does not contribute to the spectral characteristics of the PIDs either. Firstly, it has not been detected in the Marcia area (Ammannito et al., 2013b; Thangjam et al., 2014; Palomba et al., 2015), and secondly, olivine exhibits lower values in both considered ratios (see Fig. 1 and 13), which is contrary to our observations of the PIDs. However, detection of olivine by the Dawn instruments is challenging and might not be possible below 30 vol% (Beck et al., 2013; Le Corre et al., 2013), adding uncertainties in these interpretations.

HED data plot on a trend line when the pyroxene band I center is plotted against the pyroxene band II center (e.g., De Sanctis et al., 2012a and 2015c). Most of the Vestan surface is slightly deviating from this trend, which can again be explained by the contamination of impacting carbonaceous chondritic material. The same is observed when plotting FC color ratios against each other (Thangjam et al., 2013 and this study, long dashes in Figs. 13 & S4), which only cover the first pyroxene absorption band. The vast majority of Vestan FC data plot near eucrites/howardites but with a small bulge toward carbonaceous chondrites. This is displayed in the supplementary Figure S4. The highest density of the Vestan surface plots around 1.44, 1.05 (ratio values), whereas some of the PIDs plot around 1.65 (and more) and 1.04, which furthermore suggests that the main parameter to distinguish the different terrains is the indicator for pyroxene band strength, 750/917 [nm].

In summary, the major parameter for the distinction between the PIDs and their surrounding is the FC ratio 750/917 [nm] (F3/F4). The data points of selected PIDs outside of Marcia overlap with data points of eucrites, consistent with previous findings that the Marcia region is enriched in eucritic rock types (e.g., Prettyman et al., 2012; De Sanctis et al., 2015b). The spectral comparison with HED meteorites shows that PID-related regions of interest (PIDs, PID surroundings and E2a) are consistent with contamination by carbonaceous chondrites. Changes in pyroxene mineralogy towards diogenitic lithologies is not observed.

3.5 Comprehensive analysis of observations

Linking all our observations, we can separate the PIDs external to Marcia (101 PIDs) into two different types according to the ejecta units defined in section 3.1. PIDs of type 1 comprise PIDs located in E1,

where the ejecta blanket generally exhibits higher reflectance and stronger pyroxene absorptions (as does the NW part of Marcia, see Fig. 2b). These PIDs exhibit higher mean reflectance at 750 nm (Table 4), a higher mean value for the 750/917 [nm] ratio and slightly lower 2.8 μm absorption depths compared with average Vestan values. Furthermore, they have larger spatial extents (mean of 2.2 km^2) than type 2 PIDs (mean of 1.8 km^2). In total, 41 out of 101 external PIDs are of type 1 and ten of them occur within craters that existed prior to the Marcia impact (i.e., ~ 24 % of PIDs in E1 are located in small pre-existing craters).

Type 2 PIDs exhibit lower than average mean reflectance at 750 nm (Table 4) and their 750/917 [nm] ratios resemble the value of the average Vesta. Their 2.8 μm absorption depths are above the average of Vesta. Seven of the 17 identified PIDs in pre-existing craters are of type 2 (i.e., ~ 12 % from type 2 PIDs are located in small pre-existing craters), yet all of these seven occurrences are located within E2b, which corresponds to ~ 18 % of this ejecta unit's PIDs (39 PIDs within E2b and 21 within E2a). Type 2 PIDs are more abundant and are located within E2a and E2b. Considering PIDs/km^2, PIDs are more abundant in E1. This indicates that E1 contained more volatiles than E2a and E2b (all have roughly the same spatial extent), which is contrary to the general higher reflectance and pyroxene band strength nature of E1. However, if E2a (and possibly E2b) were to originate from Calpurnia, the Marcia impactor would have hit a relatively young ejecta blanket (i.e., Calpurnia ejecta shows a similar age as Marcia ejecta, Williams et al., 2014b; Appendix A) and overprinted possibly already existing PIDs sourced from Calpurnia. The impact event forming Marcia could have incorporated volatiles from the well-preserved Calpurnia ejecta. Furthermore, as ejecta deposits are more abundant close to the parent crater, E1 might comprise more PIDs/km^2 as it represents the closest ejecta deposits to Marcia.

Table 4
750 nm reflectance, 750/917 [nm] and 2.8 μm band depth values (from Combe et al., 2015) of the two PID types. Values are given with one standard deviation.

	Mean 750 nm reflectance	Mean (750/917 [nm])	Mean 2.8 μm band depth	n (pixel number)
PIDs type 1 (Fig. 11 a-f)	0.206 ± 0.008	1.621 ± 0.060	0.028 ± 0.003	1,667
Surroundings type 1 (Fig. 11 a-f)	0.172 ± 0.010	1.402 ± 0.042	0.033 ± 0.004	14,784
PIDs type 2 (Fig. 11 g-i)	0.174 ± 0.005	1.431 ± 0.020	0.033 ± 0.002	2,040
Surroundings type 2 (Fig. 11 g-i)	0.158 ± 0.009	1.336 ± 0.020	0.037 ± 0.004	8,198

Figure 14 is a key figure in this study and summarizes the values given in Tables 3 and 4, showing that PIDs show a deviating trend regarding both reflectance at 750 nm and OH content (i.e., 2.8 μm band depth) with respect to 750/917 [nm] values. The surroundings of PIDs, the NW crater wall, the crater next to the SW PID (shown in Fig. 10) and the average Vesta roughly plot on a common trend line (dashed) in both displayed diagrams, indicating a 'typical' dependence of reflectance (and OH content) and pyroxene band strength for Marcia-related regions of interest and the average Vestan values. PIDs clearly deviate from this trend (dotted line). PIDs generally have higher 750/917 [nm] values with respect to 750 nm reflectance and 2.8 μm band depth values of other more typical Marcia-related

materials. This furthermore illustrates that the PIDs' materials have undergone a process changing the original spectral nature of Vestan material.
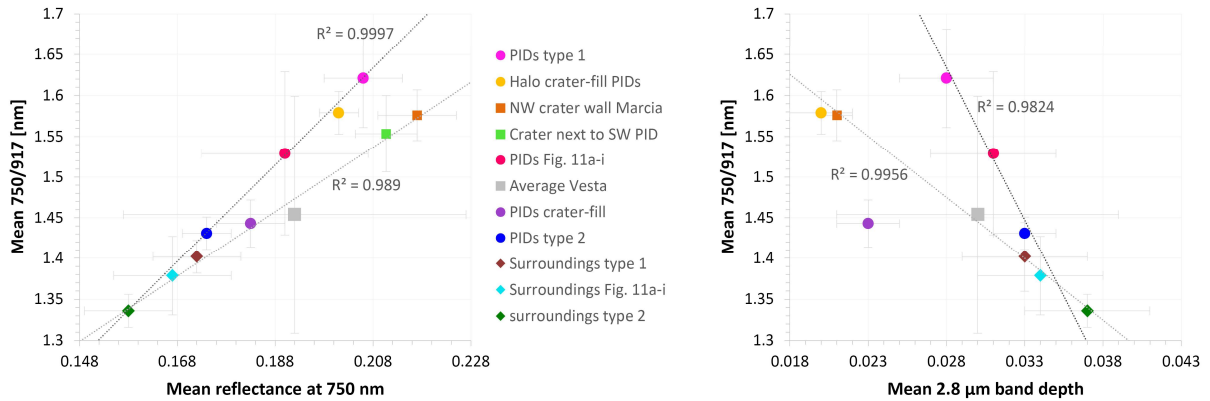

Fig. 14: Left panel: Mean reflectance at 750 nm vs. Mean 750/917 [nm] of regions of interest reported in Tables 3 & 4 and a small crater next to a PID (Figure 10, left panel). Right panel: Mean 2.8 μm band depth vs. mean 750/917 [nm] reported in Tables 3 & 4. Error bars indicate the given standard deviations, for the 'crater next to SW PID', an error of 3 % is displayed, as described for Fig. 10. There is no 2.8 μm band depth available for this crater due to the limited resolution of the VIR instrument. Regression line for PIDs contains the three PID data points. Regression line for the Marcia-related regions of interest contains the NW crater wall, the crater next to the SW PID (only for the left panel, Figure 10), the average Vesta and the three surroundings of PIDs.

We note that while the crater-fill PIDs show similar reflectance and pyroxene band strength values as for example the average Vesta, their OH contents are significantly lower, putting them in their own category (purple circle in Figure 14, right panel). As described before, the crater-fill PIDs are not nearly as spectrally homogeneous like all other PIDs (see section 3.3 and Figs. 11 & 12). Instead, these PIDs show spectral and geomorphological variations (see 'halo' and 'crater-fill' PIDs in Figs. 14 and 12) and furthermore are the only PIDs that exhibit lower reflectance and pyroxene band strength values than their immediate surroundings (Fig. 2, 11j and 12) while also showing the lowest OH abundance of all PIDs. The crater-fill PIDs and their individual pits moreover are significantly larger than all other PIDs (see section 3.2 and Fig. 5). The crater-fill halo (orange circle in Fig. 14) likewise represents its own category linked to the crater-fill PIDs, yet comprise very small individual pits down to the resolution limit (Fig. 12b) and also smooth material. In the left panel of Figure 14, the halo plots roughly on the same trend line as the external PIDs (dotted). If we would plot a regression line for the data points of the halo and the crater-fill PID, it would show an even steeper slope in the left panel and a line roughly parallel to the PID regression line in the right panel, indicating similar characteristics.

The presence of two types of PIDs is closely linked to the ejecta units described in section 3.1. Therefore, we again acknowledge that PIDs of type 2 might originate from the impact that formed Calpurnia crater. It remains challenging to explain the occurrence, extent and spectral characteristics of E2b if Calpurnia is the source. Again, the determination of the PID parent crater is not crucial for this study. The most important observations and interpretations are not tied to this separation. Moreover, if the ejecta units

853 did not form from a single event, it shows that the unique spectral changes the material underwent upon
854 PID formation is not a singularity, but instead can form during other impact events too. Yet we note that
855 Calpurnia and Marcia are adjacent to each other and likely sampled the same target material.
856 Unfortunately, there are no other large and well-preserved craters on Vesta's surface in order to see
857 whether impact events in other areas of Vesta could likewise have generated spectrally distinct PIDs.

858 Lastly, we emphasize the unique spectral trend for PIDs by presenting the left panel of Figure 14 with
859 additional data from known diogenitic sites (i.e., Matronalia Rupes scarp and craters Aelia, Lollia and
860 Antonia) which is displayed in Figure S5. These diogenitic sites plot parallel to the 'Marcia-related'
861 regression line, strengthening the unique trend for PIDs.

862

863 4   Implications on the formation of the Marcia-related PIDs

864 *4.1 Origin of the PIDs*

865 On Mars, Ceres and Vesta, PIDs occur within smooth impact deposits (Tornabene et al., 2012; Sizemore
866 et al., 2017; Pasckert et al., 2018; Denevi et al., 2012), implying that smooth and pitted surfaces share
867 the same host deposit and originate from the same event. Our analysis adds more occurrences of PIDs
868 to the already existing data on Vesta (Denevi et al., 2012) and further confirms the relationship of the
869 pitted and smooth ejecta deposits. The spectral characteristics of these two deposit surface types are
870 different from each other, yet their analysis also confirms a relationship of the two: PIDs show higher
871 reflectance and pyroxene band strength with respect to the smooth deposit surroundings and the absolute
872 values of PID reflectance and pyroxene band strength are directly related to those of their surroundings;
873 i.e., where the surrounding host material has less pronounced pyroxene characteristics and lower
874 reflectance (ejecta unit E2), the PIDs' material likewise exhibits a less pronounced 'enhancement' of
875 these properties (PIDs type 2) and vice versa. This confirms a simultaneous emplacement of the original
876 material before pits formed on some of the deposits surface, as was shown in detail by Tornabene et al.
877 (2012) for Mars. Therefore, it can be excluded that the material of the PIDs was introduced later, e.g.
878 by some sort of extraordinary secondary impact process at a later stage of Marcia's formation. As a
879 result, differences in age and exposure to the various kinds of space weathering processes (Pieters et al.,
880 2012) are very unlikely causes for the spectral differences.

881 We furthermore observe that the spectral characteristics of PIDs reach several tens of meters outward
882 into the smooth zones of the host deposits, building another sort of halo around the PIDs. This indicates
883 that the formation of the individual pits inside a PID is linked to ejection of material, not e.g. the loss of
884 material through subsurface voids, which was also shown for Mars (Tornabene et al., 2012). Thus, solid
885 material was likely ejected along with volatile phases. This is consistent with the interpretation of Denevi
886 et al. (2012).

887   We observe several PIDs occurring in pre-existing craters and with positive local topographies, facing
888   Marcia crater. Their origin therefore appears to be linked to the accumulation of ejecta (Fig. 15).
889   Accumulation of material is accompanied by an increase of impact deposit thickness and an increase in
890   the amount of internal heat. The volume of heat-bearing material increases significantly whereas the
891   surface area – where heat can freely radiate into space – remains small. This possibly results in the
892   liberation of hydroxyl groups from their host minerals as well as the buildup of pressure within the pore
893   spaces. The crater-fill PIDs do not feature a positive topography, yet they naturally represent
894   accumulated, possibly partially melted impact material within a large cavity, likewise leading to an
895   increased volume of volatiles per surface area and an increased internal amount of heat.

896   Furthermore, we identified several locations where PIDs reside along scarps and crater walls (Fig. 15b),
897   likewise indicating a structural control facilitating the liberation of volatiles along contacts between the
898   host deposits and bedrock. Although a relationship to pre-existing topography is only observed for a
899   minor population of the PIDs, it is reasonable to assume that this mechanism also plays a role for other
900   PIDs where pre-existing topography cannot be determined anymore, especially within E2b and E2a,
901   where the pre-existing topography has been largely obscured by overlying ejecta. In summary, we
902   present evidence that the formation of PIDs is controlled by the geomorphological setting into which
903   the impact deposit was placed. This is consistent with what Denevi et al. (2012) already suggested (i.e.,
904   'topographic lows') and what Tornabene et al. (2012) found for Martian PIDs.

905   Stubbs and Wang (2012) suggested the long-term survivability of water ice a few meters below the
906   surface of Vesta and therefore Scully et al. (2015) suggested that the heating of heterogeneously
907   distributed subsurface ice deposits could also have caused the formation of PIDs. However, it is unlikely
908   that subsurface ice would coincidentally be present within pre-existing craters, facing the excavation
909   direction of a non-existent crater at that point in time. The redistribution of icy material by the impact
910   and preferred deposition within craters is also questionable. Considering the spectral characteristics this
911   possibility likewise seems implausible as the sublimation of water ice would not result in a spectral
912   change of the rocky material considering a rapid degassing within hours. In conclusion, our observations
913   do not favor a role of (water) ice in the formation process which instead is controlled by accumulation
914   of ejecta and therefore the possibility of the material to liberate volatile species (i.e., increased amount
915   of internal heat) and to build up the necessary pressure and vent pipes.
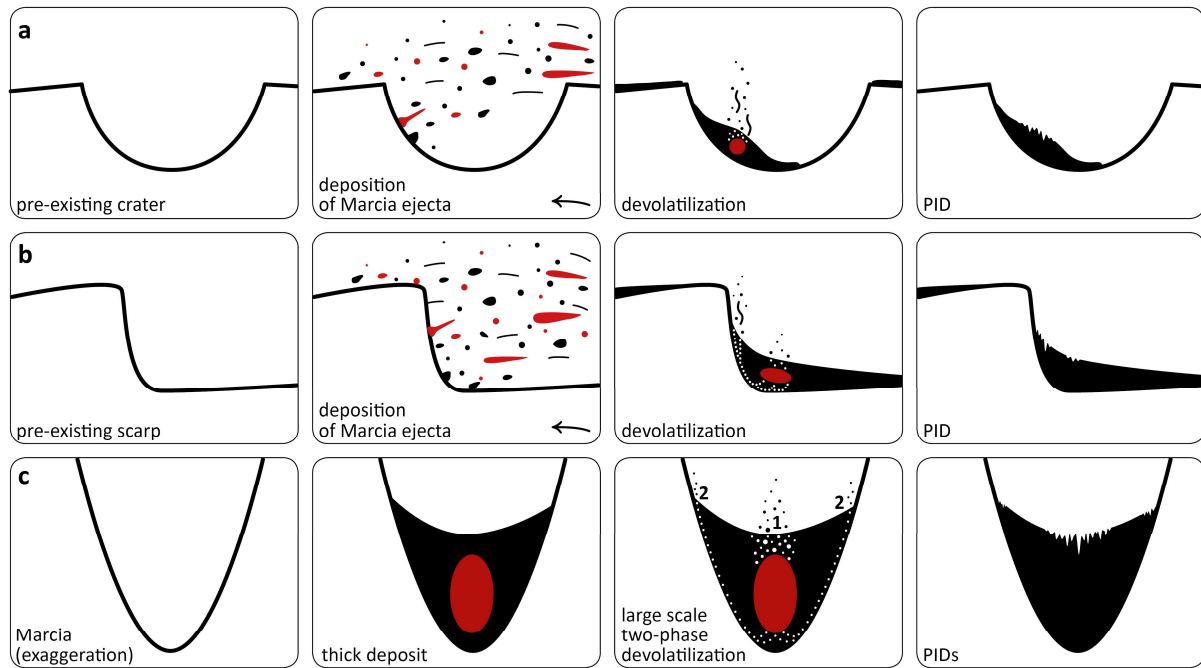
Fig. 15: Simplified schematic depiction of the mechanism leading to the formation of PIDs according to profiles shown in Figure 9: a) within pre-existing small craters, b) at topographic highs, c) within Marcia (deposit thickness > 500 m). White circles indicate paths for volatile escape. Red color within a deposit indicates the thickest part which likely retains heat for the longest time spans (highly simplified).

Our analysis of topographic profiles indicates that PIDs both form where their host deposit is thickest, but also on the margins of a host deposit. In the former case, this indicates an internal volatile source as such that the volatiles directly originate from the impact ejecta, which is likely a melt-bearing breccia (Tornabene et al., 2012; Denevi et al., 2012). In the latter case (formation on the margins of a deposit), pit formation occurs close to the colder target rock, which could indicate a contribution of target rock volatiles. However, an easier explanation consistent with observations by Tornabene et al. (2012) is that the contact provides a zone of weakness or conduit that would provide a path for volatile release and thus concentrate pits along those margins (Fig. 15b and c, white circles). PID formation on margins of a host deposit is especially present within Calpurnia, Minucia and also Marcia, where host deposit thicknesses are considerably larger than in other areas. The heavier overburden could additionally lead to the preferred release of volatiles along pathways adjacent to the colder target rock. Within Marcia, it is astonishing to observe very large PIDs in the center of the host deposit and very small PIDs located on the margins within the spectrally distinct halo. This might suggest more than one phase of devolatilization where the largest number of volatiles is released very rapidly through the direct pathways within the deposit and residual volatiles from deeper regions within the host deposit ascend along the margins to form smaller PIDs (Fig. 15c). The presence of the spectral halo itself as well as signs of subsidence within the crater-fill deposit (Fig. 12 in this study and Denevi et al., 2012) might support this hypothesis of different devolatilization phases.

940   The majority of PIDs (~ 73 %) occur within 30 km (i.e., one crater radius) of the Marcia rim. This

941   correlates well with the positive correlation of ejecta deposit thickness and PID occurrence as ejecta

942   thicknesses gradually become lower with distance from the crater (e.g., Melosh, 1989).We observe the

943   largest and thickest PIDs within the parent crater (Marcia) and a decrease of pit occurrences (i.e.,

944   dependent on deposit thickness) with distance from the parent crater. However, we did not observe a

945   correlation of deposit thickness and PID size (area) within the 13 identified pre-existing small craters

946   that host PIDs. This could be due to an erroneous estimation of pre-Marcia topography but also to

947   compositional inhomogeneities within the ejecta (especially in terms of volatile content). Tornabene et

948   al. (2012) present evidence for Tooting crater on Mars that shows that volatile contents of the target

949   rock might vary in different portions of the crater, resulting in pit-poor and densely pitted regions within

950   this crater. Given the possibility that Marcia crater was formed by an oblique impact (oval shape),

951   heterogeneities within the ejecta deposits appear likely and could cause various pit size:deposit thickness

952   ratios not dependent on each other.

953

954   *4.2 Origin of the PIDs' spectral distinctness*

955   PIDs are characterized by an increase in reflectance as well as pyroxene band strength with respect to

956   their immediate smooth surroundings (excluding the crater-fill PIDs), yet to a varying degree (Fig. 11).

957   This spectral change occurred after deposition and could result from changes in grain size, structure or

958   composition.

959   Regarding grain size, higher reflectance of a pyroxene-bearing material can be attributed to a smaller

960   grain size (e.g., Clark, 1999) as the larger number of reflective surfaces (crystal faces) increases the

961   probability of light scattering. In contrast, stronger pyroxene absorptions can be attributed to larger grain

962   sizes as absorption of light is more likely with lower numbers of reflective surfaces and larger crystal

963   bodies. Harloff and Arnold (2001) have shown that differences in roughness behave similar to

964   differences in grain size. Therefore, the spectral characteristics of PIDs do not conform to general grain

965   size or roughness effects. We nevertheless evaluate the effect of grain size variations specifically for

966   HED meteorites in order to evaluate whether grain size might still have an influence on the spectral

967   appearance of the PIDs.

968   Figure 16 shows the same spectral parameters as Figures 1 & 13 but for 16 individual HED meteorites

969   which were ground and separated into different grain size fractions. For 14 of these HEDs the largest

970   grain size fraction exhibits the lowest 965/917 [nm] values which probably results – in contrast to a

971   compositional difference due to different band centers –from the decrease of pyroxene band depth with

972   larger grain sizes (e.g., Clark, 1999; Cloutis et al., 2013a). Absorption band saturation for the first

973   pyroxene band of HEDs commonly starts around grain sizes of 67 μm on average (Cloutis et al., 2013a).

974   The spectra of grain sizes beyond that average value show more similar reflectance for 965 and 917 nm

975 which reduces 965/917 [nm] values. Vice versa, the smaller grain sizes show the highest 965/917 [nm]

976 values.

977 Except for JAH626, the finest fractions of all HED's exhibit the lowest 750/917 [nm] values, yet the

978 largest grain size fractions exhibit the second lowest values for 12 of these meteorites. A possible reason

979 for this is also the saturation of the absorption band. As grain sizes get larger, pyroxene band depth and

980 reflectance become lower. Once a maximum of band depth is reached, reflectance can continue to

981 decrease while the band depth cannot, causing 750/917 [nm] values to decrease again (e.g., Clark, 1999;

982 Harloff & Arnold, 2001). PRA04401 contains carbonaceous chondrite clasts but does not exhibit any

983 distinct spectral properties in terms of grain size. In summary, the presented spectra of different grain

984 size fractions of HED meteorites are consistent with general grain size-related observations which do

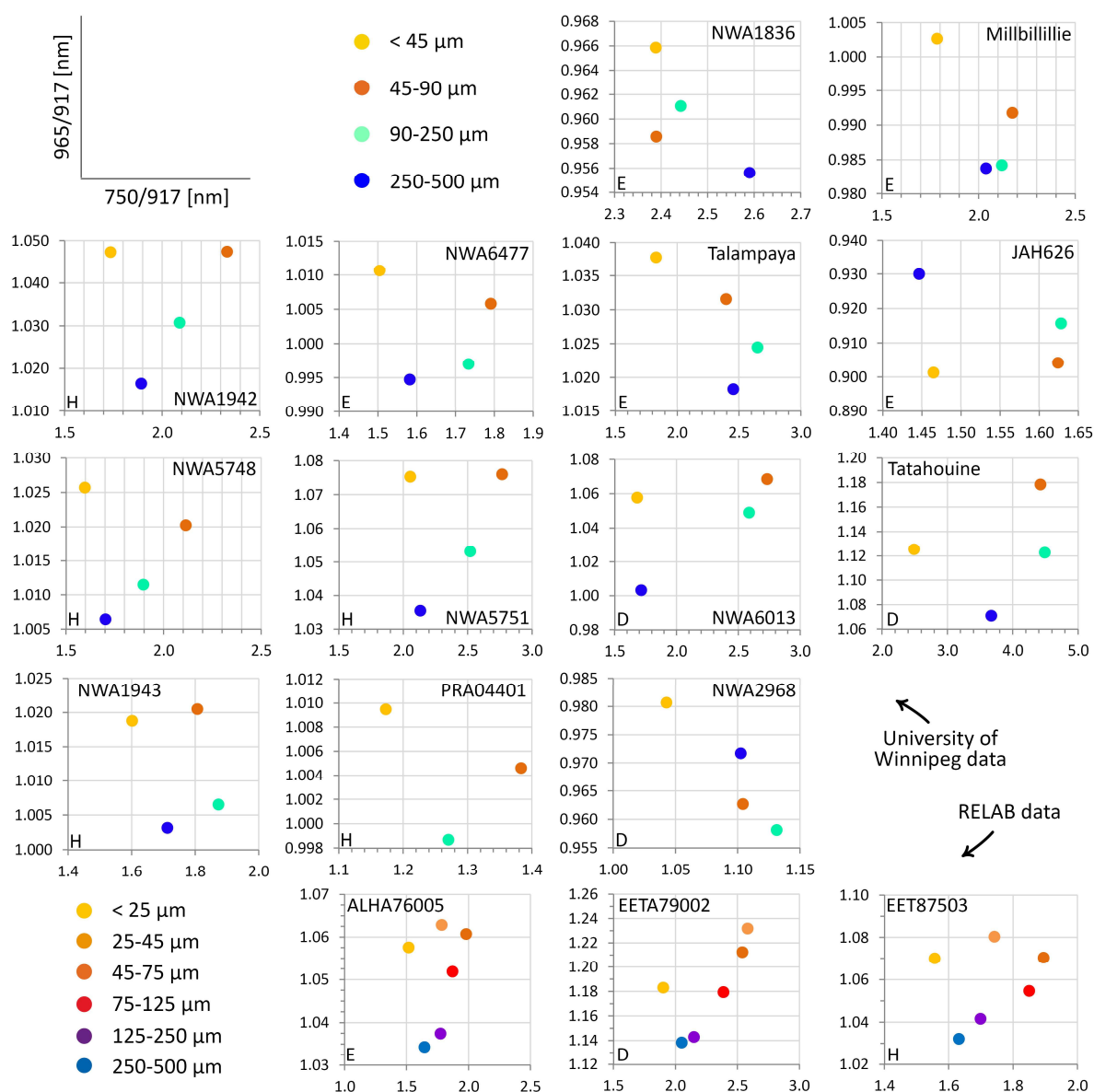985 not conform with those of the PIDs on Vesta.

986

987 Fig. 16: 750/917 [nm] vs. 965/917 [nm] for 16 different HED's that have been separated in several grain size fractions. Note

988 that for PRA04401, only three size fractions were available and that for the three RELAB HED's, six grain size fractions were

989 available. The small letters in the lower left corners indicate the HED species. The first 13 sample spectra were provided by
990 Dr. Edward Cloutis and measured at the University of Winnipeg's Planetary Spectrophotometer Facility (e.g., Cloutis et al.,
991 2013a and 2013b).

992

993 As we have just described, he difference of the PIDs associated with Marcia with respect to their
994 surroundings is very systematic (higher 750/917 [nm] values, almost no change for 965/917 [nm]),
995 indicating no observable consistency of spectral characteristics related to particle size or roughness.
996 Zambon et al. (2014) also found that the bright material on Vesta does not result from differences in
997 grain size. In their spectral study on HED meteorites mixed with CM2-type chondrites, Cloutis et al.
998 (2013a) also found that contamination with carbonaceous chondrite material is the most plausible
999 explanation for the 'dark material' on Vesta and the diminishment of spectral features. Other studies
1000 also investigated the 'dark material' on Vesta (McCord et al., 2012; Reddy et al., 2012a). They likewise
1001 concluded that the occurrence of 'dark material' is most likely caused by contamination with
1002 carbonaceous chondrite material and did not find consistencies with other possible explanations like
1003 shock effects, opaque phases and plagioclase content.

1004 The differences between the PIDs and their surroundings follow the same systematics like the difference
1005 between HED properties and 'dark material': a positive correlation between reflectance and pyroxene
1006 band strength. In our case, this is furthermore supported by the slight depletion in OH that we observe
1007 for the PIDs (Fig. 11) consistent with devolatilization of exogenic, OH-bearing minerals. Therefore, we
1008 find the differences between PIDs and their surroundings with respect to reflectance and pyroxene band
1009 strength to likely result from a small difference in composition, i.e. due to the loss and/or decomposition
1010 of dark, volatile-bearing phases.

1011 Regarding our spectral analysis of HED grain size fractions, it is important to note that terrestrial
1012 weathering, especially of Antarctic meteorites, can alter the grinding behavior of meteorites and thus
1013 result in unrealistic spectra for different grain sizes with respect to material still residing on an airless
1014 body. Most of the presented Antarctic meteorites have weathering grade A or W0/W1 which are the
1015 least altered grades, thus we assume – in agreement with our observations regarding basic spectral
1016 behavior of absorption bands and reflectance with respect to grain size – that these weathering effects
1017 do not or minorly affect the visible and near infrared analysis undertaken here. JAH626 is considered
1018 an outlier in the analysis. The meteorite is highly shocked (e.g., Ruesch et al., 2015) with little signs of
1019 terrestrial weathering. NWA2968 is a find and not characterized regarding its weathering grade in the
1020 Meteoritical Bulletin so far, so it is possible that the largest grain size fraction behaves anomalous with
1021 respect to the other grain size fractions of this meteorite due to terrestrial weathering. Additionally, this
1022 meteorite is officially regarded as an ungrouped olivine-rich achondrite, so it might not be representative
1023 for Vesta.

1024   Tornabene et al. (2012) present evidence of outcropping meter to decameter-sized rock fragments within

1025   the walls of the pits with significantly "brighter" albedo which they do not observe for the smooth

1026   surroundings. They interpret this finding as evidence for the deposit being an impact melt-bearing

1027   breccia. For a suevite outcrop at Ries crater in Germany, Newsom et al. (1986) similarly report on

1028   coarse-grained surfaces of a degassing pipe system, devoid of soil/matrix. Boyce et al. (2012)

1029   additionally suggest that the high escape rates can also eject cm-sized clasts into the surrounding of the

1030   PIDs which could represent the spectral halo presented in this study. If Vestan PIDs also show

1031   outcropping rock fragments – which is not determinable with the given image resolutions – then the

1032   spectral differences could originate from this exposure. These spectral signatures might additionally

1033   differ from typical Vestan lithologies as Marcia is the largest well-preserved crater and might have

1034   excavated deeper materials not seen anywhere else beyond the Rheasilvia basin. Within Marcia's impact

1035   melt-bearing breccia, larger clasts and rock fragments would predominantly be of HED lithology due to

1036   their higher internal strength with respect to carbonaceous chondrite material and could therefore

1037   dominate the reflectance spectrum. However, if this is true, other materials in the vicinity of Marcia like

1038   small post-impact craters or 'fresh' crater wall material still subject to modification should experience

1039   similar spectral characteristics. Yet as we have presented in our study, PIDs are characterized by stronger

1040   pyroxene absorptions (750/917 [nm] values) with respect to other Marcia-related materials with similar

1041   reflectance at 750 nm. We have shown that a 'younger' crater (i.e., post-Marcia) that impacted into the

1042   smooth part of the host deposit right next to a PID shows similar reflectance values but lower pyroxene

1043   band strength. Thus, the younger crater shows less pronounced pyroxene characteristics than the older

1044   PID within the same host deposit. This strongly indicates that another process changed the typical

1045   spectral nature of the original material at the PIDs' sites which is not related to differences in pyroxene

1046   proportions.

1047   A significant shift of the pyroxene band center towards shorter wavelength and therefore to more Mg-

1048   rich pyroxene is not observed (Fig. 13), although the 965/917 [nm] ratio is sensitive to this mineralogical

1049   difference. Hence, there is no difference in the proportion of diogenitic/eucritic lithologies with respect

1050   to PIDs and their surroundings which favors the theory of carbonaceous contamination in addition to a

1051   unique process related to accumulation and heat retention. The more endogenic and OH-depleted nature

1052   of the PIDs could theoretically also arise from phase transitions of phyllosilicates to olivine and

1053   pyroxene due to shock metamorphism and heating to > 500°C and 750°C, respectively (e.g., Akai, 1992;

1054   Nakamura, 2005 and references therein). However, as Sizemore et al. (2017) similarly describe for

1055   Ceres, average impact velocities of ~ 5 km/s in the asteroid belt (Bottke et al., 1994) would generate

1056   maximum target temperatures of ~ 800 K (Marchi et al., 2013; Supplementary Fig. S3) which suggests

1057   that for average projectiles impacting on Vesta, no phase transitions of phyllosilicates would occur.

1058   Furthermore, even if Marcia was a result of a high velocity impact, no olivine has been detected in the

1059   Marcia area (Ammannito et al., 2013b; Thangjam et al., 2014; Palomba et al., 2015). Yet we again note

1060   that detection of olivine might not be possible with the given instrumentation below 30 wt% (Beck et
1061   al., 2013; Le Corre et al., 2013).

1062   Liberation of hydroxyl groups in phyllosilicates of carbonaceous chondrites starts around 400 °C
1063   (Garenne et al., 2014) implicating that the formation of PIDs can result from devolatilization of
1064   phyllosilicates at average main belt impact velocities. However, the spectral characteristics of PIDs do
1065   not conform to devolatilization studies that investigated the spectral properties of mixtures containing
1066   volatile-bearing phases upon heating and sublimation. The different mixtures (cometary analogs with
1067   silicate components) used in Poch et al. (2016) exhibited lower reflectance and diminishment of spectral
1068   features after sublimation occurred (< -70 °C). Moderate heating of a Ceres analog material (maximum
1069   of 300 K, Galiano et al., 2020) likewise resulted in darkening of spectral properties in the VIS-NIR
1070   wavelength region as does heating of phyllosilicates (up to 700 °C, e.g., Hiroi & Zolensky, 1999;
1071   Alemanno et al., 2020). The water-related band near 3 μm of the CM2 meteorite Murchison vanishes
1072   around 500-700 °C (Miyamoto, 1991; Hiroi et al., 1996) which indicates that the PIDs' materials have
1073   not seen temperatures above those values (as VIR data show absorption bands there). Below this
1074   temperature, Murchison shows a decrease in reflectance upon heating (Cloutis et al., 2012). Cloutis et
1075   al. (2012) also showed that prolonged heating (72h) of a subbituminous coal at 450 °C results in an
1076   increase of reflectance. In this example, organics are lost or aggregated which changes the phyllosilicate-
1077   organic ratio and makes the phyllosilicates spectrally more dominant. Hence, the loss of organic
1078   compounds might trigger the change in reflectance and pyroxene band strength for the PIDs' material;
1079   yet this effect has not been shown on carbonaceous chondrite material unless fully melted and
1080   recrystallized (Clark et al., 1993). There are no studies that reflect the situation on Vesta; yet the studies
1081   reported here show that most heating/sublimation experiments with different planetary analogs result in
1082   the darkening of overall reflectance and diminishment of spectral features, in contrary to what we
1083   observe for the PIDs.

1084   Differences in glass content can also affect a material's spectral characteristics. For pyroxene-rich lunar
1085   impact-melt-bearing deposits, Neish et al. (2021) found a possible contribution of glass to explain a
1086   smooth optical appearance of certain melt deposits while showing high roughness from radar
1087   observations. Given the high likelihood that the PID host material is an impact melt-bearing breccia
1088   (Tornabene et al., 2012; Denevi et al., 2012), glass content could also play a role during the formation
1089   process of PIDs (i.e., the PIDs' surface might be devoid of glass due to the destruction of the surface
1090   layer through devolatilization). Tompkins and Pieters (2010) analyzed the effects of glass content in
1091   lunar Apollo samples and observed 'redder' spectra for the quenched glass samples vs. their crystalline
1092   counterpart as well as an inconsistent dependency of the reflectance at 750 nm. They found that higher
1093   glass contents shift the mafic absorption band position near 1 μm towards longer wavelength which
1094   decreases the 750/917 [nm] ratio of a glassy-crystalline mixture. Thus, the surrounding material of the
1095   PIDs could indeed contain higher glass contents, yet there is no difference regarding pyroxene band
1096   positions for PIDs and their surroundings. The observations of Tompkins and Pieters (2010) regarding

1097 the spectral properties of glass-crystalline mixtures are not consistent with our observations of PID-
1098 related material so differences in glass content do not seem to play a role in the context of the PIDs
1099 either.

1100 We conclude that the most likely explanation for the spectral distinctness of the PIDs is the effect of
1101 prolonged internal heating due to the accumulation of material and the devolatilization accompanied by
1102 the possible loss of organics and decomposition of darkening agents, although heating studies of
1103 meteorites have only shown a general loss of spectral features and reflectance upon heating. Other
1104 processes might enhance this effect, like the ejection of entrained pyroxene-rich clasts during the rapid
1105 release of steam. Experimental work could refine this hypothesis which is beyond the scope of this
1106 study. Lastly, we note that the 'hollows' identified on Mercury (Blewett et al., 2011 and 2013) likewise
1107 exhibit an increase in reflectance and are linked to a loss of volatiles. While their origin is likely not
1108 impact-related (Blewett et al., 2013), the process of volatile release might share similar aspects as the
1109 PIDs on Vesta.

1110

1111 *4.3 The crater-fill PIDs of Marcia*

1112 The crater-fill PIDs of Marcia are slightly lower in reflectance than the average Vesta but exhibit the
1113 lowest OH abundance of all observed PIDs including the much brighter ones (see Tables 3 & 4 and Figs.
1114 2, 11 and 14). This is contrary to the general negative correlation between reflectance/pyroxene band
1115 strength and OH abundance. Very few exceptions to this observation (e.g., Oppia's ejecta) on Vesta
1116 were reported by Combe et al. (2015) and Le Corre et al. (2013). De Sanctis et al. (2015c) report higher
1117 OH abundances for the pitted material on the floor (with respect to the western crater wall material) and
1118 conclude that this material is linked to volatile-rich exogenic material. However, our observations
1119 including the brighter halo of the PIDs and newly calibrated VIR data from Combe et al. (2015) do not
1120 confirm their conclusion entirely.

1121 The crater-fill PIDs are depleted in OH with respect to other typical Vestan materials with the same
1122 reflectance and pyroxene band strength values. The 2.8 µm band absorption depth values are even lower
1123 than for the bright PIDs west and north of the crater. The presence of the halo (Fig. 12), which comprises
1124 very small pits, shows that the crater-fill PIDs of Marcia are not homogeneously darker and that there is
1125 compositional diversity among this material. The halo shows the same trend regarding reflectance and
1126 pyroxene band strength (Fig. 14) as the external PIDs. We therefore propose that for the central PIDs,
1127 their darker appearance in the VNIR range could result from the infall of 'dark material' from the crater
1128 rim due to space weathering mechanisms (Pieters et al., 2012) and mass wasting processes (Otto et al.,
1129 2013; Krohn et al., 2014) that prevail on Vesta. Especially on the eastern crater wall inflow of dark and
1130 partly also OH-rich material is observable (see Figure 2b & d, 12b and Scully et al., 2015). Thus, we
1131 speculate that the OH-depleted pitted floor originally exhibited high reflectance and pyroxene band
1132 strength similar to the halo at the margins of the crater-fill PIDs as well as to the area around the central

1133   peak. This would also be consistent with the spectral characteristics of the external PIDs. The crater-fill

1134   PIDs would then have gradually lost these spectral characteristics due to the input of dark material from

1135   the rim. As presented with DTM data (Fig. 9), the halo reaches higher slopes at the NW crater wall and

1136   might thus not be affected by the input of darker material. Moreover, the crater wall in the NW is much

1137   more pyroxene-dominated than other areas of the crater wall, possibly also leading to less input of dark

1138   material and/or more input of pyroxene-rich material from the walls. The large depletion of OH within

1139   the crater is consistent with the presence of the largest PIDs, i.e., the crater-fill deposit has been subject

1140   to higher temperatures and constitutes the most voluminous impactite deposit associated with craters.

1141   They are thereby the most prolonged heat source and continued to lose volatiles long after the smaller

1142   external deposits had cooled.

1143   The observations by Tosi et al. (2014) might support this hypothesis. They found a higher thermal inertia

1144   for the crater-fill deposits of Marcia indicating a larger component of less porous material (Tosi et al.,

1145   2014; De Sanctis et al., 2015c; Scully et al., 2015). Furthermore, there is no indication of a

1146   heterogeneous subsurface where the crater-fill PIDs reside. Instead, the surrounding bedrock exposed

1147   north and west of the crater-fill PIDs shows a eucritic signature with only a very small spectral indication

1148   of contamination (see supplementary Fig. S4) which is likely due to surficial processes (e.g., Pieters et

1149   al., 2012). The crater is currently roughly 8-9 km deep (from the current rim) while the excavation depth

1150   ranges from 3-7 km depending on the estimation method (one third of the transient cavity depth, Melosh,

1151   1989; estimates based on lower ballistic and upper melt-rich ejecta for Haughton crater on Earth, Osinski

1152   et al., 2011). Jaumann et al. (2014) reported the regolith layer in that region to be about 1 km thick,

1153   therefore it furthermore seems unlikely to find exogenic material at these depths as hypothesized by

1154   Scully et al. (2015). Given that typical crustal lithologies are expected beneath the regolith (i.e., eucrites;

1155   e.g., Binzel & Xu, 1993; Keil, 2002; McSween et al., 2011; McSween et al., 2013b and references

1156   therein) it seems even more intriguing that the Marcia impact mobilized such a large volume of volatiles

1157   shaping the surrounding geology while excavation depths might have reached deep below the surface

1158   regolith into a differentiated body. However, estimation of regolith thickness around Marcia by Jaumann

1159   et al. (2014) is based on visual observations of dark material while Denevi et al. (2016) assume regolith

1160   depths greater than 1 km based on blocky crater population. Thus, ejecta could possibly still be regolith-

1161   dominated. Modelling the formation of this crater could perhaps greatly enhance the understanding of

1162   volatiles involved in such a large low-gravity collision, especially given the observation that Marcia

1163   might have been an oblique impact and that oblique impacts favor survivability of impactor materials

1164   (e.g., Pierazzo & Melosh, 2000).

1165   Ejecta and crater fill materials can differ greatly due to the provenance of the materials they are

1166   comprised of, so the spectral characteristics of the crater-fill PID could also be a result of a different

1167   composition due to shed crater wall material, adding higher reflectance and pyroxene band strength

1168   materials (i.e., crustal material), especially to the margins of the crater-fill. The halo of the crater-fill on

1169   the margins and the central peak could therefore also represent added slumped and uplifted material

1170 with similar spectral characteristics. However, the halo is characterized by lower reflectance and similar

1171 750/917 [nm] ratios with respect to the crater-wall material, indicating that it is not derived from this

1172 compositional variation. Instead, the halo plots on the same unique trend presented in Figure 14,

1173 indicating that crater-fill and external PIDs share a common origin, independent of compositional

1174 differences.

1175

1176 *4.4 Distribution of volatiles*

1177 Ejecta units E1 and E2 significantly differ in their overall OH content (Fig. 2d). The VIR and GRaND

1178 instruments have detected higher concentrations of eucritic lithologies in and around Marcia (as opposed

1179 to diogenitic and howarditic lithologies, Prettyman et al., 2012; Ammannito et al., 2013a, De Sanctis et

1180 al., 2015b) indicating that the Marcia impact excavated eucritic crustal material. This generally conforms

1181 to the estimated excavation depth (3 to 7 km) and the estimated regolith thickness in this region (1 km,

1182 Jaumann et al., 2014). This higher eucritic concentration appears in both E1 and E2 as presented here

1183 (mainly east and west of Marcia, best illustrated in Russell et al., 2015) which could suggest that

1184 Calpurnia is not the source of ejecta unit E2a. If these eucrite-dominated lithologies were to source from

1185 the Calpurnia event, they would broadly occur around Calpurnia crater as well, which cannot be

1186 observed (Prettyman et al., 2013; Russell et al., 2015) though the data presented do not have a high

1187 spatial resolution. The Marcia region displays both large differences in OH contents but also increased

1188 eucritic lithologies, implying complex relationships between the observed materials. We have presented

1189 evidence that pitted surfaces do not form as a result of an especially high volatile content or the presence

1190 of ice at this location but rather through structural control. Nevertheless, volatiles are naturally required

1191 in the formation of PIDs, which is why we discuss the distribution of volatiles (i.e., the distribution of

1192 carbonaceous material) in the Marcia region in more detail.

1193 Our estimates of volatiles that were lost through the PIDs range around 10^8-10^9 m^3 (Table 2). As E2a is

1194 still very OH-rich (Figs. 2 and 4) clearly not all volatiles were lost during the impact, be it Marcia or

1195 Calpurnia. Reddy et al. (2012a) suggest that on average 1-6 vol% of CM2 chondrite material is mixed

1196 within the regolith of Vesta and that up to 50 vol% are locally possible. They present three equations

1197 (section 5.2) to calculate the CM2 content (vol%) of which the first two were derived by Le Corre et al.

1198 (2011) and are based on the reflectance at 750 nm and the parameter for pyroxene band strength

1199 (750/917 [nm]). The third equation was developed by Reddy et al. (2012a) and uses the ratio

1200 750/965 [nm]. We calculated the CM2 content for all of our regions of interest and for all three

1201 equations. The three equations and all calculated values can be found in the supplements (S6). Equation

1202 (1) which is based on the 750 nm reflectance gives the highest contents and equation (2) using the

1203 750/917 [nm] ratio gives the lowest values. The third equation has similar values as equation (2) with

1204 slightly higher estimates (typically 2 to 4 vol%). Results of equation (1) yield similar values like (2) and

1205 (3) for low reflectance regions but significantly higher values for higher reflectance regions which seems

1206 unrealistic. In the following, we use equation (3) as it appears to yield the most realistic results. We note

1207 at this point that the calculated values most likely do not represent the 'true' values as PIDs do not follow

1208 the 'typical' Vestan trend regarding their pyroxene band strength values (Fig. 14), which also affects the

1209 750/965 [nm] ratio.

1210 We calculate the difference in CM2 chondrite material between PIDs and their surroundings (based on

1211 values in Table 4) to be about 9 to 12 vol% which is slightly higher than Reddy et al. (2012a) suggest

1212 for the average abundance of CM2 chondrite material on a global scale. This difference corresponds to

1213 a difference of volatile material of roughly 1 wt% (assuming 11 % of mass loss during devolatilization,

1214 Garenne et al., 2014). The smooth surroundings of PIDs contain about 19 to 26 vol% CM2 material

1215 while the PIDs contain about 7 to 17 vol% of CM2 material. The volatile content of the surrounding of

1216 PIDs corresponds to about 2-3 wt%. Boyce et al. (2012) show for Tooting crater on Mars that a relatively

1217 low volume of volatiles can lead to extensive pitting as well. They estimate ~ 12 wt% of volatiles for

1218 Tooting crater target material but also acknowledge that for the Ries crater in Germany, Engelhardt et

1219 al. (1995) and Osinski (2003) observed that roughly half of the target volatiles were still present in

1220 impact glasses, reducing the released volume. This corresponds well to our calculations of volatiles lost

1221 (i.e., 1 wt% lost with host material volatile abundances of 2-3 wt%) based on the approaches by Reddy

1222 et al. (2012a) and Garenne et al. (2014) and is also consistent with the generally dryer nature of Vesta

1223 (i.e., no subsurface ice as opposed to Mars).

1224 Based on an average of 10 vol% of CM2 material loss, we calculated the volume of CM2 material now

1225 lost at the PIDs' sites (excluding the crater-fill) using the total size of PIDs (212 km^2, Table 2), average

1226 thicknesses of the PIDs' material (50 m, 100 m, 200 m, see section 3.2) and a porosity of 25 % which

1227 results in approximate total volumes of $0.9*10^9$ m^3, $1.8*10^9$ m^3 and $3.5*10^9$ m^3, respectively. We

1228 roughly estimate the regolith porosity (i.e., 25 %) from macro porosity estimates for the silicate portion

1229 of Vesta (8 %) by Ermakov et al. (2014), average howardite and eucrite porosities (11%) given in Macke

1230 et al. (2011a) and the decline in porosity near the surface from 55 % at the surface to 37 % at one meter

1231 depth (Palmer et al., 2015).

1232 Garenne et al. (2014) observe a mass loss of around 11 % between 200 and 700 °C (attributed to (oxy)

1233 hydroxides and the dehydroxylation of phyllosilicates) for their studied CM chondrites on which they

1234 performed thermogravimetric analysis combined with infrared spectroscopy in order to quantify the

1235 chondrite's water content. We assume here that the molecular waters lost between 0 and 200 °C are

1236 already gone within the whole ejecta (i.e., both PIDs and their smooth surroundings). Assuming the

1237 same percentage of volatiles lost during the devolatilization process occurring at the PIDs' sites, a grain

1238 density of 2900 kg/m^3 for the CM2 material (Macke et al., 2011b) and the assumption that the density

1239 of lost volatiles roughly equals 1000 kg/m^3 (the density of water vapor, upper limit), resulting volatile

1240 volumes are $2.8*10^8$ m^3, $5.7*10^8$ m^3 and $1.1*10^9$ m^3, respectively. These values are in very good

1241 agreement with the estimated values in Table 2 from pit statistics. For the crater-fill PIDs in Marcia, we

1242   assume a material thickness of 500 m and a lower porosity (15 %) accounting for more compacted

1243   material (Tosi et al., 2014; De Sanctis et al., 2015c; Scully et al., 2015). The volume of lost volatiles is

1244   then $8.5*10^9$ m^3 which is one order of magnitude higher than our estimates in Table 2, possibly resulting

1245   from underestimated pit depths in section 3.2, underestimated porosity or overestimated material

1246   thickness in this calculation.

1247   With the same equation derived in Reddy et al. (2012a), we furthermore calculate the average CM2

1248   content of E2a to be around 31 vol%. If we assume that this ejecta part formed exclusively from a 1 km

1249   thick contaminated regolith layer (Jaumann et al., 2014; neglecting the possibility E2a originates from

1250   the Calpurnia impact) and a crater radius of roughly 30 km, a volume of ~ 2800 km^3 of regolith material

1251   was redistributed by the impact. Assuming a symmetric distribution around Marcia with a radius of

1252   about 100 km (the farthest PID is 69 km off the crater rim) we calculate the average thickness of

1253   contaminated Marcia ejecta to be roughly 100 m, which is consistent with ejecta thicknesses estimated

1254   with the approach by McGetchin et al. (1973) for ejecta about 15 km off the Marcia rim. We

1255   acknowledge that this is a rough estimate with high variations between regions closer and farther from

1256   the rim and it does also not include Calpurnia as the possible origin of E2a. It is difficult to estimate the

1257   thickness of E2a as it is located right on the slopes of Vestalia Terra (mountains rising to ~ 10 km above

1258   the Marcia rim). Ejecta accumulated there and obscured much of the underlying topography. If we

1259   assume an average of 200 m thickness roughly accounting for this accumulation for an area of about

1260   13,000 km^2 (E2a, Fig. 3), a regolith porosity of roughly 25 % and a CM2 content of 31 vol%, roughly

1261 $6*10^{11}$ m^3 of CM2 material are still present within E2a which corresponds to $1.9*10^{11}$ m^3 of volatiles.

1262   This is a lower limit as there are possibly more E2-type ejecta below E1 ejecta (as seen at Laeta crater

1263   and possibly even at Aricia Tholus, Fig. 3). For E1 and E2b, the average CM2 content is ~ 16 vol% and

1264   24 vol%, respectively. For E1, with an assumed average thickness of 50 m and an extent of 11,000 km^2,

1265   the volume of still-present volatiles is ~ $2*10^{10}$ m^3. For E2b (100 m and 12,000 km^2), still-present

1266   volatiles are in the order of $7*10^{10}$ m^3. The estimated value of $1.9*10^{11}$ m^3 of volatiles still present in

1267   E2a is two to three orders of magnitude higher than our estimates of lost volatiles through volatile

1268   degassing at the PIDs' sites. Most of the hydroxyl groups bound in minerals/phyllosilicates were

1269   therefore not liberated during the impact (be it Marcia or Calpurnia) and the volatiles lost by rapid vent-

1270   forming devolatilization represent a small fraction (< 2 %) of volatiles still present in the whole area.

1271   This furthermore illustrates that PID formation does not depend on the volatile content at their specific

1272   location as volatiles are still ubiquitous in the ejecta blanket. They were lost at the PIDs' sites due to

1273   topography-dependent ejecta accumulation and the resulting increase in deposit thickness and internal

1274   heat.

1275   Independent of whether Marcia or Calpurnia generated the ejecta unit E2a, the regolith where the Marcia

1276   impactor hit held at least 31 vol% of CM2 material which is an unreasonably high amount (Reddy et al.,

1277   2012a) for a large regional area like the ~ 30 km radius of pre-Marcia or ~ 25 km radius of pre-Calpurnia

1278   regolith, yet the three equations to calculate CM2 content by Le Corre et al., 2011 and Reddy et al.,

1279 2012a generate similar values for E2a (see S6) and E2a furthermore shows the highest large-scale

1280 abundance of OH (i.e., strongest absorptions at 2.8 µm, Combe et al., 2015). The Veneneia impact basin

1281 which is thought to have delivered most of the dark material is close to Marcia (e.g., Schenk et al., 2012;

1282 Jaumann et al., 2014) which could be the reason for this abnormally high amount of carbonaceous

1283 chondrite material within the regolith, yet does not entirely explain the strong dichotomy of the ejecta

1284 units which remains an open question.

1285

1286 5 Summary & Conclusions

1287 This work studies the spectral and geomorphologic properties of pitted impact deposits (PIDs) related

1288 to the young, large impact crater Marcia (and Calpurnia) on Vesta. By analyzing FC data, we find that

1289 volatile release shaping the characteristic pits within the PIDs is linked to topography-controlled

1290 accumulation of ejecta and the accompanied increase of deposit thickness and internal amount of heat,

1291 resulting in the prolonged retention of heat within the material and larger volumes of heat-bearing

1292 material with respect to the deposit's surface area. Pitted surfaces on impact deposits are often found

1293 within pre-existing craters and along scarps and crater-walls, enabling the estimation of pre-existing

1294 topography and deposit thickness. PID formation is therefore most likely not linked to exceptionally

1295 high, location-specific volatile contents or subsurface ice deposits as suggested by Scully et al. (2015).

1296 The pitted surfaces of PIDs display an 'enhancement' of eucritic characteristics, i.e. higher reflectance

1297 at 750 nm and higher pyroxene band strength (750/917 [nm]). This most likely corresponds to less

1298 contamination by carbonaceous chondrite material in contrast to grain size, roughness or glass content.

1299 Yet we note that the observed changes to the deposit material do not conform entirely with the trend

1300 given by carbonaceous contamination. We observe a unique spectral trend for PIDs with respect to their

1301 smooth surroundings and/or other typical Vestan materials regarding reflectance, pyroxene band

1302 strength and 2.8 µm absorptions. The most likely explanation for this spectral enhancement of eucritic

1303 characteristics is the loss and decomposition of exogenic volatile-rich material upon prolonged heating.

1304 This is consistent with the hypothesis presented by Denevi et al. (2012) (which was based on findings

1305 from Tornabene et al., 2012 and Boyce et al., 2012 for Martian PIDs).

1306 Heating studies of meteorites and analog materials generally show a loss of reflectance and spectral

1307 features upon heating, which is why it remains difficult to explain this spectral phenomenon, especially

1308 the increase of pyroxene band strength with respect to other Marcia-related materials with similar

1309 reflectance values. However, Vesta-related experiments have not yet been undertaken. The unique PID-

1310 forming process on Mars includes excavation of entrained particles/clasts/fragments through the

1311 devolatilization conduits (Tornabene et al., 2012; Boyce et al., 2012) which might play an additional

1312 role on Vesta if these clasts were eucrite-dominated. This might enhance the effect of the loss of CM2

1313 compounds and explain the unique spectral trend. This is also consistent with the observed spectral halo

1314 around the pitted surfaces, covering smooth surfaces beyond the pits. Nevertheless, it remains

1315 challenging to judge whether the expected spectral effects from such an excavation of eucrite-dominated
1316 clasts could really conform to the observed deviation from the typical Vestan spectral trend which is
1317 especially related to the higher band strength values of the PIDs. Thus, the petrologic and geochemical
1318 details of PID formation remain uncertain.

1319 The spectral characteristics of the crater-fill PIDs, which are by far the largest of all PIDs observed, are
1320 heterogeneous. Most of the PIDs' surface show lower reflectance and pyroxene band strength than their
1321 surroundings (i.e., the crater walls) but also the lowest 2.8 μm band depth values among PIDs. This
1322 contradicts the general anti-correlation between OH abundance and reflectance/pyroxene band strength
1323 as observed for all other PIDs related to Marcia. We speculate this might result from inflow of dark
1324 material from the crater rim by mass wasting processes. The original surface of the crater-fill PIDs likely
1325 exhibited higher reflectance and pyroxene band strength similar to the halo observed on the margins of
1326 the crater-fill PIDs and close to the central peak. This halo shows the same unique spectral characteristics
1327 as the external PIDs regarding reflectance and pyroxene band strength and therefore, the crater-fill PIDs
1328 might still have experienced the same unique process. However, the halo moreover comprises much
1329 smaller individual pits as does the immediate surrounding of the central peak which additionally shows
1330 signs of subsidence. This might indicate a secondary devolatilization process within the crater-fill
1331 deposit.

1332 PIDs occur within spectrally distinct ejecta units and accordingly hold different spectral and
1333 morphological properties, likely related to the initial abundance of volatiles/chondritic material in each
1334 ejecta unit. Based on equation (3) in Reddy et al. (2012a) we calculate the difference in CM2 chondrite
1335 material between PIDs and their surroundings to be about 8 to 12 vol% which would correspond to a
1336 difference of ~ 1 wt% volatiles. We roughly estimated the volume of volatiles that were lost through the
1337 explosive devolatilization within the PIDs material as well as the volume of volatiles still present in the
1338 ejecta. We find that volatiles lost from PIDs likewise represent only a small fraction of the volatiles still
1339 present in the ejecta (< 2 %). This furthermore illustrates that PID formation is not tied to an
1340 exceptionally high availability of volatiles (i.e., carbonaceous chondrite material). The inferred volumes
1341 of now lost volatiles from these calculations are in good agreement with volumes calculated from pit
1342 statistics.

1343

1344 6 Acknowledgements

49

1357

1358   7 References

1359   Akai, J. (1992). T-T-T diagram of serpentine and saponite, and estimation of metamorphic heating degree of Antarctic
1360   carbonaceous chondrites. *Antarctic Meteorite Research, 5*, 120.

1361   Alemanno, G., Maturilli, A., Helbert, J., & D'Amore, M. (2020). Laboratory studies on the 3 µm spectral features of Mg-rich
1362   phyllosilicates with temperature variations in support of the interpretation of small asteroid surface spectra. *546*,
1363   116424. doi:10.1016/j.epsl.2020.116424

1364   Ammannito, E., De Sanctis, M. C., Capaccioni, F., Capria, M. T., Carraro, F., Combe, J. P., Fonte, S., Frigeri, A., Joy, S. P.,
1365   Longobardo, A., Magni, G., Marchi, S., McCord, T. B., McFadden, L. A., McSween, H. Y., Palomba, E., Pieters, C. M.,
1366   Polanskey, C. A., Raymond, C. A., Sunshine, J. M., Tosi, F., Zambon, F., & Russell, C. T. (2013a). Vestan lithologies
1367   mapped by the visual and infrared spectrometer on Dawn. *Meteoritics & Planetary Science, 48*(11), 2185-2198.
1368   doi:10.1111/maps.12192

1369   Ammannito, E., de Sanctis, M. C., Palomba, E., Longobardo, A., Mittlefehldt, D. W., McSween, H. Y., Marchi, S., Capria, M. T.,
1370   Capaccioni, F., Frigeri, A., Pieters, C. M., Ruesch, O., Tosi, F., Zambon, F., Carraro, F., Fonte, S., Hiesinger, H., Magni,
1371   G., McFadden, L. A., Raymond, C. A., Russell, C. T., & Sunshine, J. M. (2013b). Olivine in an unexpected location on
1372   Vesta's surface. *Nature, 504*, 122.

1373   Beck, A. W., McCoy, T. J., Sunshine, J. M., Viviano, C. E., Corrigan, C. M., Hiroi, T., & Mayne, R. G. (2013). Challenges in
1374   detecting olivine on the surface of 4 Vesta. *Meteoritics & Planetary Science, 48*(11), 2155-2165. doi:10.1111/maps.12160

1375   Binzel, R. P., & Xu, S. (1993). Chips off of Asteroid 4 Vesta: Evidence for the Parent Body of Basaltic Achondrite Meteorites.
1376   *260*, 186. doi:10.1126/science.260.5105.186

1377   Blewett, D. T., Chabot, N. L., Denevi, B. W., Ernst, C. M., Head, J. W., Izenberg, N. R., Murchie, S. L., Solomon, S. C., Nittler, L.
1378   R., McCoy, T. J., Xiao, Z., Baker, D. M. H., Fassett, C. I., Braden, S. E., Oberst, J., Scholten, F., Preusker, F., &
1379   Hurwitz, D. M. (2011). Hollows on Mercury: MESSENGER Evidence for Geologically Recent Volatile-Related
1380   Activity. *Science, 333*, 1856.

1381   Blewett, D. T., Vaughan, W. M., Xiao, Z., Chabot, N. L., Denevi, B. W., Ernst, C. M., Helbert, J., D'Amore, M., Maturilli, A.,
1382   Head, J. W., & Solomon, S. C. (2013). Mercury's hollows: Constraints on formation and composition from analysis of
1383   geological setting and spectral reflectance. *Journal of Geophysical Research (Planets), 118*, 1013-1032.

1384   Bottke, W. F., Nolan, M. C., Greenberg, R., & Kolvoord, R. A. (1994). Velocity Distributions among Colliding Asteroids. *Icarus,*
1385   *107*, 255-268.

1386   Boyce, J. M., Wilson, L., Mouginis-Mark, P. J., Hamilton, C. W., & Tornabene, L. L. (2012). Origin of small pits in martian impact
1387   craters. *Icarus, 221*, 262-275.

1388   Clark, B. E., Fanale, F. P., & Robinson, M. S. (1993). Simulation of possible Regolith Alteration Effects on Carbonaceous
1389   Chondrite Meteorites. Paper presented at the Lunar and Planetary Science Conference XXIV. pp. 301-302, Abstract

1390   Clark, R. N. (1999). Spectroscopy of Rocks and Minerals, and Principles of Spectroscopy. In A. N. Rencz (Ed.), *Remote Sensing for*
1391   *the Earth Sciences: Manual of Remote Sensing* (Vol. 3): John Wiley & Sons, Inc.

1392   Cloutis, E. A., Hudon, P., Hiroi, T., & Gaffey, M. J. (2012). Spectral reflectance properties of carbonaceous chondrites 4:
1393   Aqueously altered and thermally metamorphosed meteorites. *220*, 586. doi:10.1016/j.icarus.2012.05.018

1394   Cloutis, E. A., Izawa, M. R. M., Pompilio, L., Reddy, V., Hiesinger, H., Nathues, A., Mann, P., Le Corre, L., Palomba, E., & Bell,
1395   J. F. (2013a). Spectral reflectance properties of HED meteorites + CM2 carbonaceous chondrites: Comparison to HED
1396   grain size and compositional variations and implications for the nature of low-albedo features on Asteroid 4 Vesta.
1397   *Icarus, 223*, 850-877.

1398   Cloutis, E. A., Mann, P., Izawa, M. R. M., Nathues, A., Reddy, V., Hiesinger, H., Le Corre, L., & Palomba, E. (2013b). The 2.5-5.1
1399   µm reflectance spectra of HED meteorites and their constituent minerals: Implications for Dawn. *Icarus, 225*, 581-601.

1400   Combe, J.-P., Ammannito, E., Tosi, F., De Sanctis, M. C., McCord, T. B., Raymond, C. A., & Russell, C. T. (2015). Reflectance
1401   properties and hydrated material distribution on Vesta: Global investigation of variations and their relationship using
1402   improved calibration of Dawn VIR mapping spectrometer. *Icarus, 259*, 21-38.

1403   Combe, J.-P., McCord, T. B., Tosi, F., Ammannito, E., Carrozzo, F. G., De Sanctis, M. C., Raponi, A., Byrne, S., Landis, M. E.,
1404   Hughson, K. H. G., Raymond, C. A., & Russell, C. T. (2016). Detection of local H_2O exposed at the surface of Ceres.
1405   *353*, aaf3010. doi:10.1126/science.aaf3010

1406   Consolmagno, G. J., & Drake, M. J. (1977). Composition and evolution of the eucrite parent body: evidence from rare earth
1407   elements. *41*, 1271. doi:10.1016/0016-7037(77)90072-2

1408   De Sanctis, M. C., Ammannito, E., Capria, M. T., Capaccioni, F., Combe, J.-P., Frigeri, A., Longobardo, A., Magni, G., Marchi, S.,
1409   McCord, T. B., Palomba, E., Tosi, F., Zambon, F., Carraro, F., Fonte, S., Li, Y. J., McFadden, L. A., Mittlefehldt, D.
1410   W., Pieters, C. M., Jaumann, R., Stephan, K., Raymond, C. A., & Russell, C. T. (2013). Vesta's mineralogical

composition as revealed by the visible and infrared spectrometer on Dawn. *Meteoritics and Planetary Science, 48*, 2166-2184.

De Sanctis, M. C., Ammannito, E., Capria, M. T., Tosi, F., Capaccioni, F., Zambon, F., Carraro, F., Fonte, S., Frigeri, A., Jaumann, R., Magni, G., Marchi, S., McCord, T. B., McFadden, L. A., McSween, H. Y., Mittlefehldt, D. W., Nathues, A., Palomba, E., Pieters, C. M., Raymond, C. A., Russell, C. T., Toplis, M. J., & Turrini, D. (2012a). Spectroscopic Characterization of Mineralogy and Its Diversity Across Vesta. *Science, 336*(6082), 697-700. doi:10.1126/science.1219270

De Sanctis, M. C., Ammannito, E., Raponi, A., Marchi, S., McCord, T. B., McSween, H. Y., Capaccioni, F., Capria, M. T., Carrozzo, F. G., Ciarniello, M., Longobardo, A., Tosi, F., Fonte, S., Formisano, M., Frigeri, A., Giardino, M., Magni, G., Palomba, E., Turrini, D., Zambon, F., Combe, J.-P., Feldman, W., Jaumann, R., McFadden, L. A., Pieters, C. M., Prettyman, T., Toplis, M., Raymond, C. A., & Russell, C. T. (2015a). Ammoniated phyllosilicates with a likely outer Solar System origin on (1) Ceres. *528*, 241. doi:10.1038/nature16172

De Sanctis, M. C., Combe, J.-P., Ammannito, E., Palomba, E., Longobardo, A., McCord, T. B., Marchi, S., Capaccioni, F., Capria, M. T., Mittlefehldt, D. W., Pieters, C. M., Sunshine, J., Tosi, F., Zambon, F., Carraro, F., Fonte, S., Frigeri, A., Magni, G., Raymond, C. A., Russell, C. T., & Turrini, D. (2012b). Detection of Widespread Hydrated Materials on Vesta by the VIR Imaging Spectrometer on board the Dawn Mission. *The Astrophysical Journal Letters, 758*.

De Sanctis, M. C., Combe, J. P., Ammannito, A., Frigeri, A., Longobardo, A., Palomba, E., Tosi, F., Zambon, F., Stephan, K., Raymond, C. A., & Russell, C. T. (2015b). Eucritic crust remnants and the effect of in-falling hydrous carbonaceous chondrites characterizing the composition of Vesta's Marcia region. *Icarus, 259*, 91-115. doi:10.1016/j.icarus.2015.05.014

De Sanctis, M. C., Coradini, A., Ammannito, E., Filacchione, G., Capria, M. T., Fonte, S., Magni, G., Barbis, A., Bini, A., Dami, M., Ficai-Veltroni, I., & Preti, G. (2011). The VIR Spectrometer. *Space Science Reviews, 163*(1), 329-369. doi:10.1007/s11214-010-9668-5

De Sanctis, M. C., Frigeri, A., Ammannito, E., Tosi, F., Marchi, S., Zambon, F., Raymond, C. A., & Russell, C. T. (2015c). Mineralogy of Marcia, the youngest large crater of Vesta: Character and distribution of pyroxenes and hydrated material. *Icarus, 248*, 392-406.

Denevi, B. W., Beck, A. W., Coman, E. I., Thomson, B. J., Ammannito, E., Blewett, D. T., Sunshine, J. M., de Sanctis, M. C., Li, J.-Y., Marchi, S., Mittlefehldt, D. W., Petro, N. E., Raymond, C. A., & Russell, C. T. (2016). Global variations in regolith properties on asteroid Vesta from Dawn's low-altitude mapping orbit. *51*, 2366. doi:10.1111/maps.12729

Denevi, B. W., Blewett, D. T., Buczkowski, D. L., Capaccioni, F., Capria, M. T., De Sanctis, M. C., Garry, W. B., Gaskell, R. W., Le Corre, L., Li, J.-Y., Marchi, S., McCoy, T. J., Nathues, A., O'Brien, D. P., Petro, N. E., Pieters, C. M., Preusker, F., Raymond, C. A., Reddy, V., Russell, C. T., Schenk, P., Scully, J. E. C., Sunshine, J. M., Tosi, F., Williams, D. A., & Wyrick, D. (2012). Pitted Terrain on Vesta and Implications for the Presence of Volatiles. *Science, 338*(6104), 246. doi:10.1126/science.1225374

Engelhardt, W. V. (1972). Shock produced rock glasses from the Ries crater. *36*, 265. doi:10.1007/bf00444336

Engelhardt, W. V., Arndt, J., Fecker, B., & Pankau, H. G. (1995). Suevite breccia from the Ries crater, Germany: Origin, cooling history and devitrification of impact glasses. *Meteoritics, 30*, 279. doi:10.1111/j.1945-5100.1995.tb01126.x

Ermakov, A. I., Fu, R. R., Castillo-Rogez, J. C., Raymond, C. A., Park, R. S., Preusker, F., Russell, C. T., Smith, D. E., & Zuber, M. T. (2017). Constraints on Ceres' Internal Structure and Evolution From Its Shape and Gravity Measured by the Dawn Spacecraft. *122*, 2267. doi:10.1002/2017je005302

Ermakov, A. I., Zuber, M. T., Smith, D. E., Raymond, C. A., Balmino, G., Fu, R. R., & Ivanov, B. A. (2014). Constraints on Vesta's interior structure using gravity and shape models from the Dawn mission. *Icarus, 240*, 146-160. doi:10.1016/j.icarus.2014.05.015

Fu, R. R., Ermakov, A. I., Marchi, S., Castillo-Rogez, J. C., Raymond, C. A., Hager, B. H., Zuber, M. T., King, S. D., Bland, M. T., Cristina De Sanctis, M., Preusker, F., Park, R. S., & Russell, C. T. (2017). The interior structure of Ceres as revealed by surface topography. *476*, 153. doi:10.1016/j.epsl.2017.07.053

Gaffey, M. J. (1976). Spectral reflectance characteristics of the meteorite classes. *Journal of Geophysical Research, 81*, 905.

Galiano, A., Dirri, F., Palomba, E., Longobardo, A., Schmitt, B., & Beck, P. (2020). Spectral investigation of Ceres analogue mixtures: In-depth analysis of crater central peak material (ccp) on Ceres. *Icarus, 343*, 113692.

Garenne, A., Beck, P., Montes-Hernandez, G., Chiriac, R., Toche, F., Quirico, E., Bonal, L., & Schmitt, B. (2014). The abundance and stability of "water" in type 1 and 2 carbonaceous chondrites (CI, CM and CR). *Geochimica et Cosmochimica Acta, 137*, 93.

Harloff, J., & Arnold, G. (2001). Near-infrared reflectance spectroscopy of bulk analog materials for planetary crust. *49*, 191. doi:10.1016/s0032-0633(00)00132-x

Hiroi, T., Zolensky, M. E., Pieters, C. M., & Lipschutz, M. E. (1996). Thermal metamorphism of the C, G, B, and F asteroids seen from the 0.7 micron, 3 micron and UV absorption strengths in comparison with carbonaceous chondrites. *31*, 321. doi:10.1111/j.1945-5100.1996.tb02068.x

Hiroi, T., & Zolensky, M. E. J. A. M. R. (1999). UV-Vis-NIR absorption features of heated phyllosilicates as remote-sensing clues of thermal histories of primitive asteroids. *12*, 108.

Jaumann, R., Nass, A., Otto, K., Krohn, K., Stephan, K., McCord, T. B., Williams, D. A., Raymond, C. A., Blewett, D. T., Hiesinger, H., Yingst, R. A., De Sanctis, M. C., Palomba, E., Roatsch, T., Matz, K.-D., Preusker, F., Scholten, F., & Russell, C. T. (2014). The geological nature of dark material on Vesta and implications for the subsurface structure. *Icarus, 240*, 3-19. doi:10.1016/j.icarus.2014.04.035

Keihm, S., Tosi, F., Capria, M. T., De Sanctis, M. C., Longobardo, A., Palomba, E., Russell, C. T., & Raymond, C. A. (2015). Separation of thermal inertia and roughness effects from Dawn/VIR measurements of Vesta surface temperatures in the vicinity of Marcia Crater. *Icarus, 262*, 30-43.

Keil, K. (2002). Geological History of Asteroid 4 Vesta: The "Smallest Terrestrial Planet". In *Asteroids III* (pp. 573).

Krohn, K., Jaumann, R., Otto, K., Hoogenboom, T., Wagner, R., Buczkowski, D. L., Garry, B., Williams, D. A., Yingst, R. A., Scully, J., De Sanctis, M. C., Kneissl, T., Schmedemann, N., Kersten, E., Stephan, K., Matz, K. D., Pieters, C. M.,

1480   Preusker, F., Roatsch, T., Schenk, P., Russell, C. T., & Raymond, C. A. (2014). Mass movement on Vesta at steep scarps
1481   and crater rims. *Icarus, 244*, 120-132. doi:10.1016/j.icarus.2014.03.013
1482 Larson, H. P., & Fink, U. (1975). Infrared Spectral Observations of Asteroid 4 Vesta. *26*, 420. doi:10.1016/0019-1035(75)90109-8
1483 Le Corre, L., Reddy, V., Nathues, A., & Cloutis, E. A. (2011). How to characterize terrains on 4 Vesta using Dawn Framing
1484   Camera color bands? *, 216*, 376. doi:10.1016/j.icarus.2011.09.014
1485 Le Corre, L., Reddy, V., Schmedemann, N., Becker, K. J., O'Brien, D. P., Yamashita, N., Peplowski, P. N., Prettyman, T. H., Li,
1486   J.-Y., Cloutis, E. A., Denevi, B. W., Kneissl, T., Palmer, E., Gaskell, R. W., Nathues, A., Gaffey, M. J., Mittlefehldt, D.
1487   W., Garry, W. B., Sierks, H., Russell, C. T., Raymond, C. A., De Sanctis, M. C., & Ammannito, E. (2013). Olivine or
1488   impact melt: Nature of the "Orange" material on Vesta from Dawn. *Icarus, 226*(2), 1568-1594.
1489   doi:10.1016/j.icarus.2013.08.013
1490 Macke, R. J., Britt, D. T., & Consolmagno, G. J. (2011a). Density, porosity, and magnetic susceptibility of achondritic meteorites.
1491   *46*, 311. doi:10.1111/j.1945-5100.2010.01155.x
1492 Macke, R. J., Consolmagno, G. J., & Britt, D. T. (2011b). Density, porosity, and magnetic susceptibility of carbonaceous
1493   chondrites. *46*, 1842. doi:10.1111/j.1945-5100.2011.01298.x
1494 Marchi, S., Bottke, W. F., Cohen, B. A., Wünnemann, K., Kring, D. A., McSween, H. Y., de Sanctis, M. C., O'Brien, D. P.,
1495   Schenk, P., Raymond, C. A., & Russell, C. T. (2013). High-velocity collisions from the lunar cataclysm recorded in
1496   asteroidal meteorites. *Nature Geoscience, 6*, 303-307.
1497 Marchi, S., McSween, H. Y., O'Brien, D. P., Schenk, P., De Sanctis, M. C., Gaskell, R., Jaumann, R., Mottola, S., Preusker, F.,
1498   Raymond, C. A., Roatsch, T., & Russell, C. T. (2012). The Violent Collisional History of Asteroid 4 Vesta. *Science,*
1499   *336*(6082), 690-694. doi:10.1126/science.1218757
1500 McCord, T. B., Adams, J. B., & Johnson, T. V. (1970). Asteroid Vesta: Spectral Reflectivity and Compositional Implications.
1501   *Science, 168*, 1445-1447.
1502 McCord, T. B., Li, J.-Y., Combe, J.-P., McSween, H. Y., Jaumann, R., Reddy, V., Tosi, F., Williams, D. A., Blewett, D. T., Turrini,
1503   D., Palomba, E., Pieters, C. M., de Sanctis, M. C., Ammannito, E., Capria, M. T., Le Corre, L., Longobardo, A.,
1504   Nathues, A., Mittlefehldt, D. W., Schröder, S. E., Hiesinger, H., Beck, A. W., Capaccioni, F., Carsenty, U., Keller, H. U.,
1505   Denevi, B. W., Sunshine, J. M., Raymond, C. A., & Russell, C. T. (2012). Dark material on Vesta from the infall of
1506   carbonaceous volatile-rich material. *Nature, 491*(7422), 83-86. doi:10.1038/nature11561
1507 McGetchin, T. R., Settle, M., & Head, J. W. (1973). Radial thickness variation in impact crater ejecta: Implications for lunar basin
1508   deposits. *Earth and Planetary Science Letters, 20*, 226-236. doi:10.1016/0012-821X(73)90162-3
1509 McSween, H. Y., Ammannito, E., Reddy, V., Prettyman, T. H., Beck, A. W., Cristina de Sanctis, M., Nathues, A., Corre, L. L.,
1510   O'Brien, D. P., Yamashita, N., McCoy, T. J., Mittlefehldt, D. W., Toplis, M. J., Schenk, P., Palomba, E., Turrini, D.,
1511   Tosi, F., Zambon, F., Longobardo, A., Capaccioni, F., Raymond, C. A., & Russell, C. T. (2013a). Composition of the
1512   Rheasilvia basin, a window into Vesta's interior. *Journal of Geophysical Research (Planets), 118*(2), 335-346.
1513   doi:10.1002/jgre.20057
1514 McSween, H. Y., Binzel, R. P., de Sanctis, M. C., Ammannito, E., Prettyman, T. H., Beck, A. W., Reddy, V., Corre, L., Gaffey, M.
1515   J., McCord, T. B., Raymond, C. A., & Russell, C. T. (2013b). Dawn; the Vesta-HED connection; and the geologic
1516   context for eucrites, diogenites, and howardites. *Meteoritics and Planetary Science, 48*, 2090-2104.
1517 McSween, H. Y., Mittlefehldt, D. W., Beck, A. W., Mayne, R. G., & McCoy, T. J. (2011). HED Meteorites and Their Relationship
1518   to the Geology of Vesta and the Dawn Mission. *Space Science Reviews, 163*, 141-174.
1519 Melosh, H. J. (1989). *Impact cratering: A geologic process*.
1520 Mittlefehldt, D. W. (2015). Asteroid (4) Vesta: I. The howardite-eucrite-diogenite (HED) clan of meteorites. *Chemie der Erde /*
1521   *Geochemistry, 75*(2), 155-183. doi:10.1016/j.chemer.2014.08.002
1522 Mittlefehldt, D. W., Greenwood, R. C., Peng, Z. X., Ross, D. K., Berger, E. L., & Barrett, T. J. (2016). Petrologic and Oxygen-
1523   Isotopic Investigations of Eucritic and Anomalous Mafic Achondrites. Paper presented at the 47th Lunar and Planetary
1524   Science Conference. pp. 1240, Abstract
1525 Miyamoto, M. (1991). Thermal Metamorphism of CI and CM Carbonaceous Chondrites: an Internal Heating Model. *26*, 111.
1526   doi:10.1111/j.1945-5100.1991.tb01026.x
1527 Nakamura, T. (2005). Post-hydration thermal metamorphism of carbonaceous chondrites. *Journal of Mineralogical and Petrological*
1528   *Sciences, 100*, 260-272. doi:10.2465/jmps.100.260
1529 Nathues, A., Schäfer, M., Reddy, V., Hoffmann, M., Thangjam, G., Le Corre, L., Sierks, H., Cloutis, E. A., Christensen, U.,
1530   Mengel, K., Vincent, J. B., & Russell, C. T. (2014). Vesta's diverse lithologies from Dawn FC. *European Planetary Science*
1531   *Congress 2014, EPSC Abstracts, Vol. 9, id. EPSC2014-251, 9.*
1532 Neish, C. D., Cannon, K. M., Tornabene, L. L., Flemming, R. L., Zanetti, M., & Pilles, E. (2021). Spectral properties of lunar
1533   impact melt deposits from Moon Mineralogy Mapper (M^3) data. *361*, 114392.
1534   doi:10.1016/j.icarus.2021.114392
1535 Newsom, H. E., Graup, G., Sewards, T., & Keil, K. J. J. o. G. R. (1986). Fluidization and hydrothermal alteration of the suevite
1536   deposit at the Ries crater, West Germany, and implications for Mars. *91*, E239. doi:10.1029/JB091iB13p0E239
1537 Osinski, G. R. (2003). Impact glasses in fallout suevites from the Ries impact structure, Germany: An analytical SEM study.
1538   *Meteoritics and Planetary Science, 38*, 1641-1667. doi:10.1111/j.1945-5100.2003.tb00006.x
1539 Osinski, G. R., Tornabene, L. L., & Grieve, R. A. F. (2011). Impact ejecta emplacement on terrestrial planets. *Earth and Planetary*
1540   *Science Letters, 310*, 167-181. doi:10.1016/j.epsl.2011.08.012
1541 Otto, K. A., Jaumann, R., Krohn, K., Matz, K.-D., Preusker, F., Roatsch, T., Schenk, P., Scholten, F., Stephan, K., Raymond, C.
1542   A., & Russell, C. T. (2013). Mass-wasting features and processes in Vesta's south polar basin Rheasilvia. *Journal of*
1543   *Geophysical Research (Planets), 118*(11), 2279-2294. doi:10.1002/2013JE004333
1544 Palmer, E. M., Heggy, E., Capria, M. T., & Tosi, F. (2015). Dielectric properties of Asteroid Vesta's surface as constrained by
1545   Dawn VIR observations. *262*, 93. doi:10.1016/j.icarus.2015.08.031
1546 Palomba, E., Longobardo, A., De Sanctis, M. C., Zinzi, A., Ammannito, E., Marchi, S., Tosi, F., Zambon, F., Capria, M. T.,
1547   Russell, C. T., Raymond, C. A., & Cloutis, E. A. (2015). Detection of new olivine-rich locations on Vesta. *Icarus, 258*,
1548   120-134. doi:10.1016/j.icarus.2015.06.011

1549 Pasckert, J. H., Hiesinger, H., Ruesch, O., Williams, D. A., Naß, A., Kneissl, T., Mest, S. C., Buczkowski, D. L., Scully, J. E. C.,
1550   Schmedemann, N., Jaumann, R., Roatsch, T., Preusker, F., Nathues, A., Hoffmann, M., Schäfer, M., De Sanctis, M. C.,
1551   Raymond, C. A., & Russell, C. T. (2018). Geologic mapping of the Ac-2 Coniraya quadrangle of Ceres from NASA's
1552   Dawn mission: Implications for a heterogeneously composed crust. *Icarus, 316*, 28-45. doi:10.1016/j.icarus.2017.06.015
1553 Pierazzo, E., & Melosh, H. J. (2000). Hydrocode modeling of oblique impacts: The fate of the projectile. *Meteoritics & Planetary*
1554   *Science, vol. 35, no. 1, pp. 117-130 (2000). 35*, 117-130. doi:10.1111/j.1945-5100.2000.tb01979.x
1555 Pieters, C. M., Ammannito, E., Blewett, D. T., Denevi, B. W., de Sanctis, M. C., Gaffey, M. J., Le Corre, L., Li, J.-Y., Marchi, S.,
1556   McCord, T. B., McFadden, L. A., Mittlefehldt, D. W., Nathues, A., Palmer, E., Reddy, V., Raymond, C. A., & Russell,
1557   C. T. (2012). Distinctive space weathering on Vesta from regolith mixing processes. *Nature, 491*(7422), 79-82.
1558   doi:10.1038/nature11534
1559 Pieters, C. M., Staid, M. I., Fischer, E. M., Tompkins, S., & He, G. (1994). A Sharper View of Impact Craters from Clementine
1560   Data. *Science, 266*, 1844-1848.
1561 Poch, O., Pommerol, A., Jost, B., Carrasco, N., Szopa, C., & Thomas, N. (2016). Sublimation of water ice mixed with silicates and
1562   tholins: Evolution of surface texture and reflectance spectra, with implications for comets. *Icarus, 267*, 154.
1563 Prettyman, T. H., Mittlefehldt, D. W., Yamashita, N., Beck, A. W., Feldman, W. C., Hendricks, J. S., Lawrence, D. J., McCoy, T.
1564   J., McSween, H. Y., Peplowski, P. N., Reedy, R. C., Toplis, M. J., Le Corre, L., Mizzon, H., Reddy, V., Titus, T. N.,
1565   Raymond, C. A., & Russell, C. T. (2013). Neutron absorption constraints on the composition of 4 Vesta. *Meteoritics &*
1566   *Planetary Science, 48*(11), 2211-2236. doi:10.1111/maps.12244
1567 Prettyman, T. H., Mittlefehldt, D. W., Yamashita, N., Lawrence, D. J., Beck, A. W., Feldman, W. C., McCoy, T. J., McSween, H.
1568   Y., Toplis, M. J., Titus, T. N., Tricarico, P., Reedy, R. C., Hendricks, J. S., Forni, O., Le Corre, L., Li, J.-Y., Mizzon, H.,
1569   Reddy, V., Raymond, C. A., & Russell, C. T. (2012). Elemental Mapping by Dawn Reveals Exogenic H in Vesta's
1570   Regolith. *Science, 338*, 242.
1571 Preusker, F., Scholten, F., Matz, K.-D., Roatsch, T., Jaumann, R., Raymond, C. A., & Russell, C. T. (2014). Global Shape of (4)
1572   Vesta from Dawn FC Stereo Images. Paper presented at the Vesta in the Light of Dawn: First Exploration of a
1573   Protoplanet in the Asteroid Belt. pp. 2027, Abstract
1574 Preusker, F., Scholten, F., Matz, K.-D., Roatsch, T., Jaumann, R., Raymond, C. A., & Russell, C. T. J. N. P. D. S. (2016). Dawn
1575   FC2 Derived Vesta DTM SPG V1.0. DAWN-A-FC2-5-VESTADTMSPG-V1.0.
1576 Reddy, V., Le Corre, L., O'Brien, D. P., Nathues, A., Cloutis, E. A., Durda, D. D., Bottke, W. F., Bhatt, M. U., Nesvorny, D.,
1577   Buczkowski, D., Scully, J. E. C., Palmer, E. M., Sierks, H., Mann, P. J., Becker, K. J., Beck, A. W., Mittlefehldt, D., Li,
1578   J.-Y., Gaskell, R., Russell, C. T., Gaffey, M. J., McSween, H. Y., McCord, T. B., Combe, J.-P., & Blewett, D. (2012a).
1579   Delivery of dark material to Vesta via carbonaceous chondritic impacts. *Icarus, 221*, 544-559.
1580   doi:10.1016/j.icarus.2012.08.011
1581 Reddy, V., Nathues, A., Le Corre, L., Sierks, H., Li, J.-Y., Gaskell, R., McCoy, T. J., Beck, A. W., Schröder, S. E., Pieters, C. M.,
1582   Becker, K. J., Buratti, B. J., Denevi, B. W., Blewett, D. T., Christensen, U., Gaffey, M. J., Gutierrez-Marques, P., Hicks,
1583   M. D., Keller, H. U., Maue, T., Mottola, S., McFadden, L. A., McSween, H. Y., Mittlefehldt, D., O'Brien, D. P.,
1584   Raymond, C., & Russell, C. (2012b). Color and Albedo Heterogeneity of Vesta from Dawn. *Science, 336*(6082), 700-704.
1585   doi:10.1126/science.1219088
1586 Roatsch, T., Kersten, E., Matz, K.-D., Preusker, F., Scholten, F., Elgner, S., Jaumann, R., Raymond, C. A., & Russell, C. T. (2013).
1587   High-resolution Vesta Low Altitude Mapping Orbit Atlas derived from Dawn Framing Camera images. *Planetary and*
1588   *Space Science, 85*, 293-298.
1589 Roatsch, T., Kersten, E., Matz, K.-D., Preusker, F., Scholten, F., Jaumann, R., Raymond, C. A., & Russell, C. T. (2012). High
1590   resolution Vesta High Altitude Mapping Orbit (HAMO) Atlas derived from Dawn framing camera images. *Planetary and*
1591   *Space Science, 73*, 283-286.
1592 Ruesch, O., Hiesinger, H., Cloutis, E., Le Corre, L., Kallisch, J., Mann, P., Markus, K., Metzler, K., Nathues, A., & Reddy, V.
1593   (2015). Near infrared spectroscopy of HED meteorites: Effects of viewing geometry and compositional variations. *258*,
1594   384. doi:10.1016/j.icarus.2015.06.034
1595 Russell, C. T., McSween, H. Y., Jaumann, R., & Raymond, C. A. (2015). The Dawn Mission to Vesta and Ceres. In P. Michel
1596   (Ed.), *Asteroids IV* (pp. 419-432).
1597 Russell, C. T., Raymond, C. A., Coradini, A., McSween, H. Y., Zuber, M. T., Nathues, A., De Sanctis, M. C., Jaumann, R.,
1598   Konopliv, A. S., Preusker, F., Asmar, S. W., Park, R. S., Gaskell, R., Keller, H. U., Mottola, S., Roatsch, T., Scully, J. E.
1599   C., Smith, D. E., Tricarico, P., Toplis, M. J., Christensen, U. R., Feldman, W. C., Lawrence, D. J., McCoy, T. J.,
1600   Prettyman, T. H., Reedy, R. C., Sykes, M. E., & Titus, T. N. (2012). Dawn at Vesta: Testing the Protoplanetary
1601   Paradigm. *Science, 336*(6082), 684-686. doi:10.1126/science.1219381
1602 Ruzicka, A., Snyder, G. A., & Taylor, L. A. (1997). Vesta as the HED Parent Body: Implications for the Size of a Core and for
1603   Large-Scale Differentiation. *Meteoritics and Planetary Science, 32*.
1604 Salisbury, J. W., & Hunt, G. R. (1974). Meteorite spectra and weathering. *79*, 4439. doi:10.1029/JB079i029p04439
1605 Schenk, P., O'Brien, D. P., Marchi, S., Gaskell, R., Preusker, F., Roatsch, T., Jaumann, R., Buczkowski, D., McCord, T., McSween,
1606   H. Y., Williams, D., Yingst, A., Raymond, C., & Russell, C. (2012). The Geologically Recent Giant Impact Basins at
1607   Vesta's South Pole. *Science, 336*(6082), 694-697. doi:10.1126/science.1223272
1608 Schenk, P., Scully, J., Buczkowski, D., Sizemore, H., Schmidt, B., Pieters, C., Neesemann, A., O'Brien, D., Marchi, S., Williams,
1609   D., Nathues, A., De Sanctis, M., Tosi, F., Russell, C. T., Castillo-Rogez, J., & Raymond, C. (2020). Impact heat driven
1610   volatile redistribution at Occator crater on Ceres as a comparative planetary process. *11*, 3679. doi:10.1038/s41467-020-
1611   17184-7
1612 Schmedemann, N., Kneissl, T., Ivanov, B. A., Michael, G. G., Wagner, R. J., Neukum, G., Ruesch, O., Hiesinger, H., Krohn, K.,
1613   Roatsch, T., Preusker, F., Sierks, H., Jaumann, R., Reddy, V., Nathues, A., Walter, S. H. G., Neesemann, A., Raymond,
1614   C. A., & Russell, C. T. (2014). The cratering record, chronology and surface ages of (4) Vesta in comparison to smaller
1615   asteroids and the ages of HED meteorites. *Planetary and Space Science, 103*, 104-130. doi:10.1016/j.pss.2014.04.004
1616 Schröder, S. E., Mottola, S., Matz, K.-D., & Roatsch, T. (2014). In-flight calibration of the Dawn Framing Camera II: Flat fields
1617   and stray light correction. *Icarus, 234*, 99-108. doi:10.1016/j.icarus.2014.02.018

Scott, E. R. D., Greenwood, R. C., Franchi, I. A., & Sanders, I. S. (2009). Oxygen isotopic constraints on the origin and parent bodies of eucrites, diogenites, and howardites. *Geochimica et Cosmochimica Acta, 73*, 5835.

Scully, J. E. C., Russell, C. T., Yin, A., Jaumann, R., Carey, E., Castillo-Rogez, J., McSween, H. Y., Raymond, C. A., Reddy, V., & Le Corre, L. (2015). Geomorphological evidence for transient water flow on Vesta. *Earth and Planetary Science Letters, 411*, 151-163. doi:10.1016/j.epsl.2014.12.004

Sierks, H., Keller, H. U., Jaumann, R., Michalik, H., Behnke, T., Bubenhagen, F., Büttner, I., Carsenty, U., Christensen, U., Enge, R., Fiethe, B., Gutiérrez Marqués, P., Hartwig, H., Krüger, H., Kühne, W., Maue, T., Mottola, S., Nathues, A., Reiche, K.-U., Richards, M. L., Roatsch, T., Schröder, S. E., Szemerey, I., & Tschentscher, M. (2011). The Dawn Framing Camera. *Space Science Reviews, 163*, 263-327. doi:10.1007/s11214-011-9745-4

Sizemore, H. G., Platz, T., Schorghofer, N., Prettyman, T. H., De Sanctis, M. C., Crown, D. A., Schmedemann, N., Neesemann, A., Kneissl, T., Marchi, S., Schenk, P. M., Bland, M. T., Schmidt, B. E., Hughson, K. H. G., Tosi, F., Zambon, F., Mest, S. C., Yingst, R. A., Williams, D. A., Russell, C. T., & Raymond, C. A. (2017). Pitted terrains on (1) Ceres and implications for shallow subsurface volatile distribution. *Geophysical Research Letters, 44*, 6570-6578.

Stephan, K., Jaumann, R., De Sanctis, M. C., Ammannito, E., Krohn, K., Otto, K. A., Tosi, F., Combe, J.-P., Roatsch, T., Matz, K.-D., McFadden, L. A., Preusker, F., Raymond, C. A., & Russell, C. T. (2015). The Sextilia-region on Asteroid 4Vesta - Stratigraphy and variegation. *Icarus, 259*, 162-180. doi:10.1016/j.icarus.2015.05.016

Stephan, K., Jaumann, R., De Sanctis, M. C., Tosi, F., Ammannito, E., Krohn, K., Zambon, F., Marchi, S., Ruesch, O., Matz, K.-D., Preusker, F., Roatsch, T., Raymond, C. A., & Russell, C. T. (2014). Small fresh impact craters on asteroid 4 Vesta: A compositional and geological fingerprint. *Journal of Geophysical Research (Planets), 119*, 771-797.

Stubbs, T. J., & Wang, Y. (2012). Illumination conditions at the Asteroid 4 Vesta: Implications for the presence of water ice. *Icarus, 217*, 272.

Thangjam, G., Nathues, A., Mengel, K., Hoffmann, M., Schäfer, M., Reddy, V., Cloutis, E. A., Christensen, U., Sierks, H., Corre, L. L., Vincent, J.-B., & Russell, C. T. (2014). Olivine-rich exposures at Bellicia and Arruntia craters on (4) Vesta from Dawn FC. *Meteoritics and Planetary Science, 49*, 1831-1850.

Thangjam, G., Reddy, V., Le Corre, L., Nathues, A., Sierks, H., Hiesinger, H., Li, J.-Y., Sanchez, J. A., Russell, C. T., Gaskell, R., & Raymond, C. (2013). Lithologic mapping of HED terrains on Vesta using Dawn Framing Camera color data. *Meteoritics and Planetary Science, 48*(11), 2199-2210. doi:10.1111/maps.12132

Tompkins, S., & Pieters, C. M. (2010). Spectral characteristics of lunar impact melts and inferred mineralogy. *Meteoritics and Planetary Science, 45*, 1152-1169. doi:10.1111/j.1945-5100.2010.01074.x

Tornabene, L. L., McEwen, A. S., Osinski, G. R., Mouginis-Mark, P. J., Boyce, J. M., Williams, R. M. E., Wray, J. J., Grant, J. A., & Mars, H. T. J. S. I. C. o. (2007, July 01, 2007). *Impact Melting and the Role of Sub-Surface Volatiles: Implications for the Formation of Valley Networks and Phyllosilicate-rich Lithologies on Early Mars.*

Tornabene, L. L., Osinski, G. R., McEwen, A. S., Boyce, J. M., Bray, V. J., Caudill, C. M., Grant, J. A., Hamilton, C. W., Mattson, S., & Mouginis-Mark, P. J. (2012). Widespread crater-related pitted materials on Mars: Further evidence for the role of target volatiles during the impact process. *Icarus, 220*, 348.

Tosi, F., Capria, M. T., De Sanctis, M. C., Combe, J.-P., Zambon, F., Nathues, A., Schröder, S. E., Li, J.-Y., Palomba, E., Longobardo, A., Blewett, D. T., Denevi, B. W., Palmer, E., Capaccioni, F., Ammannito, E., Titus, T. M., Mittlefehldt, D. W., Sunshine, J. M., Russell, C. T., & Raymond, C. A. (2014). Thermal measurements of dark and bright surface features on Vesta as derived from Dawn/VIR. *Icarus, 240*, 36-57.

Williams, D. A., Denevi, B. W., Mittlefehldt, D. W., Mest, S. C., Schenk, P. M., Yingst, R. A., Buczkowski, D. L., Sculy, J. E. C., Garry, W. B., McCord, T. B., Combe, J.-P., Jaumann, R., Pieters, C. M., Nathues, A., Le Corre, L., Hoffmann, M., Reddy, V., Schäfer, M., Roatsch, T., Preusker, F., Marchi, S., Kneissl, T., Schmedemann, N., Neukum, G., Hiesinger, H., De Sanctis, M. C., Ammannito, E., Frigeri, A., Prettyman, T. H., Russell, C. T., & Raymond, C. A. (2014a). The geology of the Marcia quadrangle of asteroid Vesta: Assessing the effects of large, young craters. *Icarus, 244*, 74-88. doi:10.1016/j.icarus.2014.01.033

Williams, D. A., Jaumann, R., McSween, H. Y., Marchi, S., Schmedemann, N., Raymond, C. A., & Russell, C. T. (2014b). The chronostratigraphy of protoplanet Vesta. *Icarus, 244*, 158-165. doi:10.1016/j.icarus.2014.06.027

Williams, D. A., O'Brien, D. P., Schenk, P. M., Denevi, B. W., Carsenty, U., Marchi, S., Scully, J. E. C., Jaumann, R., De Sanctis, M. C., Palomba, E., Ammannito, E., Longobardo, A., Magni, G., Frigeri, A., Russell, C. T., Raymond, C. A., & Davison, T. M. (2014c). Lobate and flow-like features on asteroid Vesta. *103*, 24. doi:10.1016/j.pss.2013.06.017

Williams, J.-P., Bogert, C. H., Pathare, A. V., Michael, G. G., Kirchoff, M. R., & Hiesinger, H. (2018). Dating very young planetary surfaces from crater statistics: A review of issues and challenges. *Meteoritics and Planetary Science, 53*, 554-582. doi:10.1111/maps.12924

Zambon, F., De Sanctis, M. C., Schröder, S., Tosi, F., Longobardo, A., Ammannito, E., Blewett, D. T., Mittlefehldt, D. W., Li, J.-Y., Palomba, E., Capaccioni, F., Frigeri, A., Capria, M. T., Fonte, S., Nathues, A., Pieters, C. M., Russell, C. T., & Raymond, C. A. (2014). Spectral analysis of the bright materials on the asteroid Vesta. *Icarus, 240*, 73-85.

Zolensky, M. E., Weisberg, M. K., Buchanan, P. C., & Mittlefehldt, D. W. (1996). Mineralogy of carbonaceous chondrite clasts in HED achondrites and the Moon. *Meteoritics and Planetary Science, 31*, 518-537.